Advances in understanding mineral dust and boundary layer processes over the Sahara from Fennec aircraft observations

C.L. Ryder*[1], J.B. M[c]Quaid[2,6], C. Flamant[3], P. Rosenberg[2], R. Washington[4], H.E. Brindley[5], E.J. Highwood[1], J.H. Marsham[2, 6], D.J. Parker[2], M.C. Todd[7], J.R. Banks[5], J.K. Brooke[2,8], S. Engelstaedter[4], V. Estelles[9,a], P. Formenti[10], L. Garcia-Carreras[2], C. Kocha[3], F. Marenco[8], H. Sodemann[11, b] , C.J.T. Allen[4], A. Bourdon[12], M. Bart[2,c], C. Cavazos-Guerra[7,d], S.Chevaillier[10], J. Crosier[13], E. Darbyshire[1,13], A.R. Dean[14], J.R. Dorsey[13], J. Kent[8], D. O'Sullivan[8], K. Schepanski[2,e], K. Szpek[8], J. Trembath[14], A. Woolley[14].

[1] Department of Meteorology, University of Reading, RG6 6BB, UK

[2] School of Earth and Environment, University of Leeds, LS2 9JT, UK

[3] Sorbonne Universités, UPMC, Université Paris 06, CNRS & UVSQ, UMR 8190 LATMOS, Paris, France

[4] School of Geography and the Environment, University of Oxford, UK

[5] Space and Atmospheric Physics, Department of Physics, Imperial College London, UK

[6] National Centre for Atmospheric Science, University of Leeds, LS2 9JT, UK

[7] Department of Geography, University of Sussex, Brighton BN1 9QJ, UK

[8] Met Office, Exeter, EX1 3PB, UK

[9] Dept. Física Fundamental y Experimental, Electrónica y Sistemas, Universidad de La Laguna, Spain

[10] LISA, UMR CNRS 7583, Université Paris Est Créteil et Université Paris Diderot, Institut Pierre Simon Laplace, Créteil, France

[11] Institute for Atmospheric and Climate Science, ETH Zürich, Switzerland

[12] SAFIRE, UMS CNRS-CNES-Météo-France, Francazal, France

[13] National Centre for Atmospheric Science, University of Manchester, Manchester, M13 9PL, UK

[14] Facility for Airborne Atmospheric Measurements, Cranfield, MK43 0AL, UK

[a] Now at Department of Earth Physics and Thermodynamics, Universitat de València, Spain

[b] Now at Geophysical Institute, University of Bergen, Norway

[c] Now at Aeroqual Ltd, 109 Valley Road, Auckland, New Zealand

[d] Now at Institute for Advanced Sustainability Studies (IASS), Berliner Straße 130, 14467 Potsdam, Germany

[e] Now at Leibniz Institute for Tropospheric - Research - Permoserstr. 15 - 04318 Leipzig, Germany

[*] Correspond to c.l.ryder@reading.ac.uk

Abstract

The Fennec climate program aims to improve understanding of the Saharan climate system through a synergy of observations and modelling. We present a description of the Fennec airborne observations during 2011 and 2012 over the remote Sahara (Mauritania and Mali) and the advances in the understanding of mineral dust and boundary layer processes they have provided. Aircraft instrumentation aboard the UK FAAM BAe146 and French SAFIRE Falcon 20 is described, with specific focus on instrumentation specially developed and relevant to Saharan meteorology and dust. Flight locations, aims and associated meteorology are described. Examples and applications of aircraft measurements from the Fennec flights are presented, highlighting new scientific results delivered using a synergy of different instruments and aircraft. These include: (1) the first airborne measurement of dust particles sized up to 300 microns and associated dust fluxes in the Saharan atmospheric boundary layer (SABL), (2) dust uplift from the breakdown of the nocturnal low-level jet before becoming visible in SEVIRI satellite imagery, (3) vertical profiles of the unique vertical structure of turbulent fluxes in the SABL, (4) in-situ observations of processes in SABL clouds showing dust acting as CCN and IN at -15°C, (5) dual-aircraft observations of the SABL dynamics, thermodynamics and composition in the Saharan heat low region (SHL), (6) airborne observations of a dust storm associated with a cold-pool (haboob) issued from deep convection over the Atlas, (7) the first airborne chemical composition measurements of dust in the SHL region with differing composition, sources (determined using Lagrangian backward trajectory calculations) and absorption properties between 2011 and 2012, (8) coincident ozone and dust surface area measurements suggest coarser particles provide a route for ozone depletion, (9) discrepancies between airborne coarse mode size distributions and AERONET sunphotometer retrievals under light dust loadings. These results provide insights into boundary layer and dust processes in the SHL region – a region of substantial global climatic importance.

1 Background and Motivation

The Sahara desert remains one of the most data sparse regions on the planet. During the northern summer a vast low pressure system, the Saharan Heat Low (SHL), exists over the central Sahara caused by the strong solar heating and this drives major dynamical features (e.g. Lavaysse et al. (2009); Chauvin et al. (2010)). Strong sensible surface fluxes generate near-surface temperatures in excess of 40 °C and a deep Saharan Atmospheric Boundary Layer (SABL) that reaches to a height of 6000 m, generating what is commonly regarded to be the world's deepest boundary layer (Tompkins et al., 2005; Cuesta et al., 2009) . To the south of the Sahara lies the Sahel and the SHL exerts a significant influence upon this region, in particular the timing of the West African Monsoon (WAM) onset (Lavaysse et al., 2009; Sultan and Janicot, 2003). The prediction of the onset of the WAM has been the topic of a number of recent science programmes, (e.g. the African Monsoon Multidisciplinary Analysis (AMMA), Redelsperger et al. (2006)), as it is critical to the livelihoods of the population in this region: the growing season here is short and the ground must be prepared and planted ahead of the rains arriving.

The Sahara is the largest source of mineral dust on the planet, with the highest summer dust loadings co-located with the SHL (Engelstaedter et al., 2006). Mineral dust is an important atmospheric aerosol because of its direct and indirect radiative effects (Forster et al., 2007), its contribution to atmospheric chemistry (de Reus et al., 2005), and its transport and deposition of essential nutrients to the ocean

(Jickells et al., 2005). Saharan dust is known to modify hurricane activity by reducing local sea surface temperatures in the Caribbean (Dunion and Velden (2004); Sun et al. (2009); Jenkins et al. (2008)) and in the tropical Atlantic Ocean (Evan et al., 2011; Evan et al., 2009). Saharan dynamics, including haboobs frequently driven by moist convection (Marsham et al., 2013c), low level jets (Washington et al., 2006) and dust devils and convective plumes (Ansmann et al., 2009) result in vast quantities of dust being lofted on a very regular basis into the atmosphere where they are then susceptible to synoptic-scale atmospheric transport. Thus the Saharan region plays a significant role in the weather and climate in the northern hemisphere (Tompkins et al., 2005; Rodwell and Jung, 2008), influencing regions far beyond its geographical boundaries.

There are considerable uncertainties in both climate and numerical weather prediction models for this region (Evan et al., 2014; Marsham et al., 2008b; Messager et al., 2010). Representation of the position and intensity of the SHL in climate models varies considerably. Identifying the cause of such discrepancies and ascertaining which representation most closely matches reality can only be addressed through observational data. The extreme nature of the Saharan climate and also the considerable uncertainties associated with mineral dust aerosols in numerical models all compound the discrepancies between models and reality (e.g. Kim et al. (2014); Huneeus et al. (2011); Evan et al. (2014)). Additionally observations of both dust chemical composition and the full size distribution in this remote region are crucial for accurately representing the radiative effect of dust (Formenti et al. (2014); Mahowald et al. (2014)).

In the last decade or so, a number of field programmes have been tasked with improving the observational dataset on meteorological and aerosol conditions in the wider North African sector (Table 1 and Figure 1). With the exception of limited measurements during AMMA (Messager et al., 2010; Cuesta et al., 2008), no previous campaign has focused on this central region of North Africa during the summer dust season. For example, SAMUM1 was based in Morocco, while SAMUM2 observations took place at the Cape Verde Islands (Heintzenberg, 2009; Ansmann et al., 2011). Fennec was conceived and designed to fill critical gaps in observations and understanding of the Saharan climate system.

The Fennec climate programme aims to improve understanding of and quantify the physical processes controlling the Saharan climate system, through a synergy of observational and modelling approaches in order to evaluate and attribute errors in weather and climate models for this region (Washington et al., 2012). The observational strategy is a large scale, multi-platform approach involving ground-based measurements, airborne observations and Earth observation. Fennec is an international consortium which includes research groups from the United Kingdom, France, Germany, Switzerland and the United States of America working in collaboration with the Meteorological Services of Algeria and Mauritania in North Africa.

This paper will focus on the airborne operations that were deployed as part of the Fennec programme and key scientific findings stemming from the airborne programme. Observations by means of an airborne platform provide an invaluable approach, including access to remote, inhospitable regions of the Sahara, tracking of non-static atmospheric features and providing vertical profile observations as well as dust observations above the surface layer, which is vital to understanding the capacity for long-range transport of uplifted dust. Airborne platforms can be positioned at appropriate altitudes for dedicated remote sensing surveys such as above/below radiatively active layers of mineral dust.

Measurements on aircraft platforms provide the ability to link together spatial and temporal features which are simply not accessible through fixed ground sites or satellites or even a combination of both. Furthermore, specifically in the June 2011 Intensive Observation Period (IOP) two aircraft were operated and their combined power meant that specific events could be followed through staggered missions. Finally, the combination of ground, airborne and satellite observations provide the fullest picture possible of the area of interest.

During 2011 and 2012 an extensive dataset was collected as part of the Fennec intensive observation programme. These included the deployment of two airborne platforms: the UK BAe146 FAAM and French SAFIRE F-20 aircraft, and also ground based observations via two supersites located on the western and eastern flanks of the central Sahara: Zouerate, Mauritania (Todd et al., 2013) and Bordj Badji Mokhtar, Algeria (Allen et al., 2013; Marsham et al., 2013b). These were supplemented by a network of automated weather stations which were installed in the remote desert (Hobby et al., 2013). An overview of the aircraft deployments are provided in Table 2; more detailed flight information is presented later. As part of the outreach activities of the Fennec project a movie, 'Into the Cauldron: A Meteorological Adventure,' has been also produced (Sternberg, 2013).

In addition to the Fennec programme, a number of supplementary projects took advantage of the aircraft deployment to the region. The Lagrangian Dust Source Inversion Experiment (LADUNEX) (Sodemann et al., 2015, accepted for publication) used the in-situ and remote sensing observations of mineral dust in order to validate a Lagrangian particle dispersion model FLEXPART and improve its ability to represent dust transport in the atmosphere. RAIN4DUST project exploited the remote sensing data from the French Falcon aircraft to investigate dust sources in relation to sediment supply and surface characteristics in the foothills of the central Saharan mountain ranges (Schepanski et al., 2013). Finally, the Sunphotometer Airborne Validation EXperiment (SAVEX) was designed to take advantage of the use of the island of Fuerteventura as operating base from which to conduct an intercomparison of a number of sunphotometers installed on Tenerife with aircraft observations.

The aims of this paper are firstly to document and describe the flights and meteorology during the 3 Fennec IOPs in order to provide a reference and context for published and future articles. Secondly, we provide new scientific results that have come about as a result of the Fennec airborne programme, both through airborne observations in isolation over the remote Sahara, and through the integration of data from different platforms – i.e. dual-aircraft observations and ground-based, airborne and satellite platforms. Therefore this paper provides insights into Saharan processes which separate papers cannot. Finally, despite many challenges, the Fennec aircraft campaigns have collected the only comprehensive in-situ data from the Saharan region – a region of substantial global climatic importance. Along with ground-based and satellite measurements, these data provide a much-needed resource with which to develop the science linking dust, dynamics and radiation in the central Sahara, and will be heavily exploited in the coming years. This paper provides a detailed overview of the data and its context, as well as a survey of first results.

The paper is structured as follows: in Section 2 we describe the aircraft instrumentation, with a focus on instrumentation specifically developed or installed for Fennec, and also provide information on data provision for the scientific community. Section 3 describes the meteorology during Fennec and provides an overview of the flights performed. Section 4 provides a description of new scientific results, Section 5 concludes the article.

2 Aircraft Instrumentation

Here we describe the instrumentation on both aircraft, the BAe146 and the Falcon F-20, with particular emphasis regarding instrumentation particularly relevant to Fennec measurements. Throughout this article we refer to particle size in diameter.

2.1 FAAM BAe146 Aircraft

The UK's BAe-146-301 Large Atmospheric Research Aircraft operated by the Facility for Airborne Atmospheric Measurements (FAAM) (henceforth the BAe146 aircraft) is available to the science community in a number of different configurations. These allow the most efficient use of space and access to inlets (which tend to be in the forward section of the cabin) as well as minimizing the aircraft payload, which in turn maximizes the sortie duration. Due to the remoteness of the areas of interest for Fennec the instrument fit was customized to provide the best balance of observational rigour and range. Table 4 details the instrument fit for the Fennec IOPs; some instruments were only available for some of the deployments, these are indicated in the table. There are a number of excellent descriptions of the standard instrumentation from previous campaigns which have utilised the BAe146 aircraft (e.g. (Renfrew et al. (2008); Highwood et al., 2012; McConnell et al., 2008; Haywood et al., 2011a)); other specific instrumental references are provided in Table 4. Instrumentation specifically developed, installed or configured for Fennec are described in more detail below.

2.1.1 LIDAR

The BAe146 aircraft operates a commercial Leosphere ALS450 backscatter LIDAR suitable for aerosol and thin cloud observation (Marenco et al., 2011). A description of the LIDAR system is provided by Chazette et al. (2012) and technical information is available in Table 1 of Marenco et al. (2014). The nadir-viewing LIDAR provides elastic backscatter at 355 nm and features an uncalibrated depolarisation channel, used qualitatively to distinguish depolarising layers. Data are recorded at a vertical resolution of 1.5 m and an integration time of 2 s, giving approximately 200 m horizontal resolution at aircraft speeds. The instrument is lightweight, has a relatively small receiver aperture of 15 cm diameter, has a 12 mJ pulse energy (20 Hz PRF) output and requires a low level of maintenance which makes it ideal for frequent operation aboard the BAe146 aircraft. However, as a consequence the signal to noise ratio is poorer compared to the Falcon LNG LIDAR.

Initial quick-look data is provided as range-square corrected signal (arbitrary units) which is proportional to the total backscatter coefficient from molecules and particles at a given range, r, times the two-way transmission of light from the laser source to the range r (i.e. a function of the atmospheric optical depth), for example as shown in Figure 7 and Figure 17, for which no attempt has been made to correct for attenuation by the aerosol layers. In these cases we use the Leosphere LIDAR data to locate dust layers and clouds, for which the range-corrected backscattered signal is sufficient, although dust layers lower in the atmosphere may not always be evident with such a representation, due to attenuation at higher altitudes.

In a further step, aerosol extinction coefficient can be computed from the LIDAR range-square corrected backscatter signal using the method described by Marenco et al. (2013), although this is labour-intensive, since the method is not automated and it requires a profile-by-profile review of assumptions. Additionally, the signal-to-noise ratio for the dust laden atmosphere in the Fennec region often causes difficulties in inverting the LIDAR backscatter signal to extinction coefficients. This can be overcome by integrating the lidar signals, i.e. Sodemann et al. (2015, accepted for publication)

198 decrease resolution to 300 m in the vertical, and a 60 s integration time, translating to extinction
199 coefficient profiles provided at a ~9 km along-track footprint at a typical ground speed of ~150 ms^{-1}.
200 In the lowest 0-2 km layer the uncertainty in the extinction coefficient is of the order of 100%, but this
201 uncertainty quickly decreases above, the extent of which is dependent on the ambient aerosol
202 conditions (e.g. Marenco et al. (2014)).

203 **2.1.2 Low Turbulence Inlet (LTI)**

204 A very important consideration when observing aerosol particles is the efficiency of the transmission
205 system which passes external aerosol into the aircraft cabin for collection or in situ analysis. It is
206 highlighted in the difficulty in making accurate and reliable measurements from an aircraft platform,
207 particularly that of coarse mode aerosol (Wendisch et al., 2004). For objectives such as those of the
208 Fennec program, this is of particular importance since a significant fraction of mineral dust is in the
209 coarse mode (Weinzierl et al., 2009). Inlet design can modify aerosol size distribution through either
210 underestimation due to aerosol losses or overestimation due to enhancements.

211 The BAe146 has a specialised Low Turbulence Inlet (LTI) which is designed to provide a characterised
212 community inlet capable of delivering supermicron aerosol into the cabin. This is achieved by reducing
213 turbulent flow within the tip of the inlet, reducing impaction of particles to the walls of the inlet
214 (Wilson et al., 2004). The LTI further maintains isokinetic sampling flow using a feedback controlled
215 pumping system.

216 A Grimm Technik Optical Particle Counter (OPC) was mounted inside the aircraft cabin behind the LTI
217 (LTI-GRIMM), and showed that size distributions behind the LTI compare well with those from the
218 externally mounted aircraft probes. In order to further evaluate inlet efficiency on the BAe146, Grimm
219 OPCs were mounted behind various Rosemount inlets. This allowed evaluation of the size distributions
220 passed by the standard BAe146 Rosemount inlets for the first time, from which many of the internally
221 installed aerosol instruments draw their sample from, such as the nephelometer, particle soot
222 absorption photometer, and aerosol mass spectrometer (Trembath, 2012; Trembath et al., 2012).
223 Significant losses and enhancements of the size distribution have been found to occur at different size
224 ranges.

225 **2.1.3 Double Nephelometer Setup**

226 During Fennec, two TSI 3563 integrating nephelometers measuring scattering at 450, 550 and 700 nm
227 were operated inside the aircraft cabin behind a Rosemount Inlet. During Fennec 2011, the
228 nephelometers were run in series with a BGI Very Sharp Cut Cyclone Impactor between them. The
229 impactor has a 50% penetration efficiency at 2.5 µm aerodynamic diameter, or around 1.5 µm
230 geometric diameter, at a flow rate of 16.67 litres per minute (LPM). This therefore allows the 'first'
231 nephelometer to measure scattering due to all particles passing the Rosemount inlet and the pipework
232 (estimated to be particles smaller than 2.5 microns, Trembath (2012)), and the 'second' nephelometer
233 to measure scattering from the fraction of particles smaller than 1.5 microns. However, due to the
234 nephelometers being in series, it was difficult to account for the loss of particles between the two
235 instruments. Therefore during Fennec 2012 the two nephelometers were operated in parallel to avoid
236 this problem. This was possible due to a more powerful pump being used, capable of 50 LPM, even up
237 to altitudes of up to 9000 m. Secondly a volume flow controller was installed to replace the mass flow
238 meter and needle valve.

The synergy in the approach of operating a Grimm OPC behind a Rosemount inlet to measure the size distribution, and the use of the impactor to separate the sub-1.5 micron scattering from that measured as standard by the nephelometer is novel, and allows any bias in scattering and absorption due to Rosemount inlet and pipework effects on the BAe146 to be assessed for the first time, which can lead to significant underestimation of dust absorption properties when not accounted for (Ryder et al., 2013b).

2.1.4 Size Distribution Measurements

The BAe146 is well equipped to measure aerosol size distributions (for example, see Haywood et al. (2008); Johnson et al. (2012)). However, the Fennec campaign was unusual amongst aerosol campaigns in the large number of instruments operated to measure particles larger than 3 µm diameter, and in the measurement of 'giant mode' particles – those sized over 30-40 µm. Interestingly, the recent eruption of Eyjafjallajökull in Iceland has reinvigorated the interest in 1-10 um particles since volcanic ash is generally in the same size region as mineral dust and they both have similar challenges such as non-spherical morphology (Ansmann et al, 2012): hence there is considerable benefit to be gained from the concerted efforts surrounding the observation of volcanic ash.

Instruments measuring size distribution, and the size ranges measured are shown in Table 4, and also in detail by Ryder et al. (2013b). During Fennec 2011, a total of 6 different instruments successfully measured size distributions between sizes of 0.15 to 300 microns diameter - namely the PCASP (accumulation mode), CDP, LTI-GRIMM, SID2H and CAS (coarse mode), and finally the University of Manchester CIP15 in the giant mode (see Table 4 for explanation of acronyms). All of these are wing mounted except the LTI-GRIMM, and all are optical particle counters, making use of light scattering techniques, except the CIP which uses imaging shadowing techniques (Knollenberg, 1970). Although the CIP15 is capable of measuring particles sized up to 930 µm, electrical noise allowed measurements up to 300 µm. During Fennec 2012 a slightly different suite of instruments was operated due to logistical requirements, comprising a PCASP, CDP, 2DC, SID2H, FAAM CIP15 and FAAM CIP100. Unfortunately the CIP15 suffered from electrical noise during the 2012 IOP and the data was not usable. However, the operation of other instruments such as the CDP and 2DC provide alternative measurements for this size range. Additionally the operation of the CIP100 probe extends the measurement range up to 6200 µm.

When interpreting OPC size distribution data, it is important that various limitations are noted and uncertainties taken account of (e.g. Reid et al. (2003)). In order to deal with several sources of uncertainty regarding OPC measurements, the instruments were calibrated and size distributions carefully processed as described in detail by Rosenberg et al. (2012). The PCASP was calibrated with PSL nanospheres with diameters from 0.4 to 3 µm and oil particles size selected by a DMA with diameters from 0.145 to 0.360 µm. The CDP was calibrated with glass beads, ranging from 15.9 to 49.9 µm. Smaller beads were not used due to a tendency for them to clump together, therefore the calibration was extrapolated below this size (including over the size range influenced by the inflection in the Mie response curve). Uncertainties due to this extrapolation were included in the total uncertainty budget. Our approach is to use a rigorous methodology to assign uncertainties to the data which take account of inherent problems associated with processing OPC data. Each OPC is considered as an instrument which directly measures particle scattering cross section and is calibrated in terms of this variable. Using the uncertainty in this calibration and Mie theory with an appropriate refractive index for the measured aerosol, we derive a probability density function which gives the probability

of a particle of a particular size being counted in a particular OPC bin. Integrating this probability density function allows us to derive the mean diameter and effective width of each bin. This method also permits full uncertainty propagation including ambiguities caused by the nonlinear and non-monatonic Mie theory relating scattering cross-section to particle diameter. For example, there is an inflection point in this relationship in the 5 to 10 µm range, which results in larger bin size errors across this size range (e.g. see horizontal error bars in Figure 4). Thus we represent the degeneracy in the response curve using uncertainties in the bin widths and bin centre points without any need for arbitrary smoothing or human thresholds. Note that this method results in bin widths significantly different to those provided by the manufacturer, which if used, would have introduced artefacts in the size distributions. Finally, we highlight the regular calibration of the CDP probe during the campaign, which results in better characterised size distributions (see Rosenberg et al., 2012).

Reid et al. (2003) outline various other deficiencies in previously presented OPC results. For example, they suggest that their OPCs were not able to represent size distribution variability which they believed was occurring in reality. This was not the case during Fennec; for example the effective diameter ranged from under 2 µm to over 20 µm (Ryder et al., 2013b), and Figure 4 in this article clearly shows contrasting size distributions where the peaks were either narrow and centred upon 10 microns diameter or broad across 10 to 70 microns. During Fennec the OPCs were clearly responding to different ambient distributions. Reid et al. (2003) also suggest that unknown particle refractive index and shape factor has affected OPC results. Here we processed the OPC data using refractive indices spanning 1.53–0.001i to 1.53–0.003i and errors in diameter and number concentration due to this uncertainty have been propagated (sensitivity tests using different real parts of the refractive index showed little impact on the final size distribution). The size distributions have been produced assuming spherical particles rather than non-spherical particles, which has been shown to have a negligible impact on the resulting size distributions (Osborne et al., 2011; Veihelmann et al., 2006; Lacis and Mishchenko, 1995; Liu et al., 1992). Additionally, instruments which utilized light scattering measurments at different scattering angle ranges (such as the CDP at 4 to 12°, compared to the GRIMM Technik OPCs at 30 to 150° plus 81 to 99°) produced similar size distributions (Ryder et al., 2013b) suggesting that sensitivity to viewing angle during Fennec was minimal.

Of particular note during Fennec was the operation of shadow imaging probes, such as the CIP15 during 2011 for measurement of particles sized 15 microns and above. This data is particularly valuable because unlike optical particle counter data it does not rely the non-monatonic Mie scattering relationships to derive particle size. Both Rosenberg et al. (2012) and Ryder et al. (2013b) show that the CIP15 and CDP/SID2H size distributions agree well in the overlap zone, suggesting accurate measurements of size distributions, despite the different measurement techniques applied. This further emphasizes that the reliability of the Fennec size distributions presented here.

Additionally, the PCASP and CDP agree well at their overlap zones. (see Ryder et al. (2013b) and Rosenberg et al. (2012) for full details). The combination of these rigorous calibration regimes, detailed processing procedures and agreement between instruments gives good confidence in the measured size distributions, particularly when significant numbers of coarse particles are present (e.g. see Section 4.1.1). When operated and processed with care and attention as described above, where the key uncertainties are quantified and in combination with other instrumentation, OPCs provide results which are reliable for representing volume distributions in the coarse mode.

2.1.5 Spectrally Resolved Radiation Measurements

In addition to the core pyranometers on the upper and lower of the aircraft fuselage measuring downwelling and upwelling shortwave irradiance respectively, a number of specialist radiometers were operated during Fennec which will allow considerably more detailed radiative measurements and radiative closure to be performed. In the shortwave spectrum, the Spectral Hemispheric Irradiance MeasurementS (SHIMS) measured spectrally resolved up and downwelling irradiance from 0.3 to 1.7 μm. The Shortwave Spectrometer (SWS) measures spectrally resolved radiances from 0.3 to 1.7 μm, using an externally mounted scanning telescope designed for viewing at particular angles. In the longwave spectrum, the Airborne Research Interferometer Evaluation System (ARIES) measured spectrally resolved radiances from 3.3 to 18 μm, at either nadir or zenith, as well as several different downward-pointing angles. Further details of SHIMS, SWS and ARIES can be found in Osborne et al. (2011). Operation of these instruments allows detailed radiative closure to be performed (e.g. (Haywood et al. (2011b); Osborne et al., 2011)). Further work will examine the radiative measurements made under extremely high dust loadings when very large particles were present.

2.1.6 Turbulence probe

Due to the scientific objectives of the Fennec program, the ability of the aircraft to make robust observations of atmospheric turbulence was of paramount importance. Three dimensional wind vectors are generated using a 5 port radome mounted turbulence probe at the aircraft nose which provides angle of attack measurements. These are combined with pitot tube measurements of air speed and position information from a GPS inertial navigation unit to generated ground referenced wind vectors at 32 Hz (Petersen & Renfrew 2009). A known linear dependence between the vertical component and aircraft pitch results in additional post-processing. This is likely the result of uncertainties in the calibration of the turbulence or pitot probes. Some of the parameters (static pressure and airspeed required for the processing) are generated through the on-board aircraft computer, this is calibrated in-situ annually as part of the maintenance schedule, using a pressure calibrator. Airspeed is calibrated similarly. The radome transducers are calibrated at a calibration laboratory annually, or as determined by inspection of the data for drifts or other artefacts. The INU alignment is assessed annually by a physical survey for pitch, roll, and heading. Angle of attack (AOA) and angle of sideslip (AOSS) calibrations derive from AOA/AOSS flight manoeuvres that were carried out when the facility was commissioned, as they are physically dependent on the radome mounting. These have been subsequently validated to confirm this. The AOA/AOSS is further corrected using yawing orbits, where further corrections are introduced to these quantities. True airspeed is corrected using reverse-heading manoeuvres, where the correction minimises the difference in derived wind measurement up/down wind.

2.1.7 Cloud Condensation Nuclei Observations

The concentration and properties of Cloud Condensation Nuclei (CCN) were measured using a commercial dual column continuous flow streamwise thermal gradient instrument (Droplet Measurement Technologies, Boulder, Co). The principles of its design are outlined in (Roberts and Nenes (2005); Lance et al. (2006); Rose et al. (2008)). Ambient air is drawn into a pair of temperature controlled columns where it encounters a particle free sheath flow which is humidified to near-saturation. A thermal gradient exists down each of the columns, meaning that supersaturation occurs as the samples flows through the columns. Activated aerosol will form droplets and increase in size

dependent upon their hygroscopicity. The instrument is configured to provide a pair of supersaturations at any time and has supersaturation range nominally between 0.07 % and 2 %. The residence time within the humidified zone is sufficient that these activated droplets grow to diameters larger than 1 µm, all particles with a diameter below this threshold are judged to be unactivated interstitial particles. An optical particle counter at the base of each column estimates the size distribution of the droplets (0.75 - 10 µm across 20 size bins).

In order to ensure stable volumetric flow to the CCN instrument, vital for robust measurements across altitude ranges encountered by airborne platforms, it draws air from a reduced pressure buffer volume which is connected to a modified Rosemount 102E inlet (Trembath, 2012). In addition to the CCN, a condensation particle counter, CPC (modified 3786 UCPC, Quant Technologies) also samples from this plenum to allow the total concentration of particles (2.5 nm – 3 µm) to be determined.

2.2 SAFIRE Falcon F-20 Aircraft

The SAFIRE (Service des Avions Français Instrumentés pour la Recherche en Environnement) Falcon 20 (F20) performed research flights during the June 2011 IOP. In contrast to the BAe146, it was equipped mostly with instrumentation designed to target the Saharan heat low region remotely from high altitudes (see Table 3 detailing the F20 instrumentation).

The F20 was equipped with the backscatter LIDAR LEANDRE Nouvelle Génération (LNG, de Villiers et al. (2010)), allowing the measurement of atmospheric reflectivity at three wavelengths (355, 532 and 1064 nm) to analyze the structure and radiative characteristics of desert dust plumes with a vertical resolution of 15 m and a horizontal resolution of 2 km (corresponding to a temporal averaging of the data of 10 s - or 200 shots - in order to reach a signal to noise ratio above 100). The LIDAR also has a depolarization capability on the 355 nm channel. During Fennec, the profiles of aerosol extinction coefficient at 532 nm are retrieved with an uncertainty on the order of 15% using a standard LIDAR inversion technique which is described at length in Banks et al. (2013) and Schepanski et al. (2013). The aerosol LIDAR ratio used for the inversion is considered to be constant with altitude and set to 47 sr. This value is intermediate between the value derived at 532 nm from space-borne, airborne, and ground-based LIDAR systems over northern Africa (i.e. 55 sr: Heintzenberg (2009) and Schuster et al. (2012), 50-60 sr: Tesche et al. (2009); Gross et al. (2011)) and those derived over Sahelian Africa (i.e. 41 sr: Omar et al. (2009) and Schuster et al. (2012)).

In addition to the LIDAR, the Falcon 20 was also equipped with a Vaisala AVAPS dropsondes launching system (a total of 136 sondes were launched from the Falcon aircraft during the 2011 deployment), radiometers (broadband up- and down-looking Kipp and Zonen pyranometers and pyrgeometers), the radiometer CLIMAT (Legrand et al. (2000)) as well as in situ pressure, temperature, humidity and wind sensors. There was also a nadir pointing visible camera (Basler SCA 1400-30FM with a 9 mm lens (Fujion, 2/3")) mounted aboard the Falcon providing high-resolution aerial photographs of the surface (Schepanski et al., 2013).

2.3 Access to Data

UK-Fennec FAAM aircraft data from the BAe146 is available at the British Atmospheric Data Centre (BADC, http://badc.nerc.ac.uk/home/index.html) and is freely available subject to registration. Fennec-France aircraft data is available from the Sedoo (Service de données de l'OMP,

http://catalogue.amma-international.org/) and is attached to the AMMA database, subject to free registration, listed under "Fennec" in the project list.

3 Flights and Meteorology

We now provide an overview of the meteorology and dust events during the campaigns, and a description of the flights performed in relation to these. A preliminary mission with the BAe146 was carried out in April 2011, using Ouarzazate, Morocco as the aircraft base, with measurements taken over Mauritania. However, flight restrictions from this base meant that it was logistically more straightforward to operate from Fuerteventura, one of the Canary Islands, Spain, from where subsequent campaigns in June 2011 (both aircraft) and June 2012 (BAe146 only) were based. From Fuerteventura, research flights operated over Mauritania, Mali, Senegal and the Eastern Atlantic Ocean. In following sections, flight numbers prefixed with 'b' refer to BAe146 flights, whereas flight numbers starting with 'F' refer to Falcon flights.

3.1 Meteorology

Here, we consider the synoptic scale structure of the atmosphere in the North African sector during the three Fennec observational phases shown in Table 2. We relate this in general terms to the structure of the SABL and dust conditions observed in the Fennec flight domain of the western Saharan region. In specific relation to the two summertime phases of June 2011 and 2012, we consider the state of the dominant features of the summertime low-level circulation over western North Africa, namely the Azores high pressure system, the SHL and the inter-tropical discontinuity (ITD), as well as the upper level circulation in the adjacent mid-latitudes. The SHL has a pronounced seasonal cycle (Lavaysse et al., 2009) involving a southeast to northwest migration from its position to the south of the Hoggar mountains (~18°N, 5°E) in May to its most northerly position close to 24°N and 0°W during July and August. The climatological mean date of transition between these two states is 20th June.

3.1.1 Fennec Pilot Campaign 2011

The synoptic situation during the short Fennec pilot campaign during April 5th-8th 2011 generated numerous dust emission events characteristic of spring time dust events over the Sahara. On the 1st and 2nd April a high pressure ridge over Algeria-Libya sector drove a strong northeasterly Harmattan surge over the central-eastern Sahara activating multiple dust sources in Algeria, Libya, Niger and Chad created a large dust plume of advected dust southwestward over Northern Mali, Southern Algeria by the 3rd. Further westward transport of this plume into the Fennec aircraft operations zone was prevented by strong northeasterly circulation around an intense cut-off low on the 3rd-4th April (Feature A in Figure 3a). This low tracked northwards from western Algeria to Morocco over this period and was accompanied by strong cyclonic near surface winds with pronounced dust emission along primary and secondary cold fronts penetrating southeastward over southern Morocco and northern Mauritania on the 4th April. Fennec flight b589 was able to observe this dust feature and the accompanying cold surge. Subsequent flights on the 5th-8th (see Table 5) observed the interaction of the cold maritime intrusion with dusty Saharan air, after which the dust was transported towards Portugal (Preissler et al., 2011).

3.1.2 Fennec IOP 2011

During this IOP most of the F20 and BAe146 flights were conducted over northern Mauritania and northern Mali. In terms of the large-scale structure of the atmosphere during June 2011 in this region,

a clear distinction can be made between a 'maritime phase' from around the 2nd-12th June and a 'heat-low phase' from around the 13th-30th June (see Todd et al., 2013 for full details). These phases essentially determine conditions across the entire central-western Sahara. These maritime and heat-low phases are broadly congruent with the 'east' and 'west' and phases, respectively, of the intraseasonal SHL mode of variability described by Chauvin et al. (2010). During the maritime ('heat low east') phase the upper level pattern exhibited a trough centered over the Iberian peninsula extending southwards over the northern extremity of North Africa (Feature A in Figure 3b). In addition, at low levels the SHL remained relatively stationary in an anomalously eastward location centred ~15°E (Feature B in Figure 3b), similar to the mean state for May, and the Azores high ridged towards the coast of northwest Africa. These conditions combined to drive anomalous westerlies throughout the troposphere over northwest Africa creating a strong northwesterly inflow of maritime air over much of the Fennec flight domain (Feature C in Figure 3b) with the ITD displaced southward (not shown). As such, the Sahara is effectively 'ventilated' by cool advection from the Atlantic sector restricting the heat low to the central/eastern Sahara. Accordingly, Fennec observations at both supersites (not shown) indicate that the SABL during the maritime phase to be anomalously cool and dry with shallow daytime convective boundary layer development (Marsham et al., 2013b; Todd et al., 2013) and generally cloud free conditions. Aerosol loading was low due to the relative absence over the Fennec flight domain of the two dominant dust generating processes, namely cold pools from moist convective systems, favoured within the southerly monsoon flow (ITD 'bulge') on the eastern flank of the SHL, and enhanced northeasterly Harmattan winds around the western flank of SHL trough. As a consequence, these two dust generating activity were largely restricted to the central Sahara with the eastward-displaced SHL.

Subsequently, during the latter Heat Low (west) phase anomalous positive geopotential heights dominated over Iberia and the extremity of northwest Africa (Feature A in Figure 3c), associated with the passage of three upper level ridges. At lower levels, the SHL exhibited an abrupt westward displacement to ~5-10°W (Feature B in Figure 3c) in two distinct intraseasonal pulses. These conditions combined to drive anomalous mid and upper level easterly flow, with easterlies at lower levels around the SHL, evident over the western Saharan sector (Feature C in Figure 3c) and Fennec flight domain. Fennec ground-based observations indicate the SABL during the Heat Low phase of June 2011 to be substantially hotter with deeper afternoon Convective Boundary Layer (CBL) development and cases of almost 'pure' well-mixed near dry-adiabatic profiles from the surface to the top of the Saharan Residual Layer (SRL) at ~5 km height. Dust aerosol loadings are substantially higher over the western Sahara and Fennec flight domain during the heat low phase associated with enhanced meso-scale convective activity and strong easterlies around the heat low and African Easterly wave troughs. Shallow convective cloud was common developing in the later afternoon in the relatively moist upper SRL.

Flight planning to meet Fennec science objectives was largely determined by synoptic meteorology, as well as logistical constraints. As such, the science objectives of specific flights (Table 5, Table 6 and Table 7) are geared to the prevailing meteorology described above. Overall, flights during the maritime phase (Falcon only) were able to sample substantial dust emission events over northern Mauritania (F13, F18). During the heat low phase certain flights were able to measure dust-meteorological processes associated with both northeasterly low level jet –related emission (e.g. b600/601/602, b610, b614) and mesoscale convective system (MCS) cold pool events originating over central Mali (b604) and also the Atlas mountains to the north (b605 and F22/F23). Flights to survey the SABL were

able to measure the pronounced evolution in the structure of the PBL over this transition from maritime (e.g. F14-F17) to heat low phases (e.g. b607/b608, F24/F25), representing the intra-seasonal variability and seasonal evolution of the Saharan atmosphere.

3.1.3 Fennec IOP 2012

Unlike the equivalent period of June 2011 Fennec IOP 2012 period 1-17th June there was no clear projection of the circulation onto the east-west heat low mode of Chauvin et al. (2010). As such, the period was characterised by a relatively stationary SHL centred close to the triple point of the Algeria-Niger-Mali border, further west than during the first half of June 2011. However, relatively subtle synoptic-scale variations strongly influenced the circulation over the western Saharan sector and the Fennec flight domain. First, during the early part of June 2012 from 1st-9th a weak upper level trough extended south towards the coast of Morocco (Feature A, Figure 3d) and a heat low extension was established over far western Algeria (Feature B, Figure 3d) driving a strong northwesterly maritime flow over the Fennec domain (Feature C, Figure 3d). As with the maritime phase of IOP 2011 this led to the characteristic maritime conditions of a cool, dry SABL with shallow CBL daytime development and relatively cloud- and aerosol-free conditions over almost all the domain. This maritime flow weakened after the 10th June and a heat low extension west into northwest Mali from 14th-17th June (not shown) established more characteristic heat low SABL conditions over the eastern Fennec flight domain. Specifically, a strong northeasterly low level flow around the western flank of the HL trough favourable to dust emission and a northern extension of monsoon flow to the east over Mali developed. MCS activity increased as the maritime flow weakened after the 8th June and substantial cold pool events were observed in the monsoon flow over Southern Mauritania on the 8th (see ITD 'bulge' Feature D in Figure 3d) and over Southern Mali on the 12th and 14th (not shown).

Fennec 2012 flights targeted specific features of the evolving Saharan atmosphere, including surveys of the maritime flow in the early period (b699/700), aged dust from MCS cold pools to the south of the flight domain sampled over the ocean (b702-3) and southern Mauritania (b704), boundary layer heat fluxes close to edge of the SHL (b705), the SHL tongue and LLJ dust emission (b706-8) and dust uplift and radiative processes (b708-9).

3.2 Description of Flights

Table 5 to Table 7 list each flight conducted during the various Fennec phases. A brief description of each flight is provided here to link the meteorology described in Section 3.1 to each flight's scientific aims, and to provide information for future reference. Some flights and key scientific results are described further in Section 4.

3.2.1 Flights during the Pilot Campaign 2011

During the Fennec Pilot campaign in April 2011, 7 flights were performed (Table 5, Figure 2a). b589 was an initial shake-down flight to test operational logistics, and was conducted at high altitude only, but overflew a dust front which was observed with the LIDAR and dropsondes. b590 (morning) and b591 (afternoon) were the first flights performing in-situ measurements, and sampled maritime inflow over Mauritania, which was overlain by dust layers at higher altitudes. b592 took place 2 days later on 7 April (note b592 was actually two separate flights, one in the morning and one in the afternoon) and sampled the diurnal evolution of the recovering SABL (Saharan boundary layer) following the retreat of marine air. b593 continued the sampling of the recovering SABL, but over a different surface albedo.

b594 was a science transit return of the BAe146 to the UK, sampling dust transported northwards by a low pressure system over Morocco.

3.2.2 Flights during Fennec IOP 2011

June 2011 was the main flying period of Fennec, when both the Falcon and the BAe146 were conducting missions over the Sahara. Eleven flights were performed with the F20 during the period 2-16 June (Figure 2b, Table 6). The first four flights (F09 – F12) were designed to sample the dust outflow from the continent, over the coastal Atlantic, though almost no dust was sampled during F10. The subsequent seven flights were conducted over the continent, with two flights (F13 and F18) dedicated to the study of the morning dust uplift over alluvial sources of Northern Mauritania in connection with the decay of the low-level jet. The flights were part of the RAIN4DUST project funded by the EUropean Facility for Airborne Research, EUFAR (Schepanski et al., 2013), designed to examine alluvial deposits as a dust source. Four flights were conducted along the exact same track (F14, F16, F17 and F19) to document evolution of the thermodynamics, the dynamics and the composition of the SABL over north central Mauritania in response to an approaching Saharan heat low (SHL), which was migrating westward during that period (see Section 3.1). Flight F15 was conducted to document the SABL over northern Mauritania together with a dust plume transported from Algeria and associated with a Mediterranean wind surge.

The first three flights performed by the BAe146 on 17 and 18 June were a set of missions designed to investigate very strong low level winds over northern Mali (b600, b601 and b602). During these flights some of the largest particles encountered during Fennec were measured (see Section 4.1.1), and elevated dust concentrations were seen at altitudes beneath 1km, although vertical mixing played a role in the afternoon. The Falcon also flew on 17 June (F20) with a mission dedicated to the documentation the SABL over northern Mauritania and northern Mali, west of an approaching African easterly wave, as well as the structure the dust plume associated with a Mediterranean wind surge.

Flight b603 was a calibration flight performed over the Canary Islands at high altitudes under clear skies for the radiation instruments. Flight b604 was a LADUNEX EUFAR flight sampling dust which had been uplifted more than 24 hours previously by a MCS and associated haboob over Mali, and then transported over Mauritania by prevailing winds (Sodemann et al., 2015, accepted for publication), retaining giant mode dust particles despite large transport distances (Ryder et al., 2013a). The BAe146 crossed the dust front at high and low altitudes for in-situ and remote sensing measurements. F21 consisted of a long rectilinear flight across northern Mauritania and northern Mali to survey the SABL as well as document the dust uplift in the region of the intertropical discontinuity (ITD, i.e. the near surface convergence zone between the monsoon and the harmattan flow) to the south of the SHL, over Mali.

On 21 June both the Falcon and BAe146 performed 2 flights (b605, b606, F22 and F23). On the preceding day, convection over the Atlas Mountains had initiated a dust front which had propagated southwards over Mauritania by 21 June, with aged dust overlying it. During the day the layers became mixed together. Both aircraft missions' aimed to sample this dust and diurnal mixing, see Section 4.3.3. On 22 June, again, both aircraft performed missions in the morning and afternoon (b607, b608, F24 and F25). The missions were aimed at sampling the SHL and therefore flight tracks extended well into Mali (Figure 2). LIDAR, dropsondes and radiation instrumentation were used to sample the spatial and diurnal evolution of the SHL (see Engelstaedter et al. (2015)). F26 on 23 June performed a mission

dedicated to the study of the morning dust uplift over alluvial sources of Northern Mauritania in connection with the decay of the low-level jet (RAIN4DUST project).

From 24 June onwards, dust conditions were generally more well-mixed vertically with less fresh dust being sampled. Flight b609 on 24 June sampled dust and cumulus developing on the top of the dust layers (see Section 4.1.4). Flight b610 sampled the low level jet and dust uplift mechanisms over eastern Mauritania. b611 overflew the Zouerate ground supersite - see Section 4.2.2 for a comparison of in-situ measurements to sunphotometer retrievals. b612 and b613 on 26 June were missions to achieve radiative closure and to measure heat fluxes over the desert. Both were performed under clear sky conditions with a series of stacked runs, under low dust loadings. Flight b614 was a second flight to sample dust uplift and the low level jet early in the morning. Flight b615 on 28 June was the return transit to the UK, and included radiation calibration manoeuvres.

3.2.3 Flights during Fennec IOP 2012

Since the initial flying period during Fennec 2012 was initially dominated by Atlantic Inflow, with dust being observed at the confluence of this and Saharan air (see Section 3.1.3), most of the earlier flights aimed to sample this boundary (Table 7). b698 was a science transit from the UK to Fuerteventura, during which calibration manoeuvres for radiation instruments were performed. b699 and b700 were a pair of flights on 6 an 8 June which sampled the gradient of Atlantic Inflow and its eastern boundary at high and low levels over northern Mali and northern Mauritania. b701 and b702 were similar flights, but here the edge of the Atlantic inflow was contingent with the ITD, and larger dust loadings were sampled over central and southern Mauritania. Following b702 the BAe146 landed at Dakar, and then returned to Fuerteventura over the Atlantic (b703) sampling continental dust outflow. Flight b704 sampled Atlantic Inflow and the ITD again, this time measuring the highest submicron aerosol optical depths (AODs) of Fennec, 3.4 at 550nm, over southern Mauritania. b705 on 12 June was performed around midday to measure Saharan heat fluxes over a stable pressure gradient.

Flights b706 and b707 were a pair of flights examining dust uplift over the Mauritania/Mali border, with exactly the same track, and uplift beginning to happen under stronger winds during b707. b708 was designed to measure dust uplift by the LLJ over Mali under clear sky conditions so that the radiative impact of the dust could also be measured. This flight saw the highest scattering measurements on the nephelometer during the campaign (see Section 4.3.4), from dust at very low altitudes. By contrast, b709 on 17 June sampled dust which had been transported into the SHL and was well-mixed vertically up to 6km. This flight aimed to sample the pressure structure of the SHL and also perform radiative closure. b710 overflew the Zouerate ground supersite as part of SAVEX in order to compare AERONET (AERosol Robotic NETwork) retrievals and aircraft measurements of dust. Finally, b711 was a science transit return to the UK.

4 Key Scientific Results from the Fennec Airborne Programme

Here we present key scientific results from the Fennec airborne programme. They are grouped by dust characterisation (Section 4.1), Cross-platform assessment of dust measurements (Section 4.2), Dust uplift and transport (Section 4.3) and SABL processes, dynamics and interactions with dust (Section 4.4).

4.1 Dust Characterisation

4.1.1 Size distributions

During Fennec 2011 six different instruments were used to measure size distribution, as described in Section 2, covering the size range 0.1 to 300 µm diameter. Of these, the PCASP, CDP and CIP operated consistently during the whole campaign (see Rosenberg et al. (2012) for details of calibration and errors). Very large particles were measured during Fennec 2011, with effective diameter of the full size distribution ranging from 2.3 to 19.4 µm (Ryder et al., 2013b). Examples of different types of size distribution are shown in Figure 4. The solid lines show measurements from flight b600 at around 700 m above ground level, under aerosol optical depths greater than 3.0 at 550 nm when the dust was being actively uplifted by strong winds and was encountered beneath 1 km above ground level. These were some of the largest particles encountered during Fennec 2011, and the size distribution shows a strong coarse and giant mode present with a broad peak in volume concentration from around 10 to 60 µm. Contrastingly, b612 (dashed lines) shows more aged dust (24-48 hours based on satellite imagery) which was well-mixed within the SABL up to 5 km, with optical depths at 550 nm of around 0.6. Here there are fewer particles across all sizes upwards of 0.5 µm compared to b600, and the peak volume concentration is now at 10 µm diameter, reflecting a shift to lower number concentrations and fewer coarse particles as dust is mixed vertically through the entire SABL, and larger particles are deposited during transport as well as dispersion decreasing the total number concentration. Ryder et al. (2013a) examine the effects of vertical mixing and transport on dust properties further. Interestingly, at smaller sizes than 0.5 µm there are more particles in the case of b612, which gives the size distribution a flatter shape than b600. This may be due to different dust sources, soil types and uplift wind speeds acting initially.

For the first time on the FAAM BAe-146 all size resolved particle measurements were made with high temporal resolution (≥ 10 Hz) allowing correlation with vertical wind speed and measurements of the eddy covariance particle fluxes. This technique has been previously employed to derive heat, momentum and moisture fluxes from FAAM BAe-146 data (Petersen and Renfrew, 2009). During Fennec we have been able to resolve particle flux both in terms of eddy length scales and particle diameter. During flights b600, b601 and b602 upward particle fluxes were observed associated with synoptic scale wind in Algeria and northern Mali. Upward particle fluxes were also observed during flight b604 again associated with synoptic scale winds in this area. In general it has been found that particles above 10 µm diameter dominate the mass flux and in some cases particles above 100 µm diameter make a significant contribution. Full details are provided in Rosenberg et al. (2014).

4.1.2 Chemical Composition

To date, information on the mineralogical composition of coarse mineral dust can only be obtained by post-field analysis of filter samples. The mineralogical composition is a fundamental property determining the impacts on mineral dust on climate. It controls the complex refractive index, determining the radiation interactions in the shortwave and longwave spectrum (relevant to the direct radiative effect), the water uptake capability, determining the cloud and ice nuclei activation efficiency (relevant to the indirect radiative effect), the solubility in water, controlling the capability of deposited mineral dust to be assimilated by the marine phytoplankton, and the surface reactivity relevant to interactions with the gas phase (Formenti et al., 2011a; Scheuvens et al., 2013).

The mineralogical composition of mineral dust is obtained by X-ray diffraction (XRD) (Caquineau et al., 2002). Nonetheless, this technique is not always applicable to aircraft samples because of limited sampling times yielding light loadings which are incompatible with the detection limits of this analytical technique. Typically, about 800 µg of total dust mass are needed for analysis (Caquineau et al., 1997). As an order of magnitude, this requires at least 1 hour sampling at high volume (~50 L min^{-1}) for low to moderate atmospheric concentrations (< 200 µg m^{-3}) and at least half an hour for concentrations of the order of 200 µg m^{-3} and above.

Alternatively, useful indications on the mineralogical composition of mineral dust can be obtained by examining the concentrations of typical trace elements such as Al, Si, Fe, Ti, Ca, K, Mg, Na, which can be obtained by X-ray fluorescence techniques which have typical detection limits of 10 µg or less across a filter sample (Formenti et al., 2011b). In particular, the inter-elemental ratios provide indications of the origin of mineral dust. Typically, Al is used as a unique tracer as alumino-silicates dominate the dust mass. However, the Fe/Ca ratio has also proven useful to trace the origin of the dust plumes (Kandler et al., 2007; Formenti et al., 2011a; Scheuvens et al., 2013; Formenti et al., 2014).

Ninety-three samples are available in total from the Fennec 2011 and 2012 campaigns from the BAe146 (fifty-five and thirty-eight for each field phase, respectively). Samples have been collected in the Saharan boundary layer at altitudes ranging between 350 and 2700 m asl. The total dust concentrations, estimated as the sum of oxides of Na, Mg, Al, Si, K, Ca, P, Fe, and Ti, varied between 22 to 4012 µg m^{-3}.

The analysis of Dust Uplift Potential (DUP, section 4.3.1) restricted to the filter sampling legs suggests that the Fennec 2011 was characterized exclusively by emissions from Saharan sources in Algeria, West Sahara and Mauritania, with the exception of samples from b604 where dust had been uplifted by MCS outflow over Mali and transported by a large-scale haboob (Sodemann et al., 2015, accepted for publication). However, during the Fennec 2012 period additional emissions of Sahelian dust from convective activity in Mali constituted a much larger proportion of the samples. This contrast is a result of the dominant heat low west phase during the latter half of Fennec 2011 driving anomalous northeasterlies over western Algeria (Figure 3c, Section 3.1.2) compared to a northern extension of the monsoon flow over Mali during Fennec 2012 and increased MCS activity (Section 3.1.3).

The elemental composition is consistent with the DUPs indications for those source regions. This is shown in Figure 5a where the Fe/Ca and the Si/Al ratios obtained for the Fennec 2011 and Fennec 2012 samples are compared to those measured during the AMMA, DABEX, DODO and GERBILS campaigns summarized in (Formenti et al., 2014). As a consequence, and with the exception of samples collected during flights b699 and b700 when dust originated from the sources in the Algeria, Western Sahara and Mauritania areas, samples collected during Fennec 2012 had a lower Ca and Mg percent content with respect to Fennec 2011, reflecting the absence of calcium carbonates (calcite and dolomite) in Sahelian soils (Journet et al., 2014).

Likewise, there is a clear difference between the measured single scattering albedo (SSA) at 550 nm during Fennec 2011 and Fennec 2012 (Figure 5b). Even when excluding the outlier corresponding to a pollution plume encountered during flight b710 at Zouerate during Fennec 2012, when the single scattering albedo value averaged over the filter collection run was 0.91 (± 0.02), the mean single scattering albedo value for the Fennec 2012 period is lower than that for Fennec 2011 (0.94 ± 0.01 and 0.97 ± 0.01, respectively).

Future work will investigate the possible link between the changes in composition and optical properties during the 2011 and 2012 periods. This will also involve taking into account the particle size distribution, as a function of origin and of the age of the sampled air masses.

4.1.3 Column Aerosol Loading from in-situ Measurements

It is possible to use in-situ measurements of scattering and absorption by the nephelometer and PSAP on the BAe146 respectively to calculate extinction profiles, and hence AOD. Measurements are restricted firstly by the altitudes flown by the aircraft, which is usually between above the aerosol layer and as close to the surface as is safe and permissible. Depending on visibility, this varied between around 50 m to 1 km during Fennec. Secondly the measurements are restricted by the aircraft inlets, which do not sample particles larger than around 2 µm (Ryder et al., 2013b). The former has been accounted for by assuming that the aerosol profile is constant beneath the minimum aircraft altitude to the ground, while the latter is not accounted for and therefore the AODs presented here represent only extinction from the submicron size distribution, and are therefore an underestimate. Scattering and absorption measurements are corrected as described in Ryder et al. (2013b).

AODs from Fennec 2011 and 2012 are shown in Figure 6, with circles representing 2011 and diamonds 2012. AODs ranged from 0.2 to 3.6 at 550 nm. Of particular interest were a few heavy dust events which the aircraft sampled, including b600, b601 and b602 on 17 and 18 June 2011 in northern Mali (orange, red and green circles), during which very large dust particles were measured and dust fluxes have been calculated (as described in Section 4.1.1). Secondly, flights b707 (blue and green diamonds on Mali/Mauritania border) and b708 (orange diamonds in northern Mali) in 2012 sampled very high dust loadings, the first with very low altitude, fresh dust (see Section 4.3.4), and the second with dust well mixed to above 5 km, both under clear skies (i.e. no cloud). These flights will make excellent radiation closure case studies. Thirdly, we draw the reader's attention to the large number of profiles over the ocean between the land and Fuerteventura. The vertically resolved changes in particle size and optical properties between fresh, aged and oceanic profiles are examined by Ryder et al. (2013a), who find a significant reduction in particle size, number and associated changes in optical properties for dust measured over the ocean.

4.1.4 Dust-Cloud Interactions

Saharan clouds have the potential to be significantly different to other continental mid-latitude clouds due to the abundance of dust, which can act as ice nuclei (IN) and giant cloud condensation nuclei (GCCN), and the fact that the hot dry boundary layer prevents precipitation reaching the surface. Flight b609 on 24th June 2011 investigated a convective system in Northern Mauritania. According to analyses from the Met Office operational Africa Limited Area Model, an overnight monsoon surge associated with an easterly wave brought moist southerlies as far as 24˚N at 8˚W. Over the course of the day a linear convective feature formed, extending from 18.5˚N to link with a system over the Atlas Mountains at 30˚N. Dusty cold pool outflows, which affected supersite-2 (BBM), were visible in SEVIRI satellite imagery from at least 18 to 23 UTC. Flight b609 consisted of an overflight of the system and a series of north-south aligned legs at 8.0˚W between 23.8 and 25.8˚N on the eastern flank of the convective system from 12:42 to 15:36 UTC. The run locations were restricted by operational constraints.

Figure 7 shows the flight pattern and measurements. The flight path (thick black lines) consisted of an initial high-level leg, followed by a descent to minimum altitude and then three legs beneath the

clouds, each increasing in altitude to 4500m, just below cloud base (5400 to 5800 m). Once above cloud base, a series of short legs were performed targeting three cloud cells, with the aircraft finally ascending through the cloud tops at 8000 m. Cloud droplet concentration is shown in Figure 7 on top of the aircraft track, appearing red when the aircraft was in cloud. Range corrected Leosphere LIDAR backscatter signal is shown measured during the highest altitude aircraft leg, and is also shown beneath the aircraft descent where available, since the signal is strongly attenuated by the clouds along the high-level leg. Here we solely use the LIDAR measurements to describe the presence and structure of clouds present; not for the vertical distribution of dust, due to the strong attenuation of the LIDAR signal by the clouds.

The initial LIDAR observations indicated that cloud tops ranged from 6.1 km to above the aircraft altitude of 8.75 km, equivalent to approximately -11 to -28 ˚C (based on the profile measured during the descent). It was observed visually from the aircraft cockpit that the cloud tops had no observable anvil cirrus outflow. During descent to low level the aircraft passed through one isolated cloud at 24.18 ˚N. LIDAR observations of this cell 13 minutes prior to the intersection provided a cloud top height of 6.65 km, which is estimated to be at -15.0±0.2 ˚C. The LIDAR data showed no links to, or particle flow between, any other clouds. Particle images recorded by the CIP showed that this cloud consisted of pristine hexagonal plates. Freezing at this warm temperature is uncommon even for clouds in the vicinity of a source of IN (Kanitz et al., 2011; Ansmann et al., 2008; Sassen et al., 2003; Raymond and Blyth, 1989). An explanation could be the very high dust concentrations acting as IN in the heart of the Sahara.

The descent to 500 m provided a measurement of the aerosol input into the cloud. At the surface particle concentrations above 0.13 µm diameter measured by the PCASP and CDP ranged between 60 and 80 cm^{-3} south of 25.33 ˚N. North of this point the concentrations were 200 cm^{-3}. Note that most of this concentration is measured by the PCASP and therefore does not show up on the number concentration scale in Figure 7. As the aircraft climbed to cloud base the aerosol concentration fell to 40 cm^{-3}, although the number of particles above 4 µm diameter rose from 0.05 cm-3 to 0.15 cm^{-3}.

During ascent back towards cloud base sporadic ice precipitation was observed by the CIP probe from altitudes of 4.4 km (4 ˚C) and graupel was observed impacting the aircraft. Cloud was encountered at 5.75 km (-8 ˚C) although cloud base could have been slightly lower (minimum of 5.4 km or -5 ˚C). It is of note that cloud base may have been too cold for the Hallett-Mossop ice multiplication process which occurs around -6 ˚C. No columnar ice crystals typically produced by this process were observed. Near cloud base the cloud was found to be mixed phase with droplet number peaking at 250 cm^{-3} coincident with the peak updraft speed of 10 ms^{-1}. This measured droplet concentration was found to be significantly higher than the aerosol concentration reported by the PCASP and CDP below cloud base: the shortfall in CCN must have been made up of particles smaller than the PCASP detection limit. Twohy et al. (2009) showed that dust with zero hygroscopicity, κ, is entirely activated in cloud by a 10 ms^{-1} updraft and, because of their large size, can dominate the CCN population over other hygroscopic particles when they have a small but non-zero κ (Koehler et al., 2009). It is therefore likely that dust particles were acting as CCN or GCCN in this case. Higher in the cloud there is evidence of liquid water in updraft regions and near cloud top a population of homogeneously nucleated bullet rosettes were observed. No cirrus or precipitating particles were observed above cloud top.

These measurements have shown that dust is likely acting as a CCN and is acting as an IN at temperatures of -15 ˚C. Sampling of clouds earlier in their evolution would provide further limits on the effectiveness of dust as an IN. The lack of Hallett-Mossop in these clouds makes them a useful case for assessing IN concentrations and the extreme size of the dust particles may provide tests of the impact of GCCN.

For a non-precipitating cloud we expect that equivalent potential temperature, θ_e, and total water concentration (condensed plus vapour) are conserved and hence any point in cloud should lie on a mixing line or in a mixing region of these parameters (Paluch, 1979; Blyth et al., 1988). Here the cloud is precipitating meaning that total water concentration is no longer conserved but these variables are still useful in diagnosing the transport and mixing processes (Figure 8).

Much of the sampled in-cloud air had higher water content, greater than 5 g kg^{-1}, but similarly high ranges of θ_e compared to boundary layer air (Figure 8). These are inconsistent with clouds being a simple mixture of boundary-layer and entrained air. Out of cloud, above cloud base air had some regions consistent with simple mixing, some in a similar moist warm region to in-cloud air, but also some regions with low moisture content less than 1 g kg^{-1} and high θ_e similar to boundary layer air. Profiles of water vapour mixing ratio (WVMR) (Figure 7) show that in the boundary layer (below 2500-5000 m, varying from profile-to-profile) WVMR increases with altitude. Similar behaviour was also seen in the mean WVMR profile at Fennec supersite 1 (BBM) between 15 and 18 UTC, the time of maximum cloudiness (Marsham et al., 2013b). This is again inconsistent with simple mixing of a growing boundary layer. We hypothesise that in this low shear environment precipitation is evaporating in the boundary layer air but is not able to arrest the updraft allowing water to be recycled and concentrated in the cloud. High θ_e air rises in the boundary layer and receives extra water from evaporating precipitation, such that when it enters the cloud base it has more moisture than its environment. In cloud air parcels either precipitate adding to the recycled moisture reservoir before being detrained as dry, high θ_e air, or they do not precipitate and are instead detrained as moist, high θ_e air. We also expect dust and aerosol to be affected by this recycling process. Precipitation accumulates CCN and upon total evaporation releases them as a single aggregate particle. The increase in large dust particle concentration below cloud base is qualitatively consistent with this expectation. This concentrating of moisture and dust in the boundary layer top and the modification of the dust size distribution has implications for long range transport of these atmospheric constituents. To our knowledge these are the first observations of such a mechanism increasing the moisture content within the SABL mid-levels.

4.1.5 Dust-Ozone Interactions

Heterogeneous uptake of photochemical species leads to changes in the gas-phase composition of the atmosphere; affecting the global ozone budget (Bauer et al., 2004). Previous campaigns have observed ozone depletion during high dust loadings (de Reus et al., 2000; de Reus et al., 2005). These have also been investigated through modelling studies (Bian and Zender, 2003) and laboratory studies (Chang et al., 2005; Hanisch and Crowley, 2003). There is still some debate as to whether the removal of ozone is due to heterogeneous chemistry on the surface of the dust or a feature associated with a change in air mass between high and low dust loadings. The alkalinity of mineral dust has been shown to enhance the uptake of gases on the surface (Grassian, 2002). Bauer et al. (2004) propose that the coarse mode of mineral dust could be important for heterogeneous uptake; whilst Chang et al. (2005) found that there was no mass accommodation limitation to the rate of ozone uptake coefficients,

concluding that freshly emitted Saharan dust is potentially a significant route of ozone loss. Hanisch and Crowley (2003) discussed that mineral dust surface sites could be deactivated by the extended presence of ozone. Ultimately the change in the surface of mineral dust may have repercussions for subsequent aerosol-cloud interactions and modify the cloud nucleating properties of the mineral dust. A number of case studies observed during the Fennec campaigns were investigated Brooke (2014).

Fennec flight profiles provided the opportunity to sample very recently lofted mineral dust which will not have undergone significant atmospheric 'processing' and thus provide a good opportunity to investigate heterogeneous dust/ozone interactions. These observations of decreased ozone concentrations correspond with increased mineral dust surface area associated with elevated dust concentrations. Figure 9 presents box and whisker diagrams of mineral dust mean surface area correlated with ozone mass mixing ratios observed during b707, where dust uplift was encountered at the far eastern section of the flight track in Northern Mali (orange line in Figure 2d). The red central line of the box and whisker denotes the median, the edges of the box are the 25th and 75th percentiles and the whiskers extend to the most extreme data points. Mean surface areas of 0.15 to 0.35 $\mu m^2 cm^{-3}$ (roughly count median diameters from 0.22 to 0.33 μm) correspond to ozone mass mixing ratio of 49 – 52 ppb. As the mean dust surface area increases to 0.45 to 0.75 $\mu m^2 cm^{-3}$ (count median diameters from 0.38 to 0.49), the ozone mass mixing ratio decreases to 41 - 44 ppb. The spread in ozone concentrations at mean surface areas of 0.45 $\mu m^2 cm^{-3}$ is associated with crossing into a Harmattan airflow.

These in-situ observations suggest that increased mineral dust surface area associated with fresh dust uplift and a large coarse mode contribution to the size distribution act as a route for the reduced ozone concentrations. However, from the analysis presented here it is not possible to unequivocally conclude if the air mass initially contained lower ozone concentrations and mineral dust has subsequently been uplifted, or that mineral dust uplift could have contributed to the reduced ozone concentrations observed. There is scope within the Fennec dataset to further investigate airmass source regions, potentially with Lagrangian study methods.

4.2 Cross-Platform Assessment of Dust Measurements

4.2.1 Falcon LIDAR and Satellite Validation

Aircraft data can play an important role in validating satellite-based retrievals of AOD, covering a more extensive spatial area than that which is viewed from fixed ground-based measurements. Particularly useful in this regard are active remote sensing observations from LIDAR, since they can sample the full depth of the atmosphere below the aircraft instantaneously (i.e. a physical vertical profile by the aircraft is not required) and can provide vertically resolved information.

In Figure 10, middle panel, we show an example of the level of agreement seen between three different co-located measures of AOD, one provided at 532 nm by the LIDAR LNG on the F20, one from MODIS Aqua, derived using the Deep-Blue algorithm collection 5.1 (Hsu et al., 2004) and one from the SEVIRI instrument on Meteosat-9 (Brindley and Russell (2009); Banks and Brindley (2013)), both at a wavelength of 550 nm. Here we focus on an afternoon flight (F23, see Figure 2c) made by the Falcon on a track leading across to northern Mali from northern Mauritania on the 21st June 2011.

The satellite observations are co-located spatially with the LIDAR by averaging the satellite pixels within 25 km of each LIDAR pixel. Temporally, the Aqua satellite overpass time is always within 90

minutes of the aircraft observations, with a minimum time difference of 37 minutes. For SEVIRI we take advantage of the improved temporal sampling available from geostationary orbit such that each LIDAR observation is within 30 minutes of the corresponding satellite retrieval. The lower panel in the figure shows the vertical extinction coefficient derived from the LIDAR observations, while the top coloured band illustrates the colouring of the standard 'desert-dust' Red-Green-Blue (RGB) composite (Lensky and Rosenfeld, 2008) extracted from SEVIRI along the flight track.

Looking at the middle panel, the longitudinal behaviour of the AOD derived from all three instruments is generally in good agreement although SEVIRI tends to show consistently higher AODs than those derived from the LIDAR and from MODIS. The MODIS retrievals contain more data gaps as a result of various data quality tests: both the LIDAR and SEVIRI retrievals and the RGB composites suggest that these tests may be a touch severe as there is no clear evidence of a break in the aerosol layer or the presence of cloud. The intense pink colour of the composite at the western edge of the track would suggest the largest dust loadings are located here, associated with a thick dust plume at an altitude of ~3 km and another distinct layer observable at ~5.5 km seen in the LIDAR profile (which may have originated from Mali on the 19th). By the eastern end of the track, the AODs measured by MODIS, SEVIRI and the LIDAR are slightly smaller than the values seen at the western end, the dust is much more uniformly spread throughout the lowest 5 km or so of the atmosphere, and the intensity of the RGB signal is somewhat reduced.

Further work has explored co-located aircraft and satellite data in more detail, utilising a more extensive suite of satellite instruments (such as the MISR instrument on Terra and the IASI instrument on the METOP satellites (Banks et al., 2013), and between the BAe146 in-situ measurements and space-borne LIDAR CALIOP (Pappas et al., in prep.). In the former study the differences between retrievals have been investigated, including an evaluation of the sensitivity of the retrievals to variations in dust loading, as well as to atmospheric conditions (such as column water vapour), surface features (such as albedo), and to aerosol height. As diagnosed by Banks et al. (2013), when the dust loadings are high the SEVIRI retrievals appear most capable of retrieving the appropriate AODs, whereas the other retrievals are biased low. On the other hand the SEVIRI retrievals are most sensitive to meteorological conditions, especially column moisture, under high levels of which the SEVIRI retrieved AODs are biased high; meanwhile the MODIS Deep Blue and MISR aerosol retrievals appear to be relatively insensitive to such factors. The aircraft data will be of substantial benefit in interpreting the 'desert-dust' RGB imagery.

4.2.2 Comparison of AERONET and aircraft size distributions

Considering the wide application of size distributions from AERONET retrievals such as to aerosol models and climate forcing assessments (e.g. Garcia et al. (2012); Kinne et al. (2003)), it is of importance to validate AERONET retrievals where possible with field observations. Moreover, some discrepancies have been found between retrieved size-distributions using the AERONET algorithm (Dubovik and King, 2000; Dubovik et al., 2006) and the same size-distributions derived with the SKYRAD algorithm (Nakajima et al., 1996), as described in Campanelli et al. (2012) and Estellés et al. (2012b). The SAVEX project aims to explore these discrepancies, and has been motivated by studies such as Estellés et al. (2012a) and Estellés et al. (2012b), where differences between different sunphotometer retrieval algorithms are examined.

AERONET CIMEL sunphotometers were installed and operated at the two supersites of Zouerate (western Mauritania) and Bordj-Badii Mokhtar (BBM, Algeria) as part of the Fennec programme. As part of the SAVEX project, sunphotometers were also installed and operated at several different sites on Tenerife during June 2012 with the intention of overflying the instruments during dust events. However, overflights were not performed at Tenerife due a lack of dust outflow in this location during the campaign. The aircraft range from Fuerteventura did not permit overflights at BBM. Therefore overflights as close as possible to the Zouerate station under dusty conditions were performed during 2011 (b611, 25 June) and 2012 (b710, 18 June, SAVEX flight).

During these flights, profiles and stacked legs were performed to measure in-situ aerosol properties and radiative measurements, to allow radiative closure of the column above the ground site. Radiative flux measurements were also made at the ground site. Here we present some measurements from b611 in 2011. Dust sampled during this flight was around 19 to 43 h old, originating from Algeria (Ryder et al., 2013b), with AERONET AODs at 440nm from 0.8 to 0.94, and was relatively well mixed in the SABL up to around 5.5km, although extinction coefficient measurements from the aircraft approximately doubled beneath 2.5km. Similar measurements are available from flight b710, although for that flight layers of anthropogenic pollution were detected between dust layers, thus making comparisons between platforms more complicated, and are not shown here.

Figure 11 shows a comparison of the size distributions measured by the BAe146 compared to AERONET retrievals on 25 June 2011. The in-situ aircraft measurements are taken over a vertical profile close to Zouerate on 25 June 2011 between 8 km to 80 m AGL from 1558 to 1627 UTC. In-situ size distribution measurements shown in Figure 11 are therefore shown as the median, 10th and 90th percentiles between 80 m and 5.5 km.

Sunphotometer retrievals of size-distribution from almucantar scans are not present during much of the day due to cloud cover over Zouerate. Nevertheless, several retrievals are available during the morning (dark blue), one during the flight (black), and two from 18:06 and 18:30 after the aircraft had left the region (light blue). Size-distribution retrievals shown are those directly available from AERONET (L1.5, V2) and converted to dV/dlogD to match the aircraft measurements, and adjusted to measurements in cm^{-3} assuming the dust layer is distributed evenly over 5.5 km. Further work will examine measurements from aircraft legs at different altitudes, and different ways of representing a column-average measurement from the aircraft measurements, such extinction-weighted averaging.

The median aircraft measurements show a peak volume concentration at 12 µm, while the AERONET retrievals show peaks between 3 to 6 µm. This is consistent with previous aircraft-AERONET comparisons finding larger particles measured by aircraft (Reid et al., 2003; Müller et al., 2012; Müller et al., 2010b; McConnell et al., 2008). However, only one retrieval shows a peak volume concentration at 13 µm which appears to agree much more closely with the shape of the size distribution from the aircraft measurements. Satellite images show a small convective cloud developing close to, but not over Zouerate around this time. It is possible that small scale downdrafts produced some freshly uplifted dust which may have resulted in different size distribution retrievals. However, we cannot reject the possibility that optically thin cirrus cloud contamination affected the quality of this inversion (although it is not visible in satellite imagery), which would bias the size distribution towards larger sizes, and we note that the retrieval error is around double for this particular time compared to the others shown. At sizes smaller than 3 µm differences in volume concentration are substantial between

AERONET and the aircraft, with AERONET reporting more particles. Further work will explore possible factors causing this difference.

Rather few coarse particles were seen during b611 (towards the end of the campaign) relative to the rest of Fennec, perhaps due to the aged nature of the dust which meant that the largest particles had already been deposited. This is reflected by the absence of particles larger than 16 µm in the median, and the absence of particles larger than 45 µm in the 90th percentile (see the one CIP data point for the 90th percentile), though particles of these sizes *were* measured, but the standard deviation was very large, as shown by the large error bars on the median above sizes of 16 µm.

Existing publications show contrasting examples of agreement and disagreement between airborne, ground-based and AERONET size distributions, and there has been much debate over the causes. Reid et al. (2003) provide an overview of many commonly used sizing techniques and their limitations. These authors find that aerodynamic measurement methods and sunphotometer inversions tend to produce mass median diameters (MMDs) of around 3 µm diameter, while published OPC measurements at that time produced volume median diameters (VMDs) of order 8-13 µm. Limitations of OPCs, as described in Section 2.1.4, are principally uncertainties due to assumptions of refractive index, particle shape and the Mie response curve, the latter of which leads to a sizing ambiguity in the range 5 – 10 µm. As outlined in Section 2.1.4 we consider uncertainty due to particle shape to be small (as evidenced by similar size distributions resulting from OPCs measuring over different scattering angles), and we provide error bars to account for the remaining uncertainties. Aerodynamic measurement systems, such as Aerodynamic Particle Sizers (APS) and cascade impactors rely on particle dynamic shape factor, which varies with dust particle shape, causing uncertainties in the size distribution and may undersize particles by 25% for dynamic shape factors of 1.2. These instruments are also impacted by cut-offs of larger particle sizes imposed by inlets. Open path OPC instruments such as the CDP and CIP do not suffer from inlet effects, but do have uncertainties in their measurement volume. Cascade impactors can also be affected by particles bouncing off substrates. Thus each measurement technique has its own advantages and disadvantages. Reid et al. (2003) found for dust aerosol at Puerto Rico, that AERONET and APS size distributions agreed well with MMD at around 3.5 µm, while OPC size distributions produced a VMD of 9 µm. Reid et al. (2003) conclude that OPC data are most likely to have the largest biases based principally on the response function and uncertainty/variability in particle refractive index and shape. However, no attempt was made by Reid et al. (2003) to determine uncertainties in the size distributions due to the response function or the uncertain refractive index. This error analysis has been rigorously performed here, and is represented in the error bars in Figures 4 and 11. Additionally, data from the CIP, which uses light shadowing techniques rather than light scattering techniques as with the OPCs, further increases confidence in the shape of the Fennec size distribution presented by the CDP data.

Reid et al. (2006) compared aircraft OPC measurements to surface-based APS observations in a sea-salt aerosol dominated environment, and drew similar conclusions to Reid et al. (2003). AERONET size distribution inversions were also found to compare favourably to APS surface measurements. However, in this sea-salt environment, aerosols are not likely to reach such large sizes as was observed during Fennec – the precise size range which poses challenges for sunphotometer retrievals, and additionally the inlet to the APS had a cut point of around 12 µm in this case. Finally, Reid et al. (2008) report observations of dust from the United Arab Emirates in 2004. The authors found that AERONET

and APS size distributions agreed well, although here the inlet cut point to the APS was around 10 µm, thus excluding measurements in the exact size range challenging to AERONET retrievals.

Congrastingly, other previous work (Müller et al., 2012; Müller et al., 2010b; McConnell et al., 2008) has found relative disagreement between aircraft and AERONET size distribution retrievals for dust, finding that AERONET retrievals significantly undersize dust. In some of these cases detailed radiative closure has been achieved, validating OPC observations when a reasonable coarse mode was sampled, both for dust (Osborne et al., 2011; Müller et al., 2010b; Müller et al., 2010a) and for volcanic ash (Turnbull et al., 2012; Newman et al., 2012). Thus despite the contrasting conclusions concerning AERONET size distributions, it is important to repeat these closure flights in dusty environments.

Additionally, AERONET size distribution retrievals are subject to their own set of limitations and associated errors. Firstly, maximum diameter extends only to 30 µm and the tails of the size distributions are constrained to very small values (Hashimoto et al., 2012), and encounter large errors (Dubovik and King, 2000) which are dependent on the particle size. As noted in Estellés et al. (2012b), for the diameter interval 0.2 to 14 µm, the retrieval errors do not exceed 10% in the maxima but could increase up to 35% in the minima. Outside this intermediate range the errors increase, rising up to 80–100% or higher for diameters less than 0.2 µm and greater than 14 µm (Dubovik et al., 2002).

Unfortunately the flights during Fennec when large particles were strongly evident did not take place close to AERONET sites, due to the remoteness of the flight locations. Ryder et al. (2013b) find that particle sizes are larger close to dust sources in remote locations, and Ryder et al. (2013a) show that giant particles (d>37.5 µm) are a feature of freshly uplifted dust events, and some long-range transported cases. This should act as a caution for using AERONET retrievals as a basis for dust size distributions over the central Sahara, particularly since they only extend to 30 µm diameter and the tails of the size distributions are constrained to very small values (Hashimoto et al., 2012). Further studies will examine aircraft and sun-photometer data from both 25 June 2011 and 18 June 2012, in terms of in-situ aircraft measurements, airborne and ground-based radiation measurements, and using both the AERONET and SKYRAD retrievals for the inversion of sun-photometer radiances.

4.3 Dust Uplift and Transport

4.3.1 Dust source areas from Dust Uplift Potential

It is relevant for several areas of dust measurement analysis to identify the sources of dust sampled during research flights (e.g. Section 4.1.2). Lagrangian backward trajectory calculations with the FLEXPART model (Stohl et al., 2005) have been initiated in 'tropospheric curtains' run along the track of each research flight to investigate the sources of the dust sampled. For this a large number of virtual air parcels (1000) were released at a 30 s interval in a vertical column between the surface and a pressure of 200 hPa along the flight tracks. Each parcel was tracked for 3 days backward in time using ECMWF analysis winds at a 1ºx1º horizontal grid spacing. We utilize the metric of dust uplift potential (DUP), defined as $fU^3(1+U_t/U)(1-U_t^2/U^2)$, with f being the desert and bare soil fraction, the wind velocity U, and the threshold velocity U_t=6.5 ms^{-1} (Marsham et al., 2011). Despite being a simplified representation of likely dust uplift (e.g. variations in soil moisture are neglected, and dust uplift may not be linear with threshold velocity (Kok et al., 2014), DUP is a useful indicator of where likely uplift occurred and is relatively easily computed. DUP was calculated along the three-day back-trajectories for locations where the tracked air parcels were within the boundary layer. DUP values were gridded on a 0.25°x0.25° grid and integrated over time. The DUP thus calculated for the tropospheric column

at the aircraft location characterises the airmass as measured by the onboard LIDARs when the BAe146 and Falcon were flying at high altitudes. During lower flight legs this analysis enables interpretation of in-situ dust measurements with respect to their mobilisation conditions and source regions.

Figure 12 shows the composite of the DUP from (a) all the Fennec 2011 Falcon flights, (b) Fennec 2011 BAe146 flights and (c) Fennec 2012 BAe146 flights. The areas contributing to the sampled air masses, which experienced strong winds that would be associated with dust uplift for dust-source regions (i.e. high DUP areas) were mostly located in a NE-SW oriented swath extending from central Algeria to northern Mali and Mauritania during 2011. This dominant pattern is related to the inflow into the Saharan heat low, as shown by the 925 hPa winds in Figure 3c over southwest Algeria. DUP locations from 2012 suggest more southerly dust sources, from southern Mauritania, stretching to the Mali-Algeria-Niger triple point, and along the Mali-Algeria border towards southern Libya. This is consistent with additional convective activity in Mali driving emissions which were more Sahelian-dominated during 2012 (Section 3.1.3).

Individual flights exhibit additional sources and substantial variability (see supplementary material for DUP maps for individual flights). For example, dust from more southerly sources in Mali and Mauritania was intercepted during flights b600-602, b604-b606, b608, b611 and b614. Dust from northern Niger was sampled during flight b607. Note that the connection to dust filter samples to this figure is not immediate, because only the DUP for the selected legs corresponding to the filter sampling duration and position are considered in that case (see Section 4.1.2). We note that DUP from events associated with convective downdrafts such as haboobs may not be accurately represented due to the ECMWF analyses not fully capturing these events (Marsham et al., 2011). For example, this is the case for b604, where a large MCS generated a haboob over Mali which subsequently travelled towards Mauritania (Sodemann et al., 2015, accepted for publication). Therefore in situations where dust has potential to have been uplifted by events associated with convection, back trajectories and more generally operational meteorological analysis and forecast data should not be used in isolation to determine dust source regions. For example, a combination of analysis of SEVIRI RGB satellite imagery and Lagrangian methods can be used to ensure consistency with observations (e.g. Ryder et al. (2013b)).

4.3.2 Heavy dust loadings from a low-level jet breakdown over northern Mali

One particularly notable flight was b600 during the morning of 17th June 2011, under which the highest dust loadings observed during Fennec 2011 and very large particles were measured. This was followed by flight b601 in the afternoon, and b602 the following morning in the same region. At this time the SHL was centred on the Mali-Algeria-Niger triple point, producing strong low-level northeasterlies through Algeria to northern Mali, which were particularly pronounced on the morning of the 17th (b600, Figure 13c, d, e). A region of slacker winds in Mauritania was associated with moisture remaining from the monsoon flow. Flights b600 to b602 were aimed at sampling these airmasses, travelling out at high-level to descend into the strong winds in northern Mali and returning northwestwards at low-level into the moister airmass (Figure 13a, b). In-situ aircraft profile measurements are shown in Figure 14.

Forecasts showed a pronounced decrease in the strong 925 hPa winds in northern Mali from 06 to 09 UTC, with a corresponding increase in 10 m winds, consistent with the downward mixing of

momentum from the nocturnal LLJ around the SHL, likely deflected around the Hoggar mountains (Birch et al., 2012). The existence of a LLJ is confirmed by the observation from the b600 descent into Mali (Figure 14, black) of a wind-maximum of 16.7ms^{-1} at a pressure height of 1700m (1400m AGL), located above the growing turbulent moist and dusty CBL found below 1400m AGL. The dust number and mass concentrations below 1400m were the highest observed during the Fennec 2011 campaign with particularly large particles observed during b600 and b601; the size distribution during the initial part of the horizontal run in the dusty CBL following the profile descent of b600 can be seen in Figure 4, with particles present up to nearly 300 μm. The high dust concentrations are consistent with the very high extinction measurements from the nephelometer and PSAP, of over 1250Mm^{-1} in both profile descents (Figure 14). By the time of the profile descent of b601 at approximately 1700Z the dust had been mixed up into a CBL that reached 3.7 km (Figure 14, red), with no remaining LLJ. The upwards vertical mixing of the dust resulted in the 'pinkness' in the SEVIRI images (Figure 13a, b) becoming more pronounced by the time of the second flight (the RGB product is sensitive to dust altitude, Brindley et al. (2012)). Flight b601 then travelled back under the moist convection developing over Mauritania, with some precipitation observed falling onto the aircraft, but no extensive cold-pool outflows at the aircraft altitude at this time.

To the authors' knowledge this is the first airborne observation of dust size distributions (including the presence of coarse and giant particles) measured under uplift conditions caused by the breakdown of the Saharan nocturnal LLJ. Flights b706, b707 and b708 (Section 4.3.4) from 2012 also collected in-situ measurements of dust under LLJ breakdown conditions, thus providing scope for further analysis.

4.3.3 In-situ sampling of an aged Haboob

Recent studies have shown that haboobs (dust fronts occurring at the leading edge of cold pools emanating from convective storms) are a significant source of dust over the Sahara and Sahel (Flamant et al., 2007; Knippertz et al., 2007; Schepanski et al., 2009; Tulet et al., 2010). For example, Marsham et al. (2008b), Marsham et al. (2013b) and Allen et al. (2013) show that haboobs cause around 50% of dust uplift in the summertime Sahara, contributing to the seasonal cycle in dustiness. Radiosonde observations show that the transport of cold moist air in haboobs was a major cause of global model forecast bias at the Fennec BBM supersite in June 2011 (Garcia-Carreras et al., 2013), consistent with the role of haboobs diagnosed from convection-permitting simulations (Marsham et al., 2013a).

On 21 June 2011, aircraft measurements were taken over and through an aged haboob emanating from convection over the Atlas Mountains in Morocco (Kocha et al., 2013). The cold pool passed over dust sources and uplifted large quantities of dust. The haboob was observed over the central Sahara over northern Mauritania and northern Mali in the morning with the LNG LIDAR on the Falcon 20 during flight F22 (see Figure 2b).

The haboob appears as the layer characterized by large extinction coefficient values at pressure heights beneath 1.5 km (Figure 15a). The aerosol optical thickness (AOT) derived from the LIDAR extinction coefficient profiles reached an average of 1 around 0900 UTC. At the same time, the BAe146 flew through the haboob to directly sample its characteristics during flight b605. In-situ measurements from the BAe146 show that the dust concentration and observed extinction in the cold pool air increased by a factor of around three compared to its environment. The number of large particles of size around 10 μm increased to 0.1 cm^{-3}μm^{-1} (not shown). The properties of the dust sampled during this event also had a significant impact on the radiative fluxes within the haboob. For instance, the

downward shortwave flux measured by the BAe146 decreased by 100 Wm^{-2} when entering the dusty cold pool (Figure 15b).

In the afternoon, both aircraft sampled the growth of the SABL again (flights F23 and b606) as the haboob was mixed into the Saharan residual layer above. An unambiguous influence of the haboob composition and thermodynamics was observed on the development of the SABL (Kocha et al., 2013). Simulations with and without dust are being used to investigate role of the haboob on the dynamics/thermodynamics on the development of the SABL over the central Sahara.

4.3.4 Radiation observations during dust uplift

Several flights were performed during Fennec to use aircraft in-situ aerosol measurements and radiative measurements to allow the potential to achieve radiative closure and examine the radiative properties of dust. Flight b708 on 16 June 2012 aimed to observe freshly uplifted dust at the time of downwards mixing of strong LLJ winds to the surface which was forecast to uplift dust over the Mali/Mauritania border. Additionally since clouds were absent, the flight aimed to attain radiative closure measurements since the dust loadings were high but with very low altitude dust, with AODs at 550nm of 0.54 and 1.92 measured during the two aircraft profiles by the nephelometer and the PSAP.

Figure 16b shows information from the aircraft profiles – extinction calculated from corrected scattering and absorption measurements is shown for the descent (black) and ascent (red) in Mali. During this flight, the aircraft flew a high level leg at 7.5km for radiative measurements, followed by a profile down to minimum safe altitude, which was around 100m above ground level (AGL) initially (see black line in Figure 16a). During the descent the aircraft entered the dust layer at around 900 m. At this time the dust was not visible in the SEVIRI RGB desert dust imagery, despite an AOD of 0.54, likely because the RGB imagery is sensitive to dust altitude (Brindley et al., 2012). Absence of a 'pink' signal in the SEVIRI RGB imagery during active dust uplift such as occurred during this flight would have major implications for dust source maps that have previously been created based on this imagery (e.g. Schepanski et al. (2007)). Following the descent, the aircraft flew a low level leg. Figure 16a shows the extinction as a function of longitude. As the aircraft flew eastwards the amount of dust increased until visibility was so poor that the aircraft had to ascend to 400m AGL. Despite this, extinction continued to increase to the east, with a maximum of 5500Mm^{-1}, the highest value ever observed from the FAAM nephelometer and PSAP.

At the end of the low level leg, the aircraft ascended (red line in Figure 16b). The dashed lines in Figure 16b show potential temperature, which show inversions at the height of the rapid increases in dust extinction. This is one example of many during Fennec, where the dust was encountered in a low layer, which was gradually mixed upwards during the day as the SABL grew. The red line in Figure 16a shows the measured downwelling shortwave irradiance (SWD) during the low level run. Note that during the legs (around 30 minutes) the solar zenith angle decreased so that SWD would be expected to increase with increasing longitude. Instead during the western portion of the leg, SWD decreases with increasing extinction (dust above the aircraft). During the eastern portion of the leg there is a notable drop in SWD of around 150 Wm^{-2} at around -5.7W at the same time as the peak in extinction. This flight, as well as b709 in the SHL where dust was well-mixed vertically up to 5km, will be used to examine the radiative effect of dust over the Sahara under different dust conditions (low level, well-

mixed vertically) further, using the spectral radiation instruments SHIMS, ARIES and SWS on the BAe146 in conjunction with radiative transfer models and satellite observations.

4.4 Boundary Layer Processes, Dynamics and Interactions with Dust

4.4.1 LIDAR and Dropsonde Observations

Combining LIDAR observations and dropsonde-derived atmospheric profiles allows for a detailed analysis of the spatial and vertical structure of the atmosphere as well as the boundary layer processes that control the emission, vertical mixing and transport of mineral dust. Flights b607 and b608 were part of an extensive survey of the troposphere in the SHL region with the aim a) to characterise the spatial variability the SHL, CBL, monsoon inflow and dust distribution in the central Sahara, b) to analyse how these features change throughout the day, and c) to assess the processes that control these features and dust dynamics. Both flights followed a straight track crossing from northern Mauritania into Mali in the morning of 22 June 2011 (see Figure 2c for b607 flight track; the afternoon flight b608 overlies b607). The aircraft sampled the flight track twice in the morning (b607) and the afternoon (b608) allowing the evolution of the atmosphere over time to be studied. Dropsonde measurements were obtained during the out and return flight at fixed locations. Dropsonde data were interpolated to reference times at each location thereby creating a snapshot of the state of the atmosphere in the study region at the reference times. Engelstaedter et al. (2015) analysed the observed SHL characteristics and evaluated the performance of the UK Met Office limited area model for Africa (Africa-LAM). They identified two moisture transport pathways, one curving around the SHL core in the north (especially pronounced in a morning near-surface layer), and the other going towards the northeast within the roughly 2 km deep monsoon surge. The deep afternoon CBL simulated by the Africa-LAM in the monsoon surge region (more than twice as deep as observations) suggests a significant model error due to moisture being vertically mixed into northeasterly flow above about 2 km.

As an example for the combination of observations from different instruments Figure 17 shows Leosphere LIDAR and dropsonde-derived data from BAe146 flight b607.

The range corrected LIDAR signal (see Section 2.1 for more detail on the LIDAR measurements) is shown here as coloured blocks and has a vertical resolution of 45 m and an integration time of 1 min. It is used here as an indicator for the presence of dust and clouds in the atmosphere but limitations apply. For instance, attenuation of the laser beam when it passes through an elevated dust layer can limit the LIDAR's ability to detect dust at lower levels. Dropsonde observations allow for the identification of atmospheric structures such as the top of the CBL and SRL as well as temperature inversions. The CBL depth was determined by locating the altitude in the sonde profile (from the surface upwards) where the potential air temperature (θ) first reaches 0.3°C above the value at 150 m above the surface. In cases where θ increased monotonically from the surface up to 150 m, the surface θ value was used as a reference. The top of the SRL was determined manually where possible by identifying a sharp decrease in water vapour mixing ratio coinciding with a sharp increase in θ. The resulting CBL and SRL tops were linked by solid lines in Figure 17 in order to illustrate spatio-temporal changes of these features. The depth of air temperature inversions, defined as an increase in air temperature with altitude, are indicated as grey boxes along the vertical sonde tracks together with the inversion strength in $^{o}C\ km^{-1}$ (Figure 17).

Dropsonde-derived near surface winds ranging between 11 and 17 ms^{-1} observed during the b607 outgoing flight (not shown) led to local dust emissions observed by the LIDAR at about 7.3°W (also seen in LIDAR depolarization data, not shown) that were prevented from upward mixing by a low-level temperature inversion (Figure 17a). At that time in the morning, the CBL was still relatively shallow (mostly <1 km deep), the top of the SRL varied between about 4.3 and 5.5 km above MSL, and an aged dust layer of varying intensity could be identified close to the SRL top. Cloud development was identified west of 11°W in the LIDAR data. In the time that passed between the outgoing and return flight, surface emissions ceased and the CBL grew up to about 4.5 km above MSL (B4, Figure 17b) as a result of increasing near surface temperatures. East of about 7.5°W, the CBL was prevented from growing deep by temperature inversions and the influence of monsoon flow (not shown). Clouds continued to develop west of about 10.5°W. CBL growth rates can be calculated for each dropsonde location based on the two dropsonde profiles. The SRL top showed little change compared to the outward leg apart from at B4 where the SRL was consumed completely by the fast growing CBL (Figure 17). It should be noted that SEVIRI imagery did not show any dust presence along the flight tracks on this day suggesting that the LIDAR dust signal represents background dust levels – some dust is almost always present over North Africa at this time of year (Israelevich et al., 2003).

As part of this SHL survey, the Falcon 20 took measurements at the same time as the BAe146 but on a more southern track (flight F24 in Figure 2b). The analysis of the combined aircraft data showed that the SHL had an elongated shape with a NE-SW orientation. Moisture from the monsoon inflow was transported around the SHL at low levels in the morning. These unique measurements allow for the first time to challenge climate models in the SHL region and to understand the processes that control the observed temporal and spatial variability.

4.4.2 First observations of the vertical profile of SABL fluxes and mesoscale circulations in the SABL

The Saharan atmospheric boundary layer (SABL) is probably the deepest on Earth, commonly reaching 5-6 km, and is crucial in controlling the vertical redistribution and transport of dust, moisture, heat and momentum fluxes in the Sahara (Cuesta et al., 2009). Before Fennec, aircraft observations and radiosondes (Cuesta et al., 2009; Messager et al., 2010; Marsham et al., 2013b) had shown the persistence of a deep near-neutral Saharan residual layer (SRL) over large areas of the Sahara throughout the day, with only a very small temperature inversion separating the SRL from the CBL below. Flamant et al. (2007) and Messager et al. (2010) had shown that the SRL may have a maximum humidity mixing ratio at its upper levels, and that small errors in model representation of this humidity can have substantial consequences in terms of relative humidity, cloud cover and, therefore, radiation. This unusual structure of the SABL means that relatively small perturbations to CBL temperature (e.g. from a surface albedo anomaly) are expected to have significant impacts on vertical mixing and perhaps induce circulations that may affect the CBL in neighbouring regions. There was evidence of such effects in observations from the CBL (Marsham et al., 2008a) and in modeling studies (Birch et al., 2012; Huang et al., 2010), but observations of impacts on the SRL were lacking. Observations from Fennec BBM supersite 1 showed that when the CBL does reach 5 or 6 km this tends to only happen between 15 and 18 UTC (Marsham et al., 2013b). Fennec flights have provided new insights into the vertical structure of and mixing within the SABL (see Garcia-Carreras et al. (2015) including schematic (their Figure 14) and SABL mesoscale circulations (below)).

During Fennec, aircraft LIDAR and in-situ observations were used to better understand the vertical stratification and transport mechanisms within the SABL, as well as its temporal and spatial variability (Garcia-Carreras et al., 2015). In order to sample the vertical turbulent structure of the SABL during Fennec, stacked legs were performed at different heights, determined from inspecting dropsonde profiles launched at both ends of the leg before descending. Each run was at least 10 times the SABL depth (≥ 60 km) and took place between 13-15LT, when sensible heating was maximum. Heat fluxes were computed from the stacked legs, as well as the ascents and descents, taking advantage of the shallow angle of the aircraft profiles. These indicate that entrainment fluxes are very weak, as a result of detrainment at the CBL top. This is a result of the weak temperature inversion, and high vertical velocity of overshooting parcels, which are characteristic of the SABL, and can explain the slow development of the CBL despite the strong surface heating. LIDAR measurements from high-level runs also showed that the boundary layer depth can vary by up to 100% over distances of a few kilometres due to turbulent processes alone, so that any given dropsonde profile may not be representative of the whole run.

Figure 18 shows an example from a flight where small variations in heating from an albedo anomaly appear to be generating mesoscale circulations within the SABL. Figure 18 shows the vertical extinction coefficient at 532 nm retrieved with the LIDAR LNG on 20th June 2011 (1405-1446 UTC, flight F21, see Figure 2b) from the Falcon flying southeastward in Mauritania, with water vapour mixing ratio (WVMR) and wind profiles from four dropsondes overplotted. The LIDAR transect highlights a number of BL processes of importance encountered during the Fennec campaign, showing variability from the turbulent to the synoptic scales, as described below.

At the synoptic scale, there is a temperature and humidity gradient across the transect, with warmer and drier conditions in the northwest (by ~5 K and 7 g/kg), leading to a deeper CBL compared to the southeast (4 km at 24°N compared with 2 km at 21°N). The monsoon flow at night reached approximately 20˚N along the flight-track, bringing in cool moist air into the southern end of the transect (from UK Met Office analysis, not shown), which was then redistributed vertically as the CBL grew during the day. The more spatially homogeneous residual layer, on the other hand, reflects the conditions from the day before; the monsoon front on the night of the 19th was considerably further south, leading to a deep CBL throughout the transect. Superimposed on the synoptic gradient there is substantial variability in the SABL depth and structure. Variability at the turbulent eddy scale can be observed in the northern end of the transect (24.5-25.2˚N), with changes in the depth of the well-mixed aerosol layer (and so the CBL) of ~1km over short horizontal distances (5-10km, ~0.05 to 0.1˚), consistent with idealised simulations and LIDAR measurements described in Garcia-Carreras et al. (2015).

At the mesoscale, there is a region with cloud and deeper BLs at the boundary between the warm, dry conditions in the northwest, and the moister conditions in the southeast (21.4-22.5˚N), with an orange plume reaching 6 km at 22.2N. Satellite imagery shows that the clouds observed by the LIDAR are part of a band of clouds coincident with a negative albedo anomaly of around 0.2 that is just west of the flight-track at 21.6˚N (red line, Figure 18). The surface hot-spot leads to a local increase in the CBL depth, cloud formation and an upward transport of dust. The impact of another smaller hot-spot can be observed at 22.8°N. Easterly winds in the SRL in the southeast lead to the airmass overriding the deeper CBL in the northwest, potentially contributing to the cloud formation. The 3 gkg-1 contour in Figure 18 has been drawn using the dropsonde data and the LIDAR-inferred aerosol distribution and

suggests that the deeper CBL around 22˚N acts to transport water vapour and dust directly to the top of the SRL, where it spreads laterally, capping the adjacent CBL and leading to weak maxima in water vapour mixing ratios at the top of the SRL in the three eastern dropsondes. This supports the hypotheses of Marsham et al. (2008a) and Messager et al. (2010) of mesoscale variability in the SABL and its role in the transport of CBL air into the RL, with implications for the long-range transport of dust.

4.4.3 North American wildfire emissions measured over Africa

Approximately 15 pollutant plumes were observed on the BAe146 in the upper troposphere (6 to 8.5 km altitude) above the Sahara desert during the Fennec campaign in June 2011. Using HYSPLIT trajectory analysis and MODIS satellite fire products, four source regions were identified for these pollutant plumes: flaring from oil fields in Algeria and biomass burning in the southern USA, Venezuela and West Africa. The pollutant plumes displayed high concentrations of ozone and sub-micron particles, with differing characteristics from each source region. Values for the single scattering albedo ranged from 0.57 to 0.99 and for the Angstrom exponent from -0.85 to 2.44 for individual plumes. If the HYSPLIT trajectory calculations are robust (uncertain due the substantial errors identified in the vertical wind fields), it is believed this is the first aircraft measurement of flaring from oil fields and may require further research attention: this is planned in the forthcoming DACCIWA field campaign in southern West Africa.

5 Conclusions

We have presented a description of the Fennec airborne fieldwork of 2011 and 2012 over the western Sahara, in order to provide a reference and context for published and future articles. Secondly we have presented new scientific results which have developed from the airborne measurements to show how the exploitation of aircraft measurements can deepen our understanding of weather, climate and dust processes over remote regions of the Sahara not otherwise accessible. Finally, the Fennec airborne data provide the only comprehensive resource of in-situ Saharan observations with which to develop the science linking dust, dynamics and radiation in the central Sahara. Along with the ground-based and satellite measurements, these will be heavily exploited in the coming years, and therefore we have provided a detailed overview of the data and its context.

The research areas and key findings of published articles relating to the Fennec aircraft observations are summarized in Table 8. We emphasize the measurement of giant mode dust particles using Cloud Imaging Probes (up to 300 µm during Fennec 2011 and 6200 µm during Fennec 2012), and the advancement of technologies such that size distribution measurements across the full size range at 10Hz were possible (Rosenberg et al., 2012). The former has been used to demonstrate a significant presence of particles sized larger than 10 µm over remote parts of the Sahara, including providing uncertainties in the size distribution due to refractive index assumption and the degenerate Mie response curve. Volume distributions peaked between 10 to 60 µm in many fresh, heavy dust cases while the peak volume distribution shifted to 10 to 20 µm in more aged dust events with a reduction in total concentrations (Ryder et al., 2013a, b). The measurement of size distributions at 10Hz has allowed dust fluxes in the SABL to be measured from an aircraft for the first time (Rosenberg et al., 2014).

The new scientific findings presented in this article are as follows:

- During the second half of June 2011 sources over central Algeria dominated, driven primarily by stronger easterlies associated with the westward movement of the SHL, in contrast to the second half of June 2012 when more Sahelian dust sources dominated due to a northern extension of the monsoon flow and increased MCS and cold pool activity over Mali. This is associated with differences in the chemical composition and optical property results between campaigns, which show higher dust absorption and lower calcium content in 2012 compared to 2011, characteristic of dust emitted from Sahelian soils. This change in composition and associated dust absorption can have significant radiative impacts which can be driven by dust uplift locations and the dominant meteorology. These first results of dust chemical composition in the SHL region indicate the importance of large scale meteorology in affecting dust composition and therefore radiative properties.
- Comprehensive aerosol and cloud instrumentation on the BAe146 has been used to explore the interaction between dust layers and clouds, indicating that dust particles are likely to be acting as CCN and also as IN at temperatures of -15°C.
- Ozone concentrations have been compared to size distribution measurements of surface area in an attempt to determine the role of dust on ozone depletion. Results suggest that coarser, fresher dust particles can provide a route to decrease ozone concentrations, though in this case a change of air mass during sampling prevented unequivocal attribution.
- Dust uplift under the breakdown of the nocturnal LLJ has been observed, including its impact on shortwave irradiance and the presence of coarse and giant particles in these very fresh dust events, which are observed at low altitudes and often before they become visible in SEVIRI imagery.
- F20 LIDAR measurements have been combined with BAe146 in-situ extinction and vertically resolved shortwave flux measurements to describe the influence of a haboob thermodynamics on the development of the SABL, and subsequent mixing of the haboob through the SABL.
- Combined LIDAR and dropsonde observations show the spatial and diurnal structure of the SHL. The CBL develops throughout the day while the influence of the southerly monsoon flow restricts this growth. Variability in the SABL plays an important role in the transport of CBL air into the SRL, which has implications for long range transport of dust, with evidence of surface albedo features driving such variability.
- Vertical profiles of turbulent fluxes have revealed unusual characteristics of entrainment and detrainment of thermals in the deep, dry SABL, which are a challenge for BL schemes in global models.
- Unique in-situ observations suggest that precipitation is recycled as it is evaporated into BL air that feeds clouds (a common feature of the SABL), increasing the total water content of subsequent clouds and increasing the moisture content at mid-levels in the SABL. Observations suggest cloud-processing of dust and subsequent evaporation alters the size distribution of dust.
- In one case, a comparison of aircraft LIDAR data with satellite measurements from SEVIRI and MODIS show good agreement as to the spatial distribution of dust but disagree as to the loading, which may be indicative of different sensitivities to varying meteorological conditions. Further detailed comparisons have taken place (see Table 8), demonstrating the value of aircraft-satellite validation studies.

- A comparison of column mean size distributions between AERONET and the BAe146 in-situ measurements shows AERONET retrieved peak volume size distributions at 3-6 microns, while aircraft measurements measured more coarse mode, with a peak at 12 microns. This was in a dust event with low concentrations of coarse and giant particles present – the aircraft frequently encountered cases with a greater coarse mode present. We propagated uncertainties due to calibration, Mie response curve and refractive index in the aircraft optical particle counter size distribution measurements to clearly display uncertainties to the reader. Measurements from the shadow-based CIP further increased confidence in the aircraft size distributions. Contrasting evidence exists in the literature regarding validity of AERONET dust size distribution retrievals. This work adds to the evidence that AERONET derived size distributions should be used with caution when coarse dust particles are present, and merits further detailed comparisons under heavy dust loadings.

This paper demonstrates that the Fennec airborne campaign has delivered a novel, rich dataset through the operation of two aircraft over remote regions of the Sahara. The power of these aircraft measurements will be enhanced via combination with the ground-based measurements available from the Fennec climate program, providing a unique resource for further in-depth study of the vital SHL region of the Sahara. These will be further exploited through the Fennec Earth observation and modelling programs.

Acknowledgements

Core project funding for Fennec was from the UK Natural Environmental Research Council (NERC) under grant NE/G017166/1. In addition, it received support from the NERC National Centre for Atmospheric Science (NCAS), the Agence Nationale de la Recherche (ANR n°2010 BLAN 606 01), the Institut National des Sciences de l'Univers (INSU/CNRS) through the LEFE program, the Centre National d'Etudes Spatiales (CNES) through the TOSCA program and Météo-France. Airborne data from the BAe146 was obtained using the BAe-146-301 Atmospheric Research Aircraft operated by Directflight Ltd and managed by FAAM, which is a joint entity of the NERC and the UK Met Office. Airborne data from the F20 was obtained using the Falcon 20 Environment Research Aircraft operated and managed by SAFIRE, which is a joint entity of CNRS, Météo-France & CNES. EUFAR (EUropean Facility for Airborne Research) is acknowledged for its support to the RAIN4DUST Falcon-20 flights and LADUNEX BAe146 flights. The UK Met Office is acknowledged for funding of flight b710 through SAVEX. SAVEX ground deployment at Tenerife was possible thanks to RIMA/AERONET and AEMET infrastructure; and support from Juan de la Cierva (JCI-2009-04455), Universidad de La Laguna (2012/0001624), MICIIN (CGL2012_33294) and Generalitat Valenciana (PROMETEO/2010/064) projects. Many other scientists and engineers were involved in the gathering of this outstanding dataset. Additional partners include: Directflight, AvalonAero, FAAM (Facility for Airborne Atmospheric Measurements), SAFIRE (Service des Avions Français Instrumentés pour la Recherche en Environnement), UK Met Office, and DMN Maroc. MODIS data used in this paper were produced with the LAADS online data system, developed and maintained by NASA Goddard, and we also acknowledge the MODIS scientists and associated NASA personnel for the production of the data used in this research effort. Flight forecasting would not have been possible without the model products made available especially for the Fennec project particularly the UK Met Office, the Météo-France AROME model team and the DREAM model team.

References

Allen, C. J. T., Washington, R., and Engelstaedter, S.: Dust emission and transport mechanisms in the central Sahara: Fennec ground-based observations from Bordj Badji Mokhtar, June 2011, J Geophys Res-Atmos, 118, 6212-6232, Doi 10.1002/Jgrd.50534, 2013.

Ansmann, A., Tesche, M., Althausen, D., Muller, D., Seifert, P., Freudenthaler, V., Heese, B., Wiegner, M., Pisani, G., Knippertz, P., and Dubovik, O.: Influence of Saharan dust on cloud glaciation in southern Morocco during the Saharan Mineral Dust Experiment, J Geophys Res-Atmos, 113, Doi 10.1029/2007jd008785, 2008.

Ansmann, A., Tesche, M., Knippertz, P., Bierwirth, E., Althausen, D., Muller, D., and Schulz, O.: Vertical profiling of convective dust plumes in southern Morocco during SAMUM, Tellus B, 61, 340-353, DOI 10.1111/j.1600-0889.2008.00384.x, 2009.

Ansmann, A., Petzold, A., Kandler, K., Tegen, I., Wendisch, M., Müller, D., Weinzierl, B., Müller, T., and Heintzenberg, J.: Saharan Mineral Dust Experiments SAMUM-1 and SAMUM-2: what have we learned?, Tellus B, 63, 403-429, DOI 10.1111/j.1600-0889.2011.00555.x, 2011.

Banks, J. R., and Brindley, H. E.: Evaluation of MSG-SEVIRI mineral dust retrieval products over Africa and the Middle East, Remote Sensing of Environment, 128, 58-73, doi:10.1016/j.rse.2012.07.017, 2013.

Banks, J. R., Brindley, H. E., Flamant, C., Garay, M. J., Hsu, N. C., Kalashnikov, O. V., Kluser, L., and Sayer, A. M.: Intercomparison of satellite dust retrieval products over the west African Sahara during the Fennec campaign in June 2011, Remote Sensing of Environment, 136, 99-116, DOI 10.1016/j.rse.2013.05.003, 2013.

Bauer, S. E., Balkanski, Y., Schulz, M., Hauglustaine, D. A., and Dentener, F.: Global modeling of heterogeneous chemistry on mineral aerosol surfaces: Influence on tropospheric ozone chemistry and comparison to observations, J Geophys Res-Atmos, 109, doi 10.1029/2003jd003868, 2004.

Baumgardner, D., Jonsson, H., Dawson, W., O'Connor, D., and Newton, R.: The cloud, aerosol and precipitation spectrometer: a new instrument for cloud investigations, Atmos Res, 59, 251-264, 2001.

Bian, H. S., and Zender, C. S.: Mineral dust and global tropospheric chemistry: Relative roles of photolysis and heterogeneous uptake, J Geophys Res-Atmos, 108, Doi 10.1029/2002jd003143, 2003.

Birch, C. E., Parker, D. J., Marsham, J. H., and Devine, G. M.: The effect of orography and surface albedo on stratification in the summertime Saharan boundary layer: Dynamics and implications for dust transport, J Geophys Res-Atmos, 117, Doi:10.1029/2011jd015965, 2012.

Blyth, A. M., Cooper, W. A., and Jensen, J. B.: A Study of the Source of Entrained Air in Montana Cumuli, J Atmos Sci, 45, 3944-3964, Doi 10.1175/1520-0469(1988)045<3944:Asotso>2.0.Co;2, 1988.

Brindley, H., Knippertz, P., Ryder, C., and Ashpole, I.: A critical evaluation of the ability of the Spinning Enhanced Visible and Infrared Imager (SEVIRI) thermal infrared red-green-blue rendering to identify dust events: Theoretical analysis, J Geophys Res-Atmos, 117, Doi 10.1029/2011jd017326, 2012.

1449 Brindley, H. E., and Russell, J. E.: An assessment of Saharan dust loading and the corresponding
1450 cloud-free longwave direct radiative effect from geostationary satellite observations, J Geophys Res-
1451 Atmos, 114, Doi 10.1029/2008jd011635, 2009.

1452 Brooke, J. K.: Airborne Observations of the Physical and Optical Properties of Atmospheric
1453 Aerosol, PhD, School of Earth and Environment, University of Leeds, 2014.

1454 Campanelli, M., Estelles, V., Smyth, T., Tomasi, C., Martinez-Lozano, M. P., Claxton, B., Muller, P.,
1455 Pappalardo, G., Pietruczuk, A., Shanklin, J., Colwell, S., Wrench, C., Lupi, A., Mazzola, M., Lanconelli,
1456 C., Vitale, V., Congeduti, F., Dionisi, D., Cardillo, F., Cacciani, M., Casasanta, G., and Nakajima, T.:
1457 Monitoring of Eyjafjallajokull volcanic aerosol by the new European Skynet Radiometers (ESR)
1458 network, Atmos Environ, 48, 33-45, DOI 10.1016/j.atmosenv.2011.09.070, 2012.

1459 Caquineau, S., Magonthier, M. C., Gaudichet, A., and Gomes, L.: An improved procedure for the
1460 X-ray diffraction analysis of low-mass atmospheric dust samples, Eur J Mineral, 9, 157-166, 1997.

1461 Caquineau, S., Gaudichet, A., Gomes, L., and Legrand, M.: Mineralogy of Saharan dust
1462 transported over northwestern tropical Atlantic Ocean in relation to source regions, J Geophys Res-
1463 Atmos, 107, Doi 10.1029/2000jd000247, 2002.

1464 Chang, R. Y. W., Sullivan, R. C., and Abbatt, J. P. D.: Initial uptake of ozone on Saharan dust at
1465 atmospheric relative humidities, Geophys Res Lett, 32, 10.1029/2005gl023317, 2005.

1466 Chauvin, F., Roehrig, R., and Lafore, J. P.: Intraseasonal Variability of the Saharan Heat Low and Its
1467 Link with Midlatitudes, J Climate, 23, 2544-2561, Doi 10.1175/2010jcli3093.1, 2010.

1468 Chazette, P., Dabas, A., Sanak, J., Lardier, M., and Royer, P.: French airborne lidar measurements
1469 for Eyjafjallajokull ash plume survey, Atmos Chem Phys, 12, 7059-7072, DOI 10.5194/acp-12-7059-
1470 2012, 2012.

1471 Cuesta, J., Edouart, D., Mimouni, M., Flamant, P. H., Loth, C., Gibert, F., Marnas, F., Bouklila, A.,
1472 Kharef, M., Ouchene, B., Kadi, M., and Flamant, C.: Multiplatform observations of the seasonal
1473 evolution of the Saharan atmospheric boundary layer in Tamanrasset, Algeria, in the framework of
1474 the African Monsoon Multidisciplinary Analysis field campaign conducted in 2006, J Geophys Res-
1475 Atmos, 113, 10.1029/2007jd009417, 2008.

1476 Cuesta, J., Marsham, J. H., Parker, D. J., and Flamant, C.: Dynamical mechanisms controlling the
1477 vertical redistribution of dust and the thermodynamic structure of the West Saharan atmospheric
1478 boundary layer during summer, Atmos Sci Lett, 10, 34-42, Doi 10.1002/Asl.207, 2009.

1479 de Reus, M., Dentener, F., Thomas, A., Borrmann, S., Strom, J., and Lelieveld, J.: Airborne
1480 observations of dust aerosol over the North Atlantic Ocean during ACE 2: Indications for
1481 heterogeneous ozone destruction, J Geophys Res-Atmos, 105, 15263-15275, Doi
1482 10.1029/2000jd900164, 2000.

1483 de Reus, M., Fischer, H., Sander, R., Gros, V., Kormann, R., Salisbury, G., Van Dingenen, R.,
1484 Williams, J., Zollner, M., and Lelieveld, J.: Observations and model calculations of trace gas
1485 scavenging in a dense Saharan dust plume during MINATROC, Atmos Chem Phys, 5, 1787-1803,
1486 2005.

1487 de Villiers, R. A., Ancellet, G., Pelon, J., Quennehen, B., Schwarzenboeck, A., Gayet, J. F., and Law,
1488 K. S.: Airborne measurements of aerosol optical properties related to early spring transport of mid-

1489 latitude sources into the Arctic, Atmos Chem Phys, 10, 5011-5030, DOI 10.5194/acp-10-5011-2010,
1490 2010.

1491 Dubovik, O., and King, M. D.: A flexible inversion algorithm for retrieval of aerosol optical
1492 properties from Sun and sky radiance measurements, J Geophys Res-Atmos, 105, 20673-20696, Doi
1493 10.1029/2000jd900282, 2000.

1494 Dubovik, O., Holben, B., Eck, T. F., Smirnov, A., Kaufman, Y. J., King, M. D., Tanre, D., and Slutsker,
1495 I.: Variability of absorption and optical properties of key aerosol types observed in worldwide
1496 locations, J Atmos Sci, 59, 590-608, Doi 10.1175/1520-0469(2002)059<0590:Voaaop>2.0.Co;2, 2002.

1497 Dubovik, O., Sinyuk, A., Lapyonok, T., Holben, B. N., Mishchenko, M., Yang, P., Eck, T. F., Volten,
1498 H., Munoz, O., Veihelmann, B., van der Zande, W. J., Leon, J. F., Sorokin, M., and Slutsker, I.:
1499 Application of spheroid models to account for aerosol particle nonsphericity in remote sensing of
1500 desert dust, J Geophys Res-Atmos, 111, Doi 10.1029/2005jd006619, 2006.

1501 Dunion, J. P., and Velden, C. S.: The impact of the Saharan air layer on Atlantic tropical cyclone
1502 activity, B Am Meteorol Soc, 85, 353-+, Doi 10.1175/Bams-85-3-353, 2004.

1503 Engelstaedter, S., Tegen, I., and Washington, R.: North African dust emissions and transport,
1504 Earth-Sci Rev, 79, 73-100, DOI 10.1016/j.earscirev.2006.06.004, 2006.

1505 Engelstaedter, S., Washington, R., Flamant, C., Parker, D. J., Allen, C. J. T., and Todd, M. C.: The
1506 Saharan heat low and moisture transport pathways in the central Sahara – multi-aircraft
1507 observations and Africa-LAM evaluation, J Geophys Res-Atmos, 10.1002/2015JD023123, 2015.

1508 Estellés, V., Campanelli, M., Smyth, T. J., Utrillas, M. P., and Martinez-Lozano, J. A.: Evaluation of
1509 the new ESR network software for the retrieval of direct sun products from CIMEL CE318 and PREDE
1510 POM01 sun-sky radiometers, Atmos. Chem. Phys., 12, 11619–11630, doi:10.5194/acp-12-11619-
1511 2012, 2012a.

1512 Estellés, V., Campanelli, M., Utrillas, M. P., Exposito, F., and Martinez-Lozano, J. A.: Comparison of
1513 AERONET and SKYRAD4.2 inversion products retrieved from a Cimel CE318 sunphotometer, Atmos
1514 Meas Tech, 5, 569-579, DOI 10.5194/amt-5-569-2012, 2012b.

1515 Evan, A. T., Vimont, D. J., Heidinger, A. K., Kossin, J. P., and Bennartz, R.: The Role of Aerosols in
1516 the Evolution of Tropical North Atlantic Ocean Temperature Anomalies, Science, 324, 778-781, DOI
1517 10.1126/science.1167404, 2009.

1518 Evan, A. T., Foltz, G. R., Zhang, D. X., and Vimont, D. J.: Influence of African dust on ocean-
1519 atmosphere variability in the tropical Atlantic, Nat Geosci, 4, 762-765, Doi 10.1038/Ngeo1276, 2011.

1520 Evan, A. T., Flamant, C., Fiedler, S., and Doherty, S.: An analysis of aeolian dust in climate models,
1521 Geophys Res Lett, doi:10.1002/2014GL060545, 2014.

1522 Flamant, C., Chaboureau, J. P., Parker, D. J., Taylor, C. A., Cammas, J. P., Bock, O., Timouk, F., and
1523 Pelon, J.: Airborne observations of the impact of a convective system on the planetary boundary
1524 layer thermodynamics and aerosol distribution in the inter-tropical discontinuity region of the West
1525 African Monsoon, Q J Roy Meteor Soc, 133, 1175-1189, Doi 10.1002/Qj.97, 2007.

1526 Formenti, P., Rajot, J. L., Desboeufs, K., Said, F., Grand, N., Chevaillier, S., and Schmechtig, C.:
1527 Airborne observations of mineral dust over western Africa in the summer Monsoon season: spatial

and vertical variability of physico-chemical and optical properties, Atmos Chem Phys, 11, 6387-6410, DOI 10.5194/acp-11-6387-2011, 2011a.

Formenti, P., Schütz, L., Balkanski, Y., Desboeufs, K., Ebert, M., Kandler, K., Petzold, A., Scheuvens, D., Weinbruch, S., and Zhang, D.: Recent progress in understanding physical and chemical properties of African and Asian mineral dust, Atmos Chem Phys, 11, 8231-8256, DOI 10.5194/acp-11-8231-2011, 2011b.

Formenti, P., Caquineau, S., Desboeufs, K., Klaver, A., Chevaillier, S., Journet, E., and Rajot, J. L.: Mapping the physico-chemical properties of mineral dust in western Africa: mineralogical composition, Atmos. Chem. Phys., 14, 10663-10686, doi:10.5194/acp-14-10663-2014, 2014.

Forster, P., Ramaswamy, V., Artaxo, P., Berntsen, T., Betts, R., Fahey, D. W., Haywood, J. M., Lean, J., Lowe, D. C., Myhre, G., Nganga, J., Prinn, R., Raga, G., Schulz, M., and Van Dorland, R.: Changes in Atmospheric Constituents and in Radiative Forcing, in: Climate Change 2007: The Physical Science Basis, in: Contribution of Working Group I to the Fourth Assessment Report of the Intergovernmental Panel on Climate Change, edited by: Solomon, S., Qin, D., Manning, M., Chen, Z., Marquis, M., Averyt, K. B., Tignor, M., and Miller, H. L., Cambridge University Press, Cambridge, UK, 2007.

Garcia-Carreras, L., Marsham, J. H., Parker, D. J., Bain, C. L., Milton, S., Saci, A., Salah-Ferroudj, M., Ouchene, B., and Washington, R.: The impact of convective cold pool outflows on model biases in the Sahara, Geophys Res Lett, 40, 1647-1652, Doi 10.1002/Grl.50239, 2013.

Garcia-Carreras, L., Parker, D. J., Marsham, J. H., Rosenberg, P. D., Brooks, I. M., Lock, A. P., Marenco, F., McQuaid, J. B., and Hobby, M.: The Turbulent Structure and Diurnal Growth of the Saharan Atmospheric Boundary Layer, J Atmos Sci, 72, 693-713, 10.1175/Jas-D-13-0384.1, 2015.

Garcia, O. E., Diaz, J. P., Exposito, F. J., Diaz, A. M., Dubovik, O., Derimian, Y., Dubuisson, P., and Roger, J. C.: Shortwave radiative forcing and efficiency of key aerosol types using AERONET data, Atmos Chem Phys, 12, 5129-5145, DOI 10.5194/acp-12-5129-2012, 2012.

Grassian, V. H.: Chemical reactions of nitrogen oxides on the surface of oxide, carbonate, soot, and mineral dust particles: Implications for the chemical balance of the troposphere, J Phys Chem A, 106, 860-877, Doi 10.1021/Jp012139h, 2002.

Gross, S., Tesche, M., Freudenthaler, V., Toledano, C., Wiegner, M., Ansmann, A., Althausen, D., and Seefeldner, M.: Characterization of Saharan dust, marine aerosols and mixtures of biomass-burning aerosols and dust by means of multi-wavelength depolarization and Raman lidar measurements during SAMUM 2, Tellus B, 63, 706-724, DOI 10.1111/j.1600-0889.2011.00556.x, 2011.

Hanisch, F., and Crowley, J. N.: Ozone decomposition on Saharan dust: an experimental investigation, Atmos Chem Phys, 3, 119-130, 2003.

Hashimoto, M., Nakajima, T., Dubovik, O., Campanelli, M., Che, H., Khatri, P., Takamura, T., and Pandithurai, G.: Development of a new data-processing method for SKYNET sky radiometer observations, Atmos Meas Tech, 5, 2723-2737, DOI 10.5194/amt-5-2723-2012, 2012.

Haywood, J. M., Pelon, J., Formenti, P., Bharmal, N., Brooks, M., Capes, G., Chazette, P., Chou, C., Christopher, S., Coe, H., Cuesta, J., Derimian, Y., Desboeufs, K., Greed, G., Harrison, M., Heese, B., Highwood, E. J., Johnson, B., Mallet, M., Marticorena, B., Marsham, J. H., Milton, S., Myhre, G., Osborne, S. R., Parker, D. J., Rajot, J. L., Schulz, M., Slingo, A., Tanre, D., and Tulet, P.: Overview of

the Dust and Biomass-burning Experiment and African Monsoon Multidisciplinary Analysis Special Observing Period-0, J Geophys Res-Atmos, 113, Doi 10.1029/2008jd010077, 2008.

Haywood, J. M., Johnson, B. T., Osborne, S. R., Baran, A. J., Brooks, M., Milton, S. F., Mulcahy, J., Walters, D., Allan, R. P., Klaver, A., Formenti, P., Brindley, H. E., Christopher, S., and Gupta, P.: Motivation, rationale and key results from the GERBILS Saharan dust measurement campaign, Q J Roy Meteor Soc, 137, 1106-1116, Doi 10.1002/Qj.797, 2011a.

Haywood, J. M., Johnson, B. T., Osborne, S. R., Mulcahy, J., Brooks, M. E., Harrison, M. A. J., Milton, S. F., and Brindley, H. E.: Observations and modelling of the solar and terrestrial radiative effects of Saharan dust: a radiative closure case-study over oceans during the GERBILS campaign, Q J Roy Meteor Soc, 137, 1211-1226, Doi 10.1002/Qj.770, 2011b.

Heintzenberg, J.: The SAMUM-1 experiment over Southern Morocco: overview and introduction, Tellus B, 61, 2-11, DOI 10.1111/j.1600-0889.2008.00403.x, 2009.

Highwood, E. J., Northway, M. J., McMeeking, G. R., Morgan, W. T., Liu, D., Osborne, S., Bower, K., Coe, H., Ryder, C., and Williams, P.: Aerosol scattering and absorption during the EUCAARI-LONGREX flights of the Facility for Airborne Atmospheric Measurements (FAAM) BAe-146: can measurements and models agree?, Atmos Chem Phys, 12, 7251-7267, DOI 10.5194/acp-12-7251-2012, 2012.

Hobby, M., Gascoyne, M., Marsham, J. H., Bart, M., Allen, C., Engelstaedter, S., Fadel, D. M., Gandega, A., Lane, R., McQuaid, J. B., Ouchene, B., Ouladichir, A., Parker, D. J., Rosenberg, P., Ferroudj, M. S., Saci, A., Seddik, F., Todd, M., Walker, D., and Washington, R.: The Fennec Automatic Weather Station (AWS) Network: Monitoring the Saharan Climate System, J Atmos Ocean Tech, 30, 709-724, Doi 10.1175/Jtech-D-12-00037.1, 2013.

Hsu, N. C., Tsay, S. C., King, M. D., and Herman, J. R.: Aerosol properties over bright-reflecting source regions, Ieee T Geosci Remote, 42, 557-569, Doi 10.1109/Tgrs.2004.824067, 2004.

Huang, Q., Marsham, J. H., Parker, D. J., Tian, W. S., and Grams, C. M.: Simulations of the effects of surface heat flux anomalies on stratification, convective growth, and vertical transport within the Saharan boundary layer, J Geophys Res-Atmos, 115, Doi 10.1029/2009jd012689, 2010.

Huneeus, N., Schulz, M., Balkanski, Y., Griesfeller, J., Prospero, J., Kinne, S., Bauer, S., Boucher, O., Chin, M., Dentener, F., Diehl, T., Easter, R., Fillmore, D., Ghan, S., Ginoux, P., Grini, A., Horowitz, L., Koch, D., Krol, M. C., Landing, W., Liu, X., Mahowald, N., Miller, R., Morcrette, J. J., Myhre, G., Penner, J., Perlwitz, J., Stier, P., Takemura, T., and Zender, C. S.: Global dust model intercomparison in AeroCom phase I, Atmos Chem Phys, 11, 7781-7816, DOI 10.5194/acp-11-7781-2011, 2011.

Israelevich, P. L., Ganor, E., Levin, Z., and Joseph, J. H.: Annual variations of physical properties of desert dust over Israel, J Geophys Res-Atmos, 108, 10.1029/2002jd003163, 2003.

Jenkins, G. S., Pratt, A. S., and Heymsfield, A.: Possible linkages between Saharan dust and tropical cyclone rain band invigoration in the eastern Atlantic during NAMMA-06, Geophys Res Lett, 35, Doi:10.1029/2008gl034072, 2008.

Jickells, T. D., An, Z. S., Andersen, K. K., Baker, A. R., Bergametti, G., Brooks, N., Cao, J. J., Boyd, P. W., Duce, R. A., Hunter, K. A., Kawahata, H., Kubilay, N., laRoche, J., Liss, P. S., Mahowald, N., Prospero, J. M., Ridgwell, A. J., Tegen, I., and Torres, R.: Global iron connections between desert dust, ocean biogeochemistry, and climate, Science, 308, 67-71, 2005.

1610 Johnson, B., Turnbull, K., Brown, P., Burgess, R., Dorsey, J., Baran, A. J., Webster, H., Haywood, J.,
1611 Cotton, R., Ulanowski, Z., Hesse, E., Woolley, A., and Rosenberg, P.: In situ observations of volcanic
1612 ash clouds from the FAAM aircraft during the eruption of Eyjafjallajokull in 2010, J Geophys Res-
1613 Atmos, 117, Doi 10.1029/2011jd016760, 2012.

1614 Journet, E., Balkanski, Y., and Harrison, S. P.: A new data set of soil mineralogy for dust-cycle
1615 modeling, Atmos Chem Phys, 14, 3801-3816, DOI 10.5194/acp-14-3801-2014, 2014.

1616 Kandler, K., Benker, N., Bundke, U., Cuevas, E., Ebert, M., Knippertz, P., Rodriguez, S., Schutz, L.,
1617 and Weinbruch, S.: Chemical composition and complex refractive index of Saharan Mineral Dust at
1618 Izana, Tenerife (Spain) derived by electron microscopy, Atmos Environ, 41, 8058-8074, DOI
1619 10.1016/j.atmosenv.2007.06.047, 2007.

1620 Kanitz, T., Seifert, P., Ansmann, A., Engelmann, R., Althausen, D., Casiccia, C., and Rohwer, E. G.:
1621 Contrasting the impact of aerosols at northern and southern midlatitudes on heterogeneous ice
1622 formation, Geophys Res Lett, 38, Doi 10.1029/2011gl048532, 2011.

1623 Kim, D., Chin, M., Yu, H. B., Diehl, T., Tan, Q., Kahn, R. A., Tsigaridis, K., Bauer, S. E., Takemura, T.,
1624 Pozzoli, L., Bellouin, N., Schulz, M., Peyridieu, S., Chedin, A., and Koffi, B.: Sources, sinks, and
1625 transatlantic transport of North African dust aerosol: A multimodel analysis and comparison with
1626 remote sensing data, J Geophys Res-Atmos, 119, 6259-6277, Doi 10.1002/2013jd021099, 2014.

1627 Kinne, S., Lohmann, U., Feichter, J., Schulz, M., Timmreck, C., Ghan, S., Easter, R., Chin, M.,
1628 Ginoux, P., Takemura, T., Tegen, I., Koch, D., Herzog, M., Penner, J., Pitari, G., Holben, B., Eck, T.,
1629 Smirnov, A., Dubovik, O., Slutsker, I., Tanre, D., Torres, O., Mishchenko, M., Geogdzhayev, I., Chu, D.
1630 A., and Kaufman, Y.: Monthly averages of aerosol properties: A global comparison among models,
1631 satellite data, and AERONET ground data, J Geophys Res-Atmos, 108, Doi 10.1029/2001jd001253,
1632 2003.

1633 Knippertz, P., Deutscher, C., Kandler, K., Muller, T., Schulz, O., and Schutz, L.: Dust mobilization
1634 due to density currents in the Atlas region: Observations from the Saharan Mineral Dust Experiment
1635 2006 field campaign, J Geophys Res-Atmos, 112, Doi 10.1029/2007jd008774, 2007.

1636 Knollenberg, R. G.: The optical array: An alternative to scattering or extinction for airborne
1637 particle size determination, J Appl Meteorol, 9, 86-103, doi:10.1175/1520-0450, 1970.

1638 Kocha, C., Flamant, C., Berckmens, J., Fink, A., Garcia-Carreras, L., Knippertz, P., Lafore, J.-P.,
1639 Marnas, F., Marsham, J. H., Parker, D. J., Rosenberg, P., Ryder, C. L., Tulet, P., and Washington, R.:
1640 How can a dusty cold pool change the diurnal evolution of the Saharan Boundary Layer?, EGU 2013,
1641 Vienna, 2013.

1642 Koehler, K. A., Kreidenweis, S. M., DeMott, P. J., Petters, M. D., Prenni, A. J., and Carrico, C. M.:
1643 Hygroscopicity and cloud droplet activation of mineral dust aerosol, Geophys Res Lett, 36, Doi
1644 10.1029/2009gl037348, 2009.

1645 Kok, J. F., Mahowald, N. M., Fratini, G., Gillies, J. A., Ishizuka, M., Leys, J. F., Mikami, M., Park, M.
1646 S., Park, S. U., Van Pelt, R. S., and Zobeck, T. M.: An improved dust emission model - Part 1: Model
1647 description and comparison against measurements, Atmos Chem Phys, 14, 13023-13041, DOI
1648 10.5194/acp-14-13023-2014, 2014.

1649 Lacis, A. A., and Mishchenko, M. I.: Climate forcing, climate sensitivity, and climate response: A
1650 radiative modeling perspective on atmospheric aerosols, Dahl Ws Env, 17, 11-42, 1995.

1651 Lance, S., Medina, J., Smith, J. N., and Nenes, A.: Mapping the operation of the DMT Continuous
1652 Flow CCN counter, Aerosol Sci Tech, 40, 242-254, Doi 10.1080/02786820500543290, 2006.

1653 Lavaysse, C., Flamant, C., Janicot, S., Parker, D. J., Lafore, J. P., Sultan, B., and Pelon, J.: Seasonal
1654 evolution of the West African heat low: a climatological perspective, Clim Dynam, 33, 313-330, DOI
1655 10.1007/s00382-009-0553-4, 2009.

1656 Legrand, M., Pietras, C., Brogniez, G., Haeffelin, M., Abuhassan, N. K., and Sicard, M.: A high-
1657 accuracy multiwavelength radiometer for in situ measurements in the thermal infrared. Part I:
1658 Characterization of the instrument, J Atmos Ocean Tech, 17, 1203-1214, Doi 10.1175/1520-
1659 0426(2000)017<1203:Ahamrf>2.0.Co;2, 2000.

1660 Lensky, I. M., and Rosenfeld, D.: Clouds-Aerosols-Precipitation Satellite Analysis Tool (CAPSAT),
1661 Atmos Chem Phys, 8, 6739-6753, 2008.

1662 Liu, P. S. K., Leaitch, W. R., Strapp, J. W., and Wasey, M. A.: Response of Particle Measuring
1663 Systems Airborne Asasp and Pcasp to Nacl and Latex-Particles, Aerosol Sci Tech, 16, 83-95, Doi
1664 10.1080/02786829208959539, 1992.

1665 Mahowald, N., Albani, S., Kok, J. F., Engelstaeder, S., Scanza, R., Ward, D. S., and Flanner, M. G.:
1666 The size distribution of desert dust aerosols and its impact on the Earth system, Aeolian Res, 15, 53-
1667 71, DOI 10.1016/j.aeolia.2013.09.002, 2014.

1668 Marenco, F., Amiridis, V., Marinou, E., Tsekeri, A., and Pelon, J.: Airborne verification of CALIPSO
1669 products over the Amazon: a case study of daytime observations in a complex atmospheric scene,
1670 Atmos Chem Phys, 14, 11871-11881, DOI 10.5194/acp-14-11871-2014, 2014.

1671 Marsham, J. H., Parker, D. J., Grams, C. M., Johnson, B. T., Grey, W. M. F., and Ross, A. N.:
1672 Observations of mesoscale and boundary-layer scale circulations affecting dust transport and uplift
1673 over the Sahara, Atmos Chem Phys, 8, 6979-6993, 2008a.

1674 Marsham, J. H., Parker, D. J., Grams, C. M., Taylor, C. M., and Haywood, J. M.: Uplift of Saharan
1675 dust south of the intertropical discontinuity, J Geophys Res-Atmos, 113, Doi 10.1029/2008jd009844,
1676 2008b.

1677 Marsham, J. H., Knippertz, P., Dixon, N. S., Parker, D. J., and Lister, G. M. S.: The importance of the
1678 representation of deep convection for modeled dust-generating winds over West Africa during
1679 summer, Geophys Res Lett, 38, Doi 10.1029/2011gl048368, 2011.

1680 Marsham, J. H., Dixon, N. S., Garcia-Carreras, L., Lister, G. M. S., Parker, D. J., Knippertz, P., and
1681 Birch, C. E.: The role of moist convection in the West African monsoon system: Insights from
1682 continental-scale convection-permitting simulations, Geophys Res Lett, 40, 1843-1849,
1683 10.1002/Grl.50347, 2013a.

1684 Marsham, J. H., Hobby, M., Allen, C., J, B., Bart, M., Brooks, B., Cavazos-Guerra, C., Engelstaedter,
1685 S., Gascoyne, M., McQuaid, J., O'Learly, A., Ouchene, B., Ouladichir, A., Parker, D., Saci, A., Salah-
1686 Ferroudj, M., Todd, M., and Washington, R.: Meteorology and dust in the central Sahara:
1687 Observations from Fennec superiste-1 during the June 2011 Intensive Observation Period, accepted
1688 for publication in Journal of Geophysical Research-Atmospheres, 2013b.

1689 Marsham, J. H., Hobby, M., Allen, C. J. T., Banks, J. R., Bart, M., Brooks, B. J., Cavazos-Guerra, C.,
1690 Engelstaedter, S., Gascoyne, M., Lima, A. R., Martins, J. V., McQuaid, J. B., O'Leary, A., Ouchene, B.,
1691 Ouladichir, A., Parker, D. J., Saci, A., Salah-Ferroudj, M., Todd, M. C., and Washington, R.:

Meteorology and dust in the central Sahara: Observations from Fennec supersite-1 during the June 2011 Intensive Observation Period, J Geophys Res-Atmos, 118, 4069-4089, Doi 10.1002/Jgrd.50211, 2013c.

McConnell, C. L., Highwood, E. J., Coe, H., Formenti, P., Anderson, B., Osborne, S., Nava, S., Desboeufs, K., Chen, G., and Harrison, M. A. J.: Seasonal variations of the physical and optical characteristics of Saharan dust: Results from the Dust Outflow and Deposition to the Ocean (DODO) experiment, J Geophys Res-Atmos, 113, Doi 10.1029/2007jd009606, 2008.

Messager, C., Parker, D. J., Reitebuch, O., Agusti-Panareda, A., Taylor, C. M., and Cuesta, J.: Structure and dynamics of the Saharan atmospheric boundary layer during the West African monsoon onset: observations and analyses from the research flights of 14 and 17 July 2006, Q J Roy Meteor Soc, 136, 107-124, doi:10.1002/qj.469, 2010.

Müller, D., Ansmann, A., Freudenthaler, V., Kandler, K., Toledano, C., Hiebsch, A., Gasteiger, J., Esselborn, M., Tesche, M., Heese, B., Althausen, D., Weinzierl, B., Petzold, A., and von Hoyningen-Huene, W.: Mineral dust observed with AERONET Sun photometer, Raman lidar, and in situ instruments during SAMUM 2006: Shape-dependent particle properties, J Geophys Res-Atmos, 115, Doi:10.1029/2009jd012523, 2010a.

Müller, D., Weinzierl, B., Petzold, A., Kandler, K., Ansmann, A., Müller, T., Tesche, M., Freudenthaler, V., Esselborn, M., Heese, B., Althausen, D., Schladitz, A., Otto, S., and Knippertz, P.: Mineral dust observed with AERONET Sun photometer, Raman lidar, and in situ instruments during SAMUM 2006: Shape-independent particle properties, J Geophys Res-Atmos, 115, Doi 10.1029/2009jd012520, 2010b.

Müller, D., Lee, K. H., Gasteiger, J., Tesche, M., Weinzierl, B., Kandler, K., Müller, T., Toledano, C., Otto, S., Althausen, D., and Ansmann, A.: Comparison of optical and microphysical properties of pure Saharan mineral dust observed with AERONET Sun photometer, Raman lidar, and in situ instruments during SAMUM 2006, J Geophys Res-Atmos, 117, Doi 10.1029/2011jd016825, 2012.

Nakajima, T., Tonna, G., Rao, R. Z., Boi, P., Kaufman, Y., and Holben, B.: Use of sky brightness measurements from ground for remote sensing of particulate polydispersions, Appl Optics, 35, 2672-2686, Doi 10.1364/Ao.35.002672, 1996.

Newman, S. M., Clarisse, L., Hurtmans, D., Marenco, F., Johnson, B., Turnbull, K., Havemann, S., Baran, A. J., O'Sullivan, D., and Haywood, J.: A case study of observations of volcanic ash from the Eyjafjallajokull eruption: 2. Airborne and satellite radiative measurements, J Geophys Res-Atmos, 117, 10.1029/2011jd016780, 2012.

Omar, A. H., Winker, D. M., Kittaka, C., Vaughan, M. A., Liu, Z. Y., Hu, Y. X., Trepte, C. R., Rogers, R. R., Ferrare, R. A., Lee, K. P., Kuehn, R. E., and Hostetler, C. A.: The CALIPSO Automated Aerosol Classification and Lidar Ratio Selection Algorithm, J Atmos Ocean Tech, 26, 1994-2014, Doi 10.1175/2009jtecha1231.1, 2009.

Osborne, S. R., Baran, A. J., Johnson, B. T., Haywood, J. M., Hesse, E., and Newman, S.: Short-wave and long-wave radiative properties of Saharan dust aerosol, Q J Roy Meteor Soc, 137, 1149-1167, Doi 10.1002/Qj.771, 2011.

Paluch, I. R.: Entrainment Mechanism in Colorado Cumuli, J Atmos Sci, 36, 2467-2478, Doi 10.1175/1520-0469(1979)036<2467:Temicc>2.0.Co;2, 1979.

1733 Pappas, V., Ryder, C. L., Highwood, E. J., and Young, S.: Comparison of Fennec airborne in-situ
1734 dust measurements with CALIOP spaceborne lidar retrievals of extinction, Remote Sensing of
1735 Environment, in prep.

1736 Petersen, G. N., and Renfrew, I. A.: Aircraft-based observations of air-sea fluxes over Denmark
1737 Strait and the Irminger Sea during high wind speed conditions, Q J Roy Meteor Soc, 135, 2030-2045,
1738 Doi 10.1002/Qj.355, 2009.

1739 Preissler, J., Wagner, F., Pereira, S. N., and Guerrero-Rascado, J. L.: Multi-instrumental
1740 observation of an exceptionally strong Saharan dust outbreak over Portugal, J Geophys Res-Atmos,
1741 116, Doi:10.1029/2011jd016527, 2011.

1742 Raymond, D. J., and Blyth, A. M.: Precipitation Development in a New-Mexico Thunderstorm, Q J
1743 Roy Meteor Soc, 115, 1397-1423, DOI 10.1002/qj.49711549011, 1989.

1744 Redelsperger, J. L., Thorncroft, C. D., Diedhiou, A., Lebel, T., Parker, D. J., and Polcher, J.: African
1745 monsoon multidisciplinary analysis - An international research project and field campaign, B Am
1746 Meteorol Soc, 87, 1739-1746, Doi 10.1175/Bams-87-12-1739, 2006.

1747 Reid, J. S., Jonsson, H. H., Maring, H. B., Smirnov, A., Savoie, D. L., Cliff, S. S., Reid, E. A., Livingston,
1748 J. M., Meier, M. M., Dubovik, O., and Tsay, S. C.: Comparison of size and morphological
1749 measurements of coarse mode dust particles from Africa, J Geophys Res-Atmos, 108, Doi
1750 10.1029/2002jd002485, 2003.

1751 Reid, J. S., Brooks, B., Crahan, K. K., Hegg, D. A., Eck, T. F., O'Neill, N., de Leeuw, G., Reid, E. A., and
1752 Anderson, K. D.: Reconciliation of coarse mode sea-salt aerosol particle size measurements and
1753 parameterizations at a subtropical ocean receptor site, J Geophys Res-Atmos, 111,
1754 10.1029/2005jd006200, 2006.

1755 Reid, J. S., Reid, E. A., Walker, A., Piketh, S., Cliff, S., Al Mandoos, A., Tsay, S. C., and Eck, T. F.:
1756 Dynamics of southwest Asian dust particle size characteristics with implications for global dust
1757 research, J Geophys Res-Atmos, 113, Doi 10.1029/2007jd009752, 2008.

1758 Renfrew, I. A., Petersen, Outten, Sproson, Moore, Hay, Ohigashi, Zhang, Kristjansson, Fore,
1759 Olafsson, Gray, Irvine, Bovis, Brown, Swinbank, Haine, Lawrence, Pickart, Shapiro, and Woolley: The
1760 Greenland flow distortion experiment, B Am Meteorol Soc, 89, 1307-1324, Doi
1761 10.1175/2008bams2508.1, 2008.

1762 Roberts, G. C., and Nenes, A.: A continuous-flow streamwise thermal-gradient CCN chamber for
1763 atmospheric measurements, Aerosol Sci Tech, 39, 206-221, Doi 10.1080/027868290913988, 2005.

1764 Rodwell, M. J., and Jung, T.: Understanding the local and global impacts of model physics
1765 changes: An aerosol example, Q J Roy Meteor Soc, 134, 1479-1497, Doi 10.1002/Qj.298, 2008.

1766 Rose, D., Gunthe, S. S., Mikhailov, E., Frank, G. P., Dusek, U., Andreae, M. O., and Poschl, U.:
1767 Calibration and measurement uncertainties of a continuous-flow cloud condensation nuclei counter
1768 (DMT-CCNC): CCN activation of ammonium sulfate and sodium chloride aerosol particles in theory
1769 and experiment, Atmos Chem Phys, 8, 1153-1179, 2008.

1770 Rosenberg, P., Dean, A., Williams, P., Minikin, A., Pickering, M., and Petzold, A.: Particle sizing
1771 calibration with refractive index correction for light scattering optical particle counters and impacts
1772 upon PCASP and CDP data collected during the Fennec campaign, Atmospheric Measurement
1773 Technique Discussions, 5, 97-135, doi:10.5194/amtd-5-97-2012, 2012.

Rosenberg, P. D., Parker, D. J., Ryder, C. L., Marsham, J. H., Garcia-Carreras, L., Dorsey, J. R., Brooks, I. M., Dean, A. R., Crosier, J., McQuaid, J. B., and Washington, R.: Quantifying particle size and turbulent scale dependence of dust flux in the Sahara using aircraft measurements, J Geophys Res-Atmos, 119, 7577-7598, Doi 10.1002/2013jd021255, 2014.

Ryder, C. L., Highwood, E. J., Lai, T. M., Sodemann, H., and Marsham, J. H.: Impact of Atmospheric Transport on the Evolution of Microphysical and Optical Properties of Saharan Dust, accepted at Geophysical Research Letters, 2013a.

Ryder, C. L., Highwood, E. J., Rosenberg, P., Trembath, J., Brooke, J., Bart, M., Dean, A., Crosier, J., Dorsey, J., Brindley, H., Banks, J. R., Marsham, J. H., McQuaid, J. B., Sodemann, H., and Washington, R.: Optical properties of Saharan dust aerosol and contribution from teh coarse mode as measured during the Fennec 2011 aircraft campaign, Atmos. Chem. Phys., 13, 303-325, doi:10.5194/acp-13-303-2013, 2013b.

Sassen, K., DeMott, P. J., Prospero, J. M., and Poellot, M. R.: Saharan dust storms and indirect aerosol effects on clouds: CRYSTAL-FACE results, Geophys Res Lett, 30, Doi 10.1029/2003gl017371, 2003.

Schepanski, K., Tegen, I., Laurent, B., Heinold, B., and Macke, A.: A new Saharan dust source activation frequency map derived from MSG-SEVIRI IR-channels, Geophys Res Lett, 34, Doi 10.1029/2007gl030168, 2007.

Schepanski, K., Tegen, I., and Macke, A.: Saharan dust transport and deposition towards the tropical northern Atlantic, Atmos Chem Phys, 9, 1173-1189, 2009.

Schepanski, K., Flamant, C., Chaboureau, J. P., Kocha, C., Banks, J. R., Brindley, H. E., Lavaysse, C., Marnas, F., Pelon, J., and Tulet, P.: Characterization of dust emission from alluvial sources using aircraft observations and high-resolution modeling, J Geophys Res-Atmos, 118, 7237-7259, Doi 10.1002/Jgrd.50538, 2013.

Scheuvens, D., Schutz, L., Kandler, K., Ebert, M., and Weinbruch, S.: Bulk composition of northern African dust and its source sediments - A compilation, Earth-Sci Rev, 116, 170-194, DOI 10.1016/j.earscirev.2012.08.005, 2013.

Schuster, G. L., Vaughan, M., MacDonnell, D., Su, W., Winker, D., Dubovik, O., Lapyonok, T., and Trepte, C.: Comparison of CALIPSO aerosol optical depth retrievals to AERONET measurements, and a climatology for the lidar ratio of dust, Atmos Chem Phys, 12, 7431-7452, DOI 10.5194/acp-12-7431-2012, 2012.

Sodemann, H., Lai, M., Marenco, F., Ryder, C. L., Flamant, C., Knippertz, P., Rosenberg, P., Bart, M., and McQuaid, J.: Lagrangian dust model simulations for a case of moist convective dust emission and transport in the western Sahara region during Fennec/LADUNEX, J Geophys Res-Atmos, 2015, accepted for publication.

Sternberg, R.: Into the Cauldron: A Meteorological Adventure, http://fennec.ouce.ox.ac.uk/movie.html, in: EGU GeoCinema, 2013.

Stohl, A., Forster, C., Frank, A., Seibert, P., and Wotawa, G.: Technical note: The Lagrangian particle dispersion model FLEXPART version 6.2, Atmos Chem Phys, 5, 2461-2474, 2005.

Sultan, B., and Janicot, S.: The West African monsoon dynamics. Part II: The "preonset" and "onset" of the summer monsoon, J Climate, 16, 3407-3427, Doi 10.1175/1520-0442(2003)016<3407:Twamdp>2.0.Co;2, 2003.

Sun, D. L., Lau, W. K. M., Kafatos, M., Boybeyi, Z., Leptoukh, G., Yang, C. W., and Yang, R. X.: Numerical Simulations of the Impacts of the Saharan Air Layer on Atlantic Tropical Cyclone Development, J Climate, 22, 6230-6250, Doi 10.1175/2009jcli2738.1, 2009.

Tesche, M., Ansmann, A., Muller, D., Althausen, D., Mattis, I., Heese, B., Freudenthaler, V., Wiegner, M., Esselborn, M., Pisani, G., and Knippertz, P.: Vertical profiling of Saharan dust with Raman lidars and airborne HSRL in southern Morocco during SAMUM, Tellus B, 61, 144-164, DOI 10.1111/j.1600-0889.2008.00390.x, 2009.

Todd, M. C., Allen, C. J. T., Bart, M., Bechir, M., Bentefouet, J., Brooks, B. J., Cavazos-Guerra, C., Clovis, T., Deyane, S., Dieh, M., Engelstaedter, S., Flamant, C., Garcia-Carreras, L., Gandega, A., Gascoyne, M., Hobby, M., Kocha, C., Lavaysse, C., Marsham, J. H., Martins, J. V., McQuaid, J. B., Ngamini, J. B., Parker, D. J., Podvin, T., Rocha-Lima, A., Traore, S., Wang, Y., and Washington, R.: Meteorological and dust aerosol conditions over the western Saharan region observed at Fennec Supersite-2 during the intensive observation period in June 2011, J Geophys Res-Atmos, 118, 8426-8447, Doi 10.1002/Jgrd.50470, 2013.

Tompkins, A. M., Cardinali, C., Morcrette, J. J., and Rodwell, M.: Influence of aerosol climatology on forecasts of the African Easterly Jet, Geophys Res Lett, 32, Doi:10.1029/2004gl022189, 2005.

Trembath, J.: Airborne CCN Measurements, SAES, University of Manchester, 2012.

Trembath, J., Bart, M., and Brooke, J.: FAAM Technical Note: Efficiencies of modified Rosemount housings for sampling aerosol on a fast atmospheric research aircraft, Facility for Airborne Atmospheric Measurements, FAAM, Cranfield, UK, http://www.faam.ac.uk/index.php/component/docman/cat_view/140-science-instruments, 2012.

Tulet, P., Crahan-Kaku, K., Leriche, M., Aouizerats, B., and Crumeyrolle, S.: Mixing of dust aerosols into a mesoscale convective system Generation, filtering and possible feedbacks on ice anvils, Atmos Res, 96, 302-314, DOI 10.1016/j.atmosres.2009.09.011, 2010.

Turnbull, K., Johnson, B., Marenco, F., Haywood, J. M., Minikin, A., Weinzierl, B., Schlager, H., Schumann, U., Leadbetter, S., and Woolley, A.: A case study of observations of volcanic ash from the Eyjafjallajokull eruption: 1. In situ airborne observations, J Geophys Res-Atmos, 117, 10.1029/2011jd016688, 2012.

Twohy, C. H., Kreidenweis, S. M., Eidhammer, T., Browell, E. V., Heymsfield, A. J., Bansemer, A. R., Anderson, B. E., Chen, G., Ismail, S., DeMott, P. J., and Van den Heever, S. C.: Saharan dust particles nucleate droplets in eastern Atlantic clouds, Geophys Res Lett, 36, Doi 10.1029/2008gl035846, 2009.

Veihelmann, B., Konert, M., and van der Zande, W. J.: Size distribution of mineral aerosol: using light-scattering models in laser particle sizing, Appl Optics, 45, 6022-6029, Doi 10.1364/Ao.45.006022, 2006.

Washington, R., Todd, M. C., Engelstaedter, S., Mbainayel, S., and Mitchell, F.: Dust and the low-level circulation over the Bodele Depression, Chad: Observations from BoDEx 2005, J Geophys Res-Atmos, 111, 10.1029/2005jd006502, 2006.

1853 Washington, R., Flamant, C., Parker, D. J., Marsham, J. H., McQuaid, J. B., Brindley, H., Todd, M.,
1854 Highwood, E. J., Ryder, C. L., Chaboureau, J.-P., Kocha, C., Bechir, M., and Saci, A.: Fennec - The
1855 Saharan Climate System, CLIVAR Exchanges, 17, 31-32, 2012.

1856

1857

1858 ## Tables

Campaign	Date	Reference
JET2000	Summer 2000	Thorncroft et al., 2003
Saharan Dust Experiment (SHADE)	Summer 2000	Haywood et al., 2003
Dust and Biomass Experiment DABEX	Winter 2006	Haywood et al., 2008
Dust Outflow and Deposition to the Ocean (DODO)	Winter/Summer 2006	McConnell et al., 2008
African Monsoon Multidisciplinary Analysis (AMMA)	2006	Redelsperger et al., 2006
NASA AMMA (NAMMA)	Summer 2006	Zipser et al., 2009
Saharan Mineral Dust Experiment 1 (SAMUM1)	2006	Heintzenberg, 2009
Saharan Mineral Dust Experiment 2 (SAMUM2)	2008	Ansmann et al. (2011)
Geostationary Earth Radiation Budget Intercomparison of Long-wave and Short-wave radiation (GERBILS)	Summer 2007	Haywood et al., 2011

1859 **Table 1: Previous aircraft programmes in the region.**

1860

IOP	Date	Operating base	Aircraft	Number of Flights	Number of Dropsondes
Pilot study	April 2011	Ouarzazate, Morocco	BAe146	6	42
IOP1	June 2011	Fuerteventura, Canaries	BAe146 FF-20	16 (BAe146) 18 (FF-20)	81 (BAe146) 136 (FF-20)
IOP2	June 2012	Fuerteventura, Canaries	BAe146	14	40

Table 2: Overview of IOPs

1864

Name	**Instrument**	**Measures**	**Sampling rate**	Reference for more detail
LNG LIDAR	Downward facing high spectral resolution LIDAR (CAB)	Atmospheric backscatter coefficients at 532 and 1064 nm. Aerosol extinction coefficients at 532 nm.	20 Hz	Banks et al., 2013; Schepanski et al., 2013
AVAPS II	Airborne Vertical Atmospheric Profiler System & RD94 GPS dropsondes (CAB)	Profiles of position, pressure, temperature, relative humidity, wind speed and direction	2 Hz	
Basler SCA1400-30FM	Downward facing monochrome (black/white) camera (CAB)	Pictures of ground surface with a resolution of 1392 x 1040 pixels. Each photograph covers a horizontal area of 3.3 km x 4.4 km along the track for a nominal aircraft altitude of 11 km asl	1 Hz	Schepanski et al., 2013
Kipp & Zonen CPM22	Precision Spectral Pyranometer (RFM & BLM)	0.2–3.6 µm up- and downwelling irradiance	0.2 Hz	
Kipp & Zonen CGR4	Precision Infrared Radiometer (RFM & BLM)	4.5–42 µm up- and downwelling irradiance	0.05 Hz	
CLIMAT CE 332	Downward-facing radiometer (BLM)	Spectrally resolved directional radiance: brightness temperature at 8.7, 10.8 and 12 µm	1 Hz	Legrand et al., 2000
General Eastern 1011B (RDM)	Hygrometer using the chilled-mirror technique (RDM)	Water vapour (dew point temperature) over range -65 to 50°C	1 Hz	
Aerodata Humicap (RDM)	Humidity capacity sensor (RDM)	Relative humidity (0-100%)	10 Hz	
Rosemount 1201	Pressure sensor (NBM)	Static pressure (250-1035 hPa)	10 Hz	
Rosemount 1221	Pressure sensors (NBM)	Differential incidence and drift pressures (±70 hPa)	10 Hz	
Rosemount 102 E2AL	Temperature sensor (RDM)	Temperatures (non de-iced), calibrated over range –60° to 40°C; uncertainty ±0.5°C	10 Hz	
Rosemount 871	Ice Proble (RDM)	Indication of supercooled water	N/A	
LITTON 90-100	Inertial navigation unit (CAB)	Aircraft position, aircraft velocity components, aircraft attitude (pitch, roll, yaw) and attitude rates, ground speed, wind speed and direction, and drift angle (position and acceleration at 1 Hz)	66 Hz	
TRT AHV 8	Radar altimeter (CAB)	Altitude (0-5000 ft, accuracy ±2%)	10 Hz	
Bancom BC635 on Trimble Transducer	Global Positioning System (CAB)	Aircraft position, velocity, and time standard	1 Hz	
Collins ADC 80	Air Data Computer (CAB)	Barometric altitude (-2000 to 7000 ft) and true air speed	10 Hz	

1865 **Table 3: Instruments onboard the SAFIRE Falcon 20 during the 2011 IOP. NBM= Nose Boom Mounted; CAB=inside aircraft**
1866 **cabin, RDM=Radome Mounted, BLM=Belly Mounted; RFM=Roof Mounted**

1867

Name	Instrument	Property Measured	Sampling rate	Reference	IOP in Use
Aircraft Position and Meteorological Measurements					
GPS	Patch	Aircraft position, velocity, and time standard	1 Hz	FAAM	All
INU	Inertial Navigation Unit	Aircraft velocity components, attitude, attitude rates, ground speed, and drift angle	32 Hz	FAAM	All
RadAlt	Radar Altimeter	Altitude above surface, max 5000 ft AGL (accuracy ±2%)	2 Hz	FAAM	All
RVSM	Reduced vertical separation minimum data system	Static and pitot-static pressures, pressure altitude, indicated air speed	32 Hz	FAAM	All
Rosemount Temperature Sensors		Deiced and non-deiced, calibrated over range –60° to 30°C; (±0.3°C)	32 Hz	FAAM	All
Turbulence probe	Turbulence (see also RVSM)	Air speed and incidence angle; 3-D wind components; measurement uncertainty ±0.2 m s–1	32 Hz	Peterson & Renfrew, 2008	All
AIMMS	Aircraft-Integrated Meteorological Measurement System (Aventech Research, Inc)	General meteorological parameters, generally used as backup to core turbulence probe. WM		FAAM	All
AVAPS	Airborne Vertical Atmospheric Profiler System (Vaisala RD94 GPS dropsondes)	Profiles of position, pressure, temperature, relative humidity, wind speed and direction	2 Hz	FAAM	All
Water Content Measurements					
TWC	Total water content using a Lyman-alpha absorption hygrometer	Water (H_2O) over range 0–20 g kg^{-1} and accuracy ±0.15 g kg^{-1}	64 Hz	FAAM	All
General Eastern	Hygrometer (using the chilled-mirror technique)	Water vapor (dewpoint temperature) over 220–320K; instrument response time can be up to 30 s; measurement uncertainty ±0.25K above 273.15 K, ±1K at 210 K	4 Hz	FAAM	All
Johnson Williams	Liquid water content probe	Liquid water concentration in clouds using heated wire resistance bridge over 0–3 gm^{-3}; uncertainity ±10%	4 Hz	FAAM	All
Nevzorov	Liquid and total water content probe	Liquid and total (ice plus liquid) water in clouds using a heated wire over range 0.003–3 gm^{-1}; accuracy ±10%	8 Hz	FAAM	All
Aircraft Inlets					
Rosemount 102E Inlets	Aerosol inlets for cabin instrumentation	Originally designed for PRT Measurements, only accumulation mode particles passed	n/a	Trembath (2012)	All

LTI	Low Turbulence Inlet	Fully characterised inlet, passes coarse mode particles	n/a	Trembath 2012, Wilson et al., 2004	All
Filter sample inlet	Parallel coarse mode samplers	Supplies filter samples for offline analysis	n/a	Formenti et al, 2014	All
In-situ Aerosol Measurements					
PCASP	Passive Cavity Aerosol Spectrometer Probe (PMS canister instrument)	PNC, 0.1–3 μm, OPT, (WM	1 Hz	Rosenberg et al., 2012, FAAM	All
CDP	Cloud Droplet Probe	PNC, 3-50 μm, OPT (WM)	1Hz standard, 10Hz during Fennec	Rosenberg et al., 2012, FAAM	All
CIP15	Cloud Imaging Probe	PNC, 15-930 μm, 15 μm resolution, SH (WM). Provided by U.Manchester in 2011 and by FAAM in 2012. 2012 data suffered from electronic noise.	10Hz	Rosenberg et al., 2012, FAAM	All
CIP100	Cloud Imaging Probe	PNC, 100-6200 μm, 100 μm resolution, SH (WM)	1Hz	FAAM	2012
GRIMM OPC	Grimm Technik 1.129 Sky Optical Particle Counter	PNC, 0.25-32 μm, placed behind different inlets,OPT (CAB)	1Hz	Heim et al., 2008	All
2D-C	Two-dimensional cloud particle imaging probe (PMS canister instrument)	5-s-averaged values of PNC, condensed water content, mean volume radius, precipitation rate, and size spectrum (25–800 μm), SH (WM)	1 Hz	FAAM	2012
SID2H	Small Ice Detector	PNC, 2-60 μm, OPT, also non-sphericity (WM)	1Hz	Cotton et al., 2010	All
CAS	Cloud and Aerosol Spectrometer	PNC, 0.6 – 50 μmOPT, (WM), part of U.Manchester CAPS probe.	1Hz	(Baumgardner et al., 2001)	2011
University of Manchester CAPS Probe	Cloud, Aerosol and Precipitation Spectrometer (DMT)	Aerosol particle and cloud hydrometeor size (0.51 - 50 μm). Liquid water content from 0.01 to 3 g m^{-3} . Aerosol probes comprise CAS and CIP15 instruments (WM)	1Hz	FAAM	2011
CCN	Dual column continuous flow cloud condensation nuclei counter (DMT)	Concentration and properties of cloud condensation nuclei (CAB)	1 Hz	Trembath (2012)	All
CPC	Modified TSI 3786 condensation particle counter	Aerosol particles (2.5 nm – 3 μm) (CAB)	1 Hz	Trembath (2012)	All
Nephelometer	TSI 3563 Integrating nephelometer	Total scattering and hemispheric backscattering coefficient at 450, 550, and 700 nm (CAB)	1 Hz	Ryder et al., (2013b), FAAM	All
PSAP	Radiance Research Particle Soot Absorption Photometer	Absorption coefficient at 567 nm (CAB)	1 Hz	Ryder et al., (2013b), FAAM	All
Radiometric Measurements					

BBR	Broadband shortwave Radiometers (pyranometers)	0.3–3 μm & 0.7–3 μm up and downwelling irradiance	1 Hz	FAAM	All
SHIMS	Spectral Hemispheric Irradiance MeasurementS	Spectrally resolved irradiance, up and downwelling, 0.3-1.7 μm	0.1Hz	Osborne et al., 2011	All
SWS	ShortWave Spectrometer	Spectrally resolved directional radiance, 0.3-1.7 μm	0.1Hz	Osborne et al., 2011	All
ARIES	Airborne Research Interferometer Evaluation System	Spectrally resolved directional radiance, 3.3-18 μm	1Hz	Wilson et al., 1999; Osborne et al., 2011	All
Heimann	Downward-facing radiometer	Downward facing brightness temperature (8–14 μm)	4 Hz	FAAM	All
LIDAR	Downward facing aerosol LIDAR (Leosphere ALS450)	Aerosol and thin cloud retreivals, qualitative depolarisation	2 sec	Marenco et al., (2011; 2013)	All
Video cameras	Up/downward, forward, and rear-view cameras	Digital video recordings		FAAM	All
Chemistry Measurements					
Ozone	TECO 49C UV photometric instrument	Ozone (O_3); integration time 4 s	1 Hz	FAAM	All
Carbon Monoxide	CO Aerolaser AL5002	Carbon monoxide (CO) by UV flourescence at 150 nm	1 Hz	FAAM	2012

Table 4: Instrumentation on the BAe146 aircraft relevant to Fennec. WM=Wing Mounted, CAB=inside aircraft cabin, PNC=particle number concentration, OPT=optical scattering measurements, SH=Light Shadowing Measurements. Size ranges shown for optical instruments refer to nominal ranges provided by manufacturers, i.e. not corrected for aerosol type-specific refractive indices. FAAM = refer to FAAM website where full instrumentation details are provided, www.faam.ac.uk/index.ph./science-instruments.

1875

Date	Flight Number	Times, UTC	Locations	Purpose
4 April	b589	1551 to 1852	MAU	Overflight of dust front
5 April	b590	0850 to 1328	MAU	Sampling of maritime air underlying dusty continental air
	b591	1505 to 1838	MAU	Sampling of maritime air underlying dusty continental air
7 April	b592 (2 flights)	0652 to 1706	MAU	Sampling of dust in recovering SABL
8 April	b593	0829 to 1341	MAU	Surface albedo impact on recovering SABL
9 April	b594	0913 to 1359	Ouarzazate to UK	Sampling of dust transported northwards towards UK

1876 **Table 5: April 2011 pilot campaign flights of BAe146.**

1877

Date	Flight Number	Times, UTC	Locations	Purpose
2 June	F09	1527-1858	EAO	Dust outflow over EAO
6 June	F10	1200-1533	EAO	Dust outflow over EAO
10 June	F11	1028-1401	EAO, MAU, SEN	Dust outflow over EAO & PBL over MAU
10 June	F12	161-1940	EAO, MAU, SEN	Dust outflow over EAO & PBL over MAU
11 June	F13	0906-229	N MAU	Dust uplift, RAIN4DUST
11 June	F14	14401-809	N MAU	PBL
13 June	F15	1100-1422	N MAU and N MAL	Survey of N MAU & dust associated with Mediterranean surge
14 June	F16	1437-1809	N MAU	PBL
15 June	F17	1433-1802	N MAU	PBL
16 June	F18	0913-1224	N MAU	Dust uplift, RAIN4DUST
16 June	F19	1442-1812	N MAU	PBL; approaching AEW
17 June	b600	0748-1241	MAL, N MAU	Characterisation of LLJ winds and dust
	F20	1528-1858	N MAL, N MAU	Survey of N MAU and N MAL & dust associated with Mediterranean surge and AEW
	b601	1443-1937	N MAL, N MAU	Characterisation of LLJ winds and dust
18 June	b602	0810-1240	N MAL, N MAU	Characterisation of LLJ winds and dust
	b603	1415-1555	Canary Islands	High altitude radiation instrument calibration
20 June	b604	1247-1751	MAU	Sampling of dust uplifted by MCS, LADUNEX
	F21	1322-1700	N and central MAU	Survey of dust associated with ITD and SHL
21 June	b605	0810-1158	MAU	Sampling of dust uplifted by Atlas Mts density current
	b606	1404-1920	MAU	SABL development and heat fluxes
	F22	0718-1035	N MAU and N MAL	Survey of dust associated with Mediterranean surge and density currents from Atlas Mts
	F23	1313-1630	N MAU and N MAL	Survey of dust associated with Mediterranean surge and density currents from Atlas Mts
22 June	b607	0804-1237	MAU, MAL	Sampling of SHL with LIDAR and dropsondes
	b608	1510-2016	MAU, MAL	Sampling of SHL with LIDAR and dropsondes
	F24	0917-1245	N MAU	Survey SHL; dust associated with Mediterranean surge (N) & ITD (S & E)
	F25	1521-1849	N MAU	Survey of SHL; dust associated with Mediterranean surge (N) & ITD (S & E)
23 June	F26	0833-1200	N MAU	Dust uplift, RAIN4DUST
24 June	b609	1129-1645	MAU	Dust-cloud interactions
25 June	b610	0731-1217	MAU	Dust uplift by LLJ
	b611	1414-1916	MAU	Overflight of Zouerate ground site
26 June	b612	0729-1222	MAU	Dust and radiative fluxes
	b613	1355-1859	MAU	SABL development and heat fluxes
27 June	b614	0634-1139	MAU	Dust uplift by LLJ
28 June	b615	0814-1129	Canary Islands	Radiation instrument calibration

Table 6: June 2011 IoP Flights. Flight numbers with preceding 'b' indicate BAe146 flight, with preceding 'F' indicate Falcon flight. Abbreviations: EAO=Eastern Atlantic Ocean, MAU=Mauritania, MAL=Mali, SEN=Senegal, FUE=Fuerteventura, ZOU=Zouerate supersite.

1882

Date	Flight Number	Times, UTC	Locations	Purpose
1 June	b698	0942 - 1708	UK to FUE	Science transit to FUE with radiation cailbrations
6 June	b699	1201 - 1654	N MAL, N MAU	Atlantic Inflow 1
8 June	b700	0756 - 1257	N MAL, N MAU	Atlantic Inflow 2
9 June	b701	0755 - 1308	Central MAU	Dust at ITD 1
10 June	b702	0804 - 1241	Central MAU	Dust at ITD 2 (to Dakar)
	b703	1412 - 1720	EAO	Dust Outflow over EAO
11 June	b704	1214 - 1719	S MAU	Very heavy dust at ITD 3
12 June	b705	1127 - 1707	N MAL	Midday Heat fluxes
14 June	b706	1307 - 1813	N MAL	Dust uplift 1
15 June	b707	0913 - 1433	N MAL	Dust uplift 2
16 June	b708	0756 - 1308	N MAL, W MAU	Dust uplift by LLJ and Radiative Closure
17 June	b709	1214 - 1724	N MAL	Dust in SABL and Radiative Closure
18 June	b710	0751 to 1311	ZOU	SAVEX flight over Zouerate
19 June	b711	0755 to 1039	FUE and EAO	Science transit to Porto

1883 **Table 7: June 2012 Fennec IOP flights.**

1884

1885

Research Area	Key Findings	Reference
Publications Deriving from Fennec Aircraft Observations		
Size distribution measurements	A new method for correcting OPC data for particle optical properties	Rosenberg et al. (2012)
BAe146 Inlets	BAe146 Rosemount inlet significantly excludes particles larger than 3 µm diameter	Trembath (2012)
Size distributions and optical properties of dust	Consistent presence of coarse and giant particles over Sahara; SSA at 550 nm 0.7 to 0.97 strongly related to particle size; inverse relationship between size and dust age.	Ryder et al., (2013b)
Impacts of transport on dust size distribution	d_{eff} decrease of 4.5 µm, and SSA increase from 0.92 to 0.95 between fresh and Atlantic SAL dust.	Ryder et al., (2013a)
Dust-ozone interactions	Increased dust surface area associated with fresh dust uplift and a large coarse mode act as a route for the reduced ozone concentrations.	Brooke (2014)
Dust fluxes	Size resolved dust fluxes follow the power law predicted by the Kok brittle fragmentation theory. Large size cut off is significantly larger than seen in other observations. Large fluxes were correlated with regions of varying topography.	Rosenberg et al. (2014)
Satellite retrievals of dust	Imperial SEVIRI dust AOD products are most effective at high dust loadings, but are sensitive to meteorological conditions; MODIS Deep Blue and MISR AOD products more consistent at lower dust loadings.	Banks et al. (2013)
Lagrangian modelling of dust uplift and transport	Validation of Lagrangian dust transport model with dust mass concentration underlines difficulties to quantify dust emission due to moist convection. Manual inversion approach constrains dust source and flux.	(Sodemann et al., 2015, accepted for publication)
Dust uplift from fluvial sources	Dust emission from alluvial source observed by airborne remote sensing; Nocturnal LLJ drives morning dust uplift; explicit representation of endorheic systems as dust sources required in terms of their role as dust sources.	Schepanski et al.,(2013)
Structure and diurnal growth of the SABL	Turbulent structure, vertical fluxes and diurnal growth of SABL described with radiosondes, aircraft measurements and a LEM. Novel processes found, such as detrainment from the CBL top which acts to slow down CBL growth.	Garcia-Carreras et al. (2015)
Moisture transport pathways in the SHL region	Observation-based SHL characterisation; monsoon surge splits into two moisture transport pathways: a) around the SHL and b) towards northeast; afternoon CBL depth over-estimation by model leads to moisture advection error.	Engelstaedter et al. (2015)
Further information from Fennec		
Introduction to Fennec		Washington et al. (2012)
Ground-based observations	Supersite 1, Bordj Badji Moktar	Marsham et al., (2013)
	Supersite 2, Zouerate	Todd et al. (2013)

	The Fennec Automatic Weather Station Network	Hobby et al. (2013)

Table 8: Key publications deriving from Fennec aircraft observations and summarizing other Fennec ground-based observations.

Figure Captions

Figure 1: The Fennec domain and climatology. Figure shows mean (2000–2012) June–September AOD from satellite MISR data (shaded, contour intervals are 0.4, 0.6, and 0.8) and key mean June–September circulation features derived from ERA-Interim reanalysis data (1979–2012), specifically the mean position of the Saharan heat low core (1008 hPa contour of sea level pressure, thick red contour); the mean position of the inter-tropical discontinuity (solid blue line, as defined by the 10 gkg^{-1} contour of 925 hPa specific humidity). Figure also highlights the location of the two Fennec supersites (SS1 yellow square, SS2 yellow circle), and approximate aircraft flight zone (green polygon). Also indicated are surface elevation (dashed cyan contour, 1000, 1500, and 2000m) and the approximate location of recent airborne field campaigns.

Figure 2: Flight tracks of the BAe146 and Falcon during Fennec: (a) Fennec Pilot, April 2011, BAe146; (b) June 2011, Falcon, (c) June 2011, BAe146, (d) June 2011, BAe146. Each colour shows a different flight. Note that in (b) and (d), the tracks of the following flights are the same and therefore not visible: F11, F12 and F26; F13 and F18; F14, F16, F17 and F19; F22 and F23; F24 and F25; b706 and b707.

Figure 3: Synoptic conditions during the Fennec flight campaigns. (a) 300hpa (m, shaded), 925hPa geopotential height (white contours with intervals at 700, 725, 750 and 800m), 925 hPa winds (ms^{-1}) and 15°C contour of 925 hPa temperature (blue line) to show cold air advection, on 06UTC 4th April 2011. Feature A marks the position of the cut-off low. (b) Daily mean 200hPa geopotential height (m, shaded), 925hPa winds (ms-1) and mean frequency of the SHL occurrence (white contours with intervals at 0.25, 0.5 and 0.75, as defined using the method of Lavaysse et al., [2009]) averaged over the period 1-12th June 2011 (the maritime phase). Features A, B and C indicate the approximate locations of an upper level trough, SHL centre and maritime low level flow, respectively. (c) as (b) except for the period 13-30th June 2011 (heat low phase) and where features A, B and C indicate the approximate locations of an upper level ridge, SHL centre and enhanced northeasterly 'Harmattan' level flow, respectively. (d) as (b) except for the period 1st-18th June 2012, and a 10.0 gkg-1 925hPa specific humidity contour (blue line) and where features A, B, C and D indicate the approximate locations of an upper level trough, SHL extension trough, maritime low level flow and ITD bulge, respectively.

Figure 4: Example size distributions measured in different dust layers during Fennec 2011. Size distributions were measured using the PCASP (green), CDP (red) and CIP15 (purple). Solid lines show measurements from b600, during active uplift close to the desert surface; dashed lines show measurements from b612 which was dust aged by several days and well-mixed within a deep SABL. Vertical error bars show one standard deviation of the data combined with instrumental uncertainty, and only upwards errors are shown for clarity. Horizontal errors show uncertainty in bin centre diameter.

Figure 5: (a) Scatter plot of the elemental Fe/Ca versus the Si/Al ratios for the Fennec 2011 and 2012 samples compared to samples collected during the AMMA, DODO and GERBILS campaign (Formenti et al., 2014). Indications of the source regions according to the values of those tracers are also given. (b) Box plot of SSAs at 550nm measured during Fennec 2011 and 2012 for horizontal runs corresponding to filter samples taken. SSAs are calculated from scattering measured by the nephelometer and absorption measured by the PSAP on the BAe146 mounted behind Rosemount inlets, and therefore represent accumulation mode only. Box lines represent the median and interquartile range, whiskers represent the minimum and maximum values, and square represents the mean.

Figure 6: Aerosol optical depths at 550 nm measured by the nephelometer and PSAP on the BAe146 during profiles, representing accumulation mode 550nm AOD. AODs are an underestimate since they do not include contribution from coarse particles. Circles represent 2011 data, diamonds 2012 data.

Figure 7: b609 dropsonde/aircraft moisture profiles and range-corrected LIDAR cross section of the scientific area of interest (red-blue colour scale, arbitrary logarithmic units) including an aircraft track coloured by the droplet concentration as measured by the CDP plus PCASP (black to red colour scale). The LIDAR data collected during descent (thick sloping black line) is plotted instead of the high level data when available. Above this, LIDAR data from the high level flight leg is shown. Arrows indicate locations of dropsondes. Sondes 1-3 were dropped on entry to the area and sonde 4 on exit.

Figure 8: Equivalent potential temperature and total water content during the flight. "Environment" points represent data from the descent out of cloud, "Boundary Layer" points represent data collected during aircraft ascent up to an altitude of 5000 m, "In cloud" points represent data collected during aircraft ascent above 5000 m where cloud droplet number was measured greater than 0.5 cm^{-1} and "Out of cloud" points represent data collected during aircraft ascent above 5000 m where cloud droplet number was less than 0.5 cm^{-1}. Mean in and out of cloud values are shown with large circles outlined in black.

Figure 9: Box and whisker diagram of mineral dust mean surface area and ozone mass mixing ratio along the b707 (15 June 2012) flight transect. Surface area is calculated from PCASP count median diameter.

Figure 10: Aircraft and satellite observations along the track of the outbound Falcon flight F23 on the 21st June (1352-1445 UT), across northern Mauritania and ending in northern Mali. Lower panel: LIDAR vertical extinction coefficient cross-section (at 532 nm); middle panel: co-located SEVIRI, MODIS, and LIDAR (LNG) AOD retrievals along the Falcon flight-track; upper panel: the along-track SEVIRI RGB 'desert-dust' imagery.

Figure 11: Volume size distributions from BAe146 flight b611 Profile 1 (1558 to 1627 UTC) compared to AERONET retrievals. Aircraft size distribution measurements are shown by green (PCASP), red (CDP) and purple (CIP15). Solid lines show the median volume concentrations over the column up to 5.5km. Vertical error bars show standard deviation over the column (where lower error bars reach below the plot minimum they have been omitted for clarity). Horizontal error bars show uncertainties in bin size. Points with dashed lines represent the 10th and 90th percentiles across the column. AERONET retrievals from the Zouerate site over the day are shown in dark blue (morning), black (retrieved during the flight) and light blue (retrieved shortly after the flight).

Figure 12: Composite of the dust uplift potential (DUP, shading, $m^3\ s^{-3}$) for the air masses observed by the aircraft LIDARs during all flights from each campaign (blue lines). Calculations have been performed for tropospheric curtains along the flight tracks, integrating the dust uplift potential for the 3 days preceding each research flight. DUPs are shown for (a) Fennec 2011 Falcon flights; (b) Fennec 2011 BAe146 flights; (c) Fennec 2012 BAe146 flights.

Figure 13: (a) and (b) SEVIRI RGB dust imagery for 1000Z and 1700Z, and showing the flight tracks of flight b600 and b601 respectively (BAe146 track in red, F20 track in yellow, black track sections show location of aircraft at satellite image time. (c), (d) and (e) UK Met Office wind forecasts for 06Z at 925hPa (c), 06Z at 10m (d) and 09Z for 925hPa (e), all for 17 June 2011 on the morning of the flight.

Figure 14: Aircraft measurements from the profile descent of b600 (around 1000Z, black) and b601 (around 1700Z, red) corresponding to the tracks, imagery and forecasts shown in Figure 13. Figure shows wind speed (u), wind direction, vertical wind speed (w), corrected extinction coefficient (Ext) calculated from the nephelometer scattering and PSAP absorption, potential temperature, and water vapour mixing ratio (r). Note that altitude is shown in pressure height, corresponding to minimum altitudes of 825m and 784m AGL respectively for b600 and b601.

Figure 15: (a) AOD computed from the Falcon 20 LNG LIDAR extinction coefficient profile at around 1000 UTC on 21 June 2011, flight F22. (b) Cross section ofthe LNG LIDAR extinction coefficient ($10^{-6}m^{-1}$). (c) Shortwave downwelling irradiance (Wm^{-1}, red) and extinction coefficient (10^{-6} m^{-1}, black) as a function of the pressure during the ascent of the BAe146 from within the haboob to upper levels, flight b605. Note that the minimum pressure height of 360 m is equivalent to 105 m above ground level.

Figure 16: a) Measurements made during low level runs in flight b708 on 16 June 2012 sampling uplifted dust by a low level jet. Black line shows radar altitude (height above ground, left axis), accumulation mode extinction measured by the nephelometer and PSAP (green line, left axis), and downwelling shortwave irradiance (red line, right axis) measured by a pyranometer, averaged with a moving window of 20 seconds. Grey shading indicates times when the aircraft was ascending due to poor visibility. b) Profiles of extinction (solid lines) and potential temperature (dashed lines) measured during flight b708, for the descent (black) and ascent (red). Potential temperature has been averaged over 5s windows.

Figure 17: LIDAR and dropsonde observations from 22 June 2011 morning flight b607 (yellow line in Figure 2c) plotted along longitude for a) outgoing and b) return. BAe146 LIDAR measurements (coloured boxes) are shown as the range-corrected LIDAR backscatter signal 355 nm. White regions identify periods of LIDAR data dropouts. Dotted vertical lines indicate dropsonde locations. Black solid lines mark top of the CBL (Convective Boundary Layer) and SRL (Saharan Residual Layer). Grey boxes along dropsonde tracks show depth of temperature inversions (change in °C km-1 shown next to box). Purple line indicates ground level. Dropsonde location ID and release time are indicated above each dropsonde track.

Figure 18: LNG LIDAR-derived extinction coefficient at 532 nm on 20 June 2011 during flight F21 from 25.0N, 11.5W to 19.0N, 8.7W. Water vapour mixing ratio (WVMR, gkg^{-1}) and wind profiles from four dropsondes are superimposed (black lines, dropsonde locations indicated by arrows), with WVMR contours drawn by hand using the LIDAR backscatter; away from the dropsondes these are by necessity subjective and the 7 and 8 gkg^{-1} contours have not been continued west of 21.2N due to a lack of data. Along-track albedo derived from MODIS satellite data is shown in the upper panel, and albedo 1W of the flight track.

Figures for Advances in understanding mineral dust and boundary layer processes, C.L. Ryder et al.

June 15, 2015

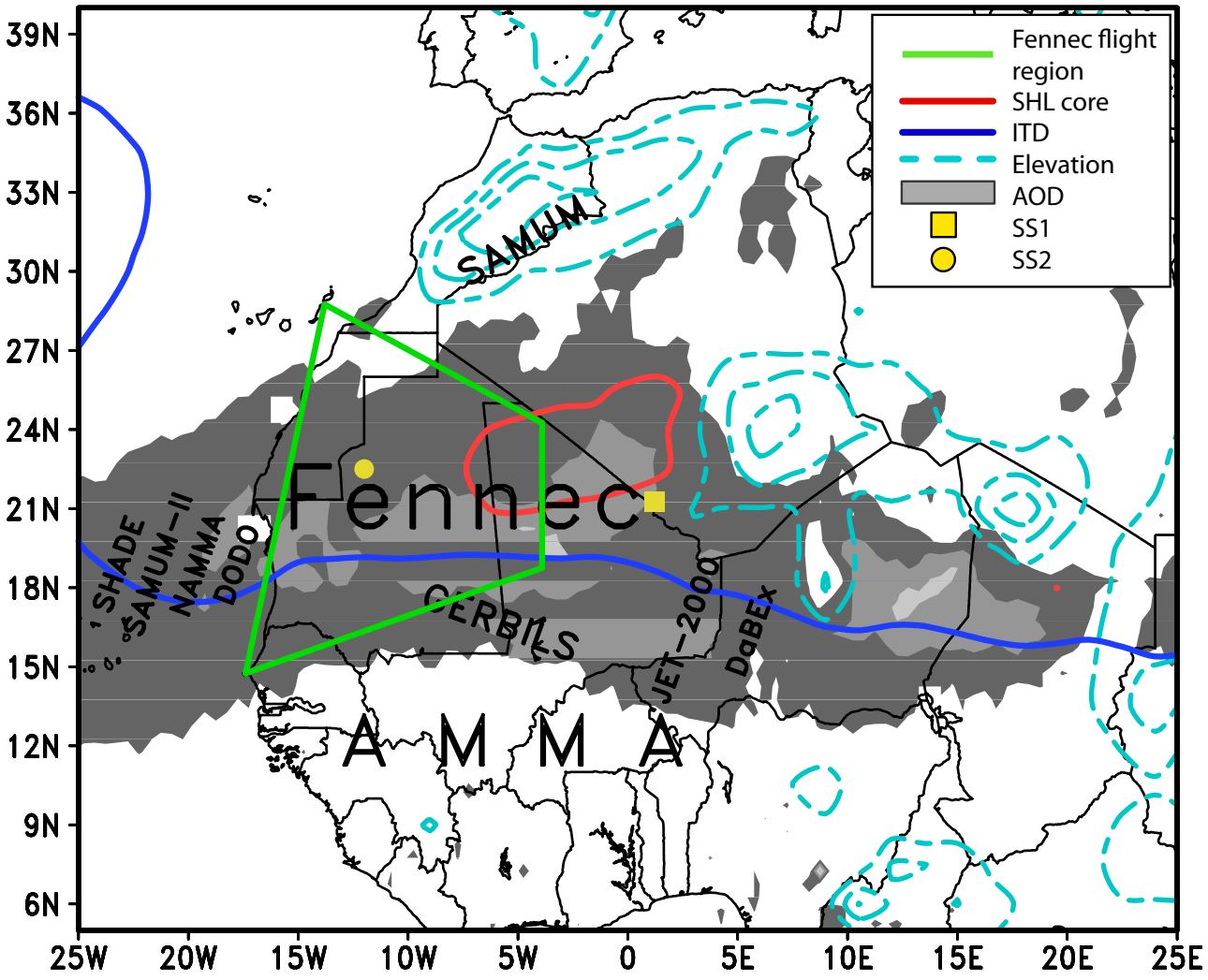

Figure 1: Figure 1

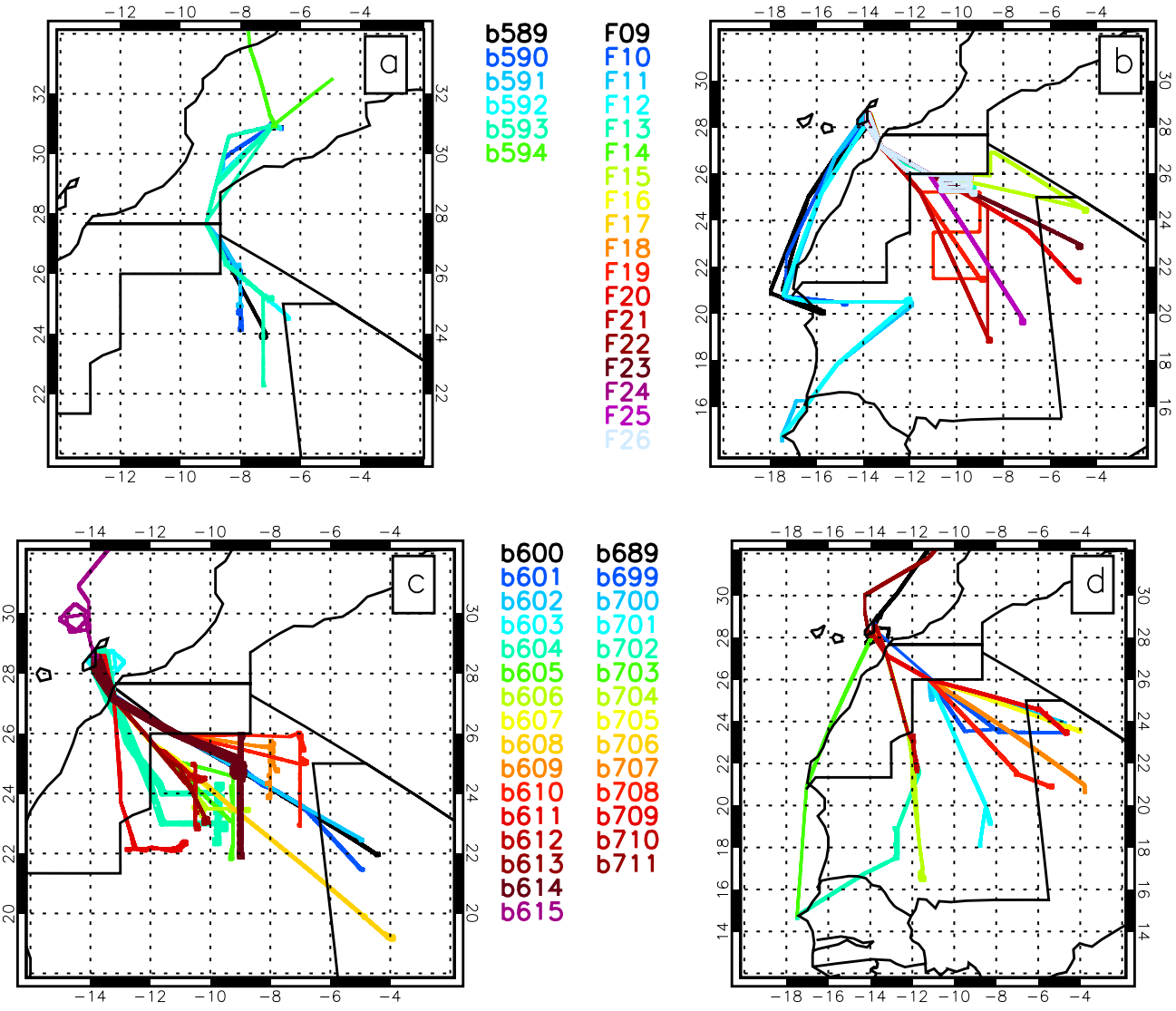

Figure 2: Figure 2

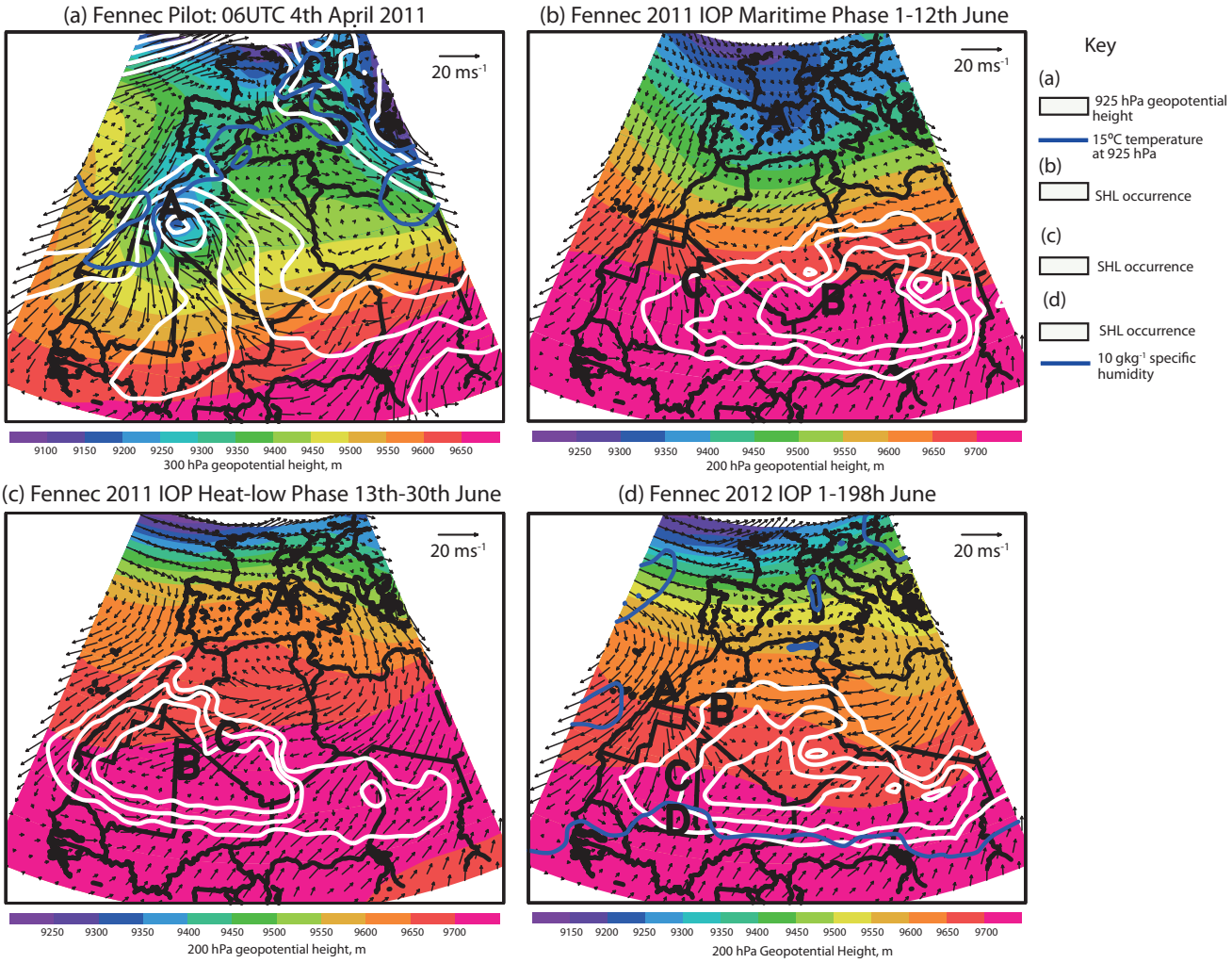

Figure 3: Figure 3

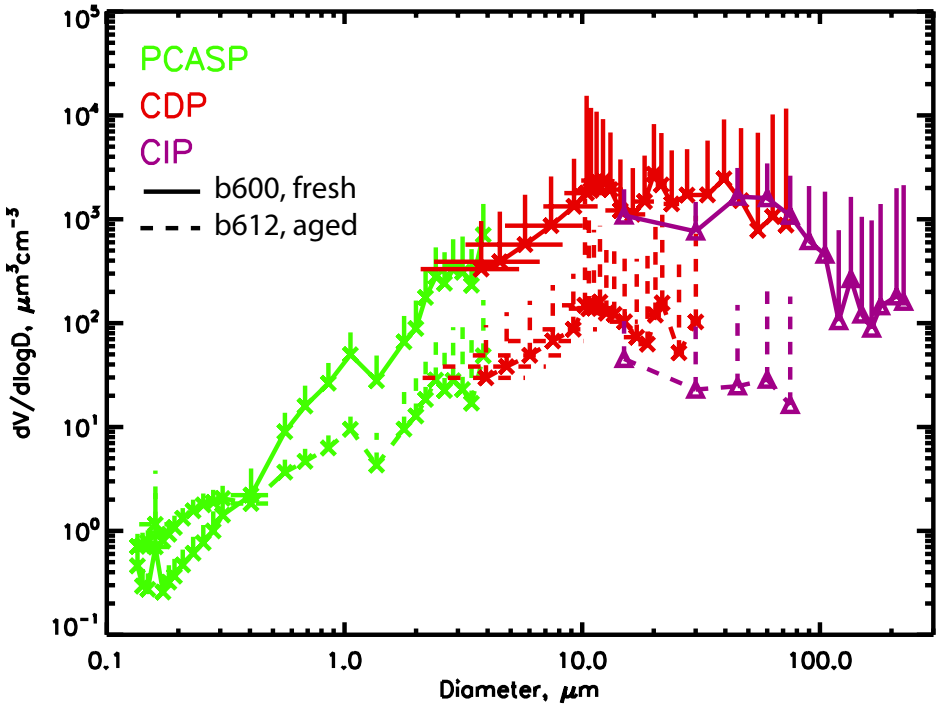

Figure 4: Figure 4

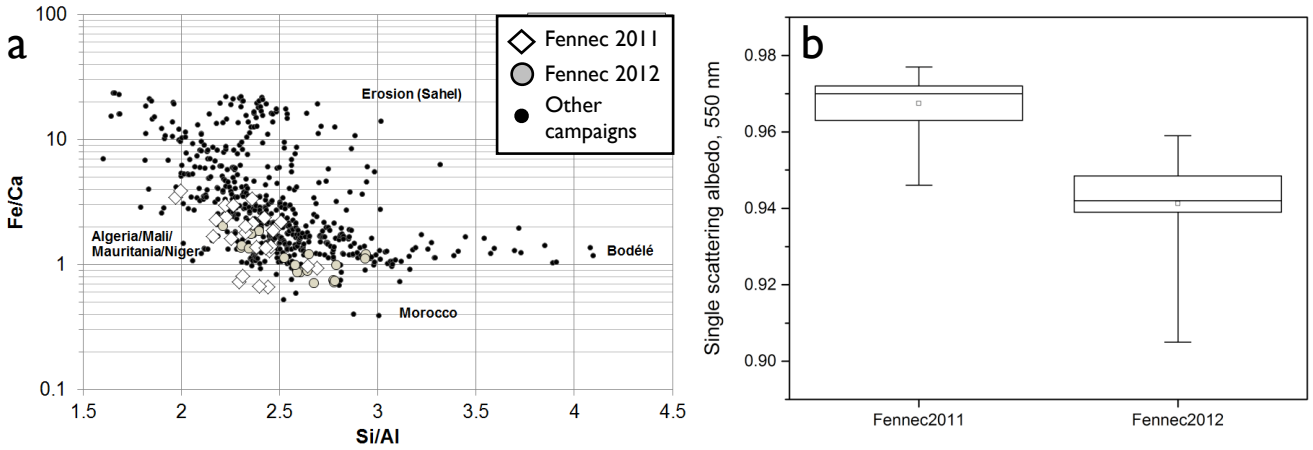

Figure 5: Figure 5

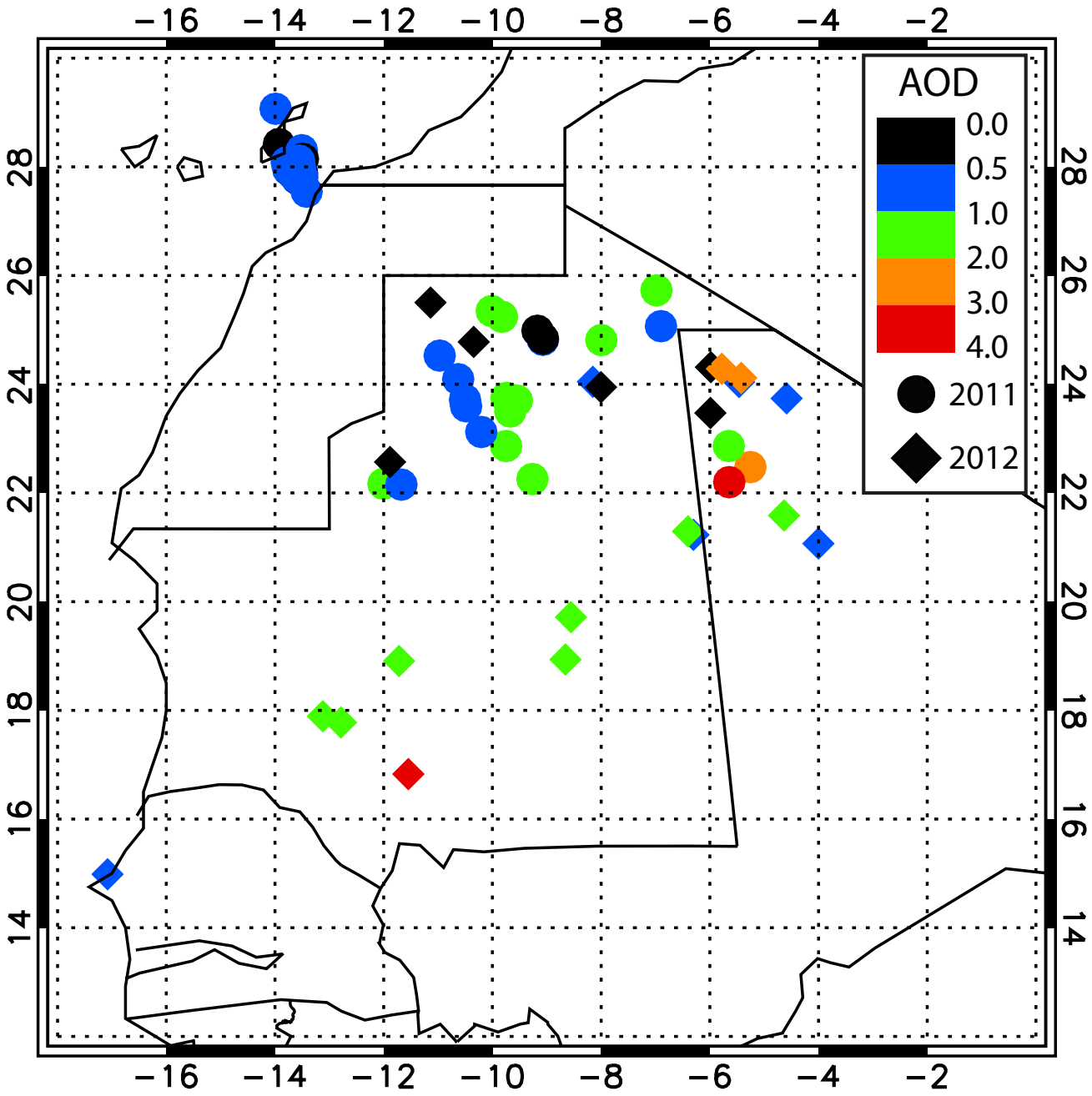

Figure 6: Figure 6

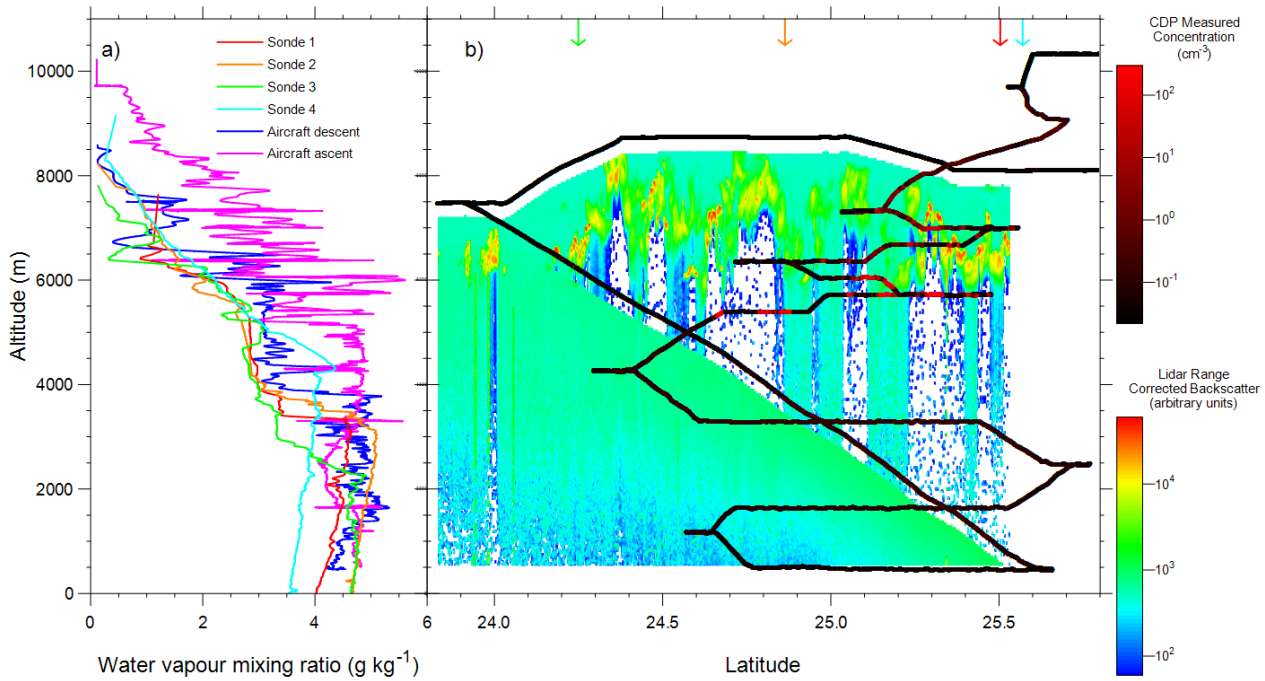

Figure 7: Figure 7

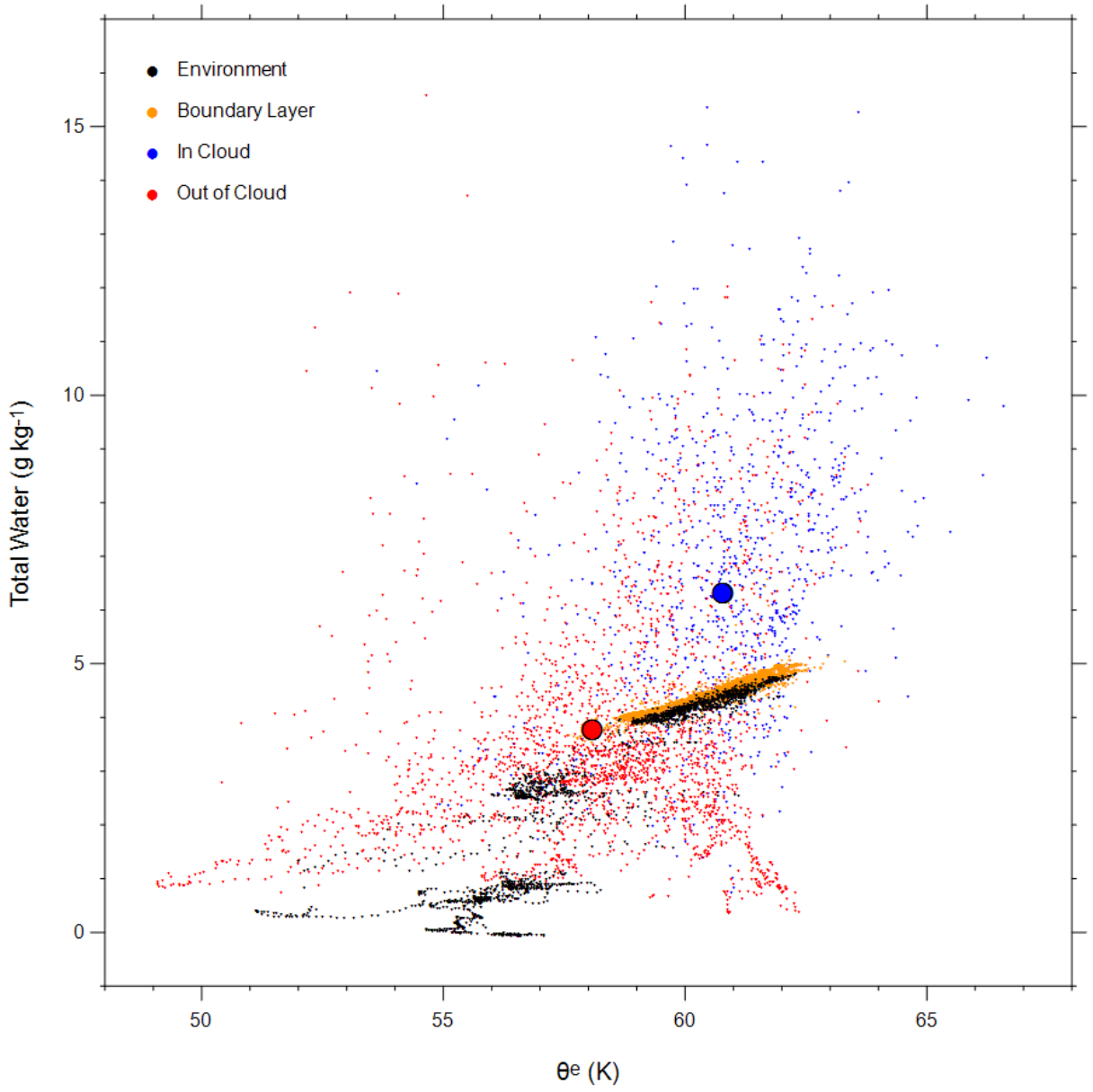

Figure 8: Figure 8

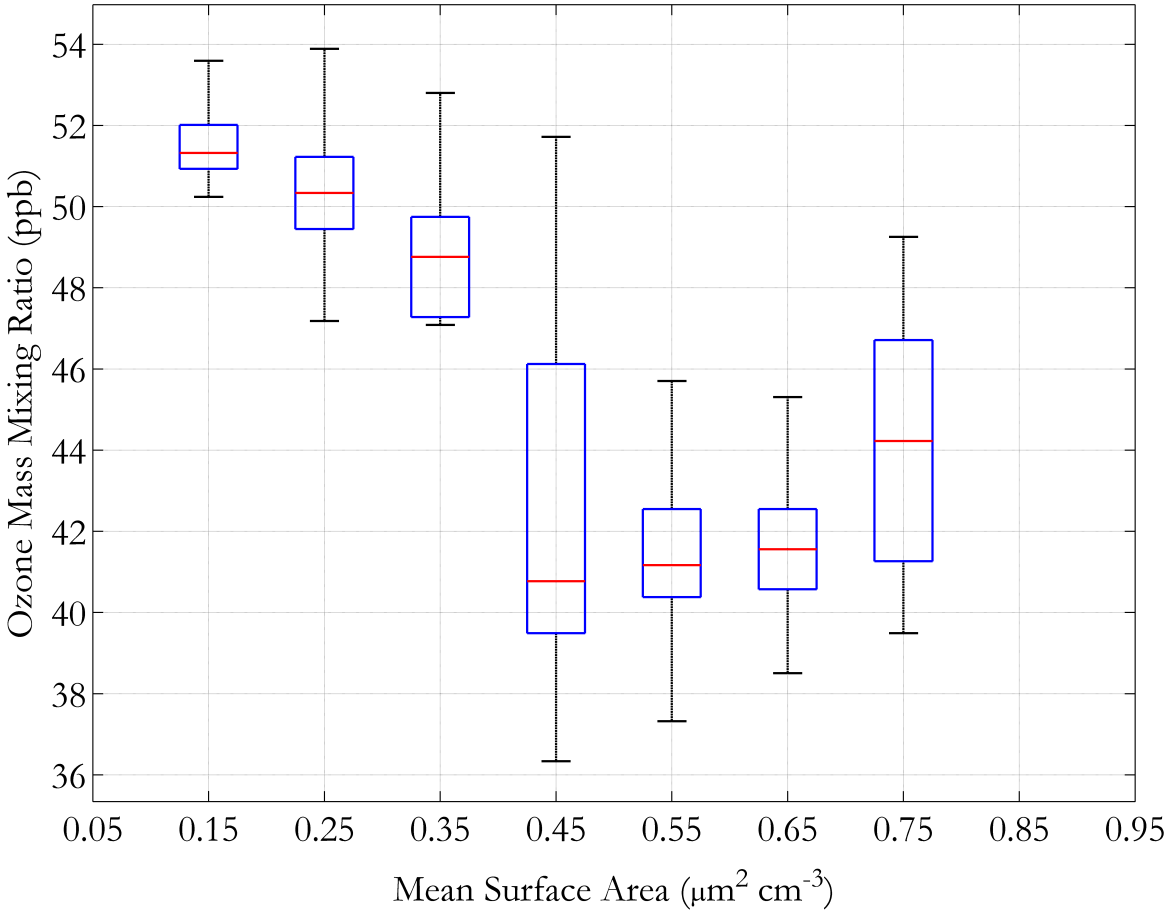

Figure 9: Figure 9

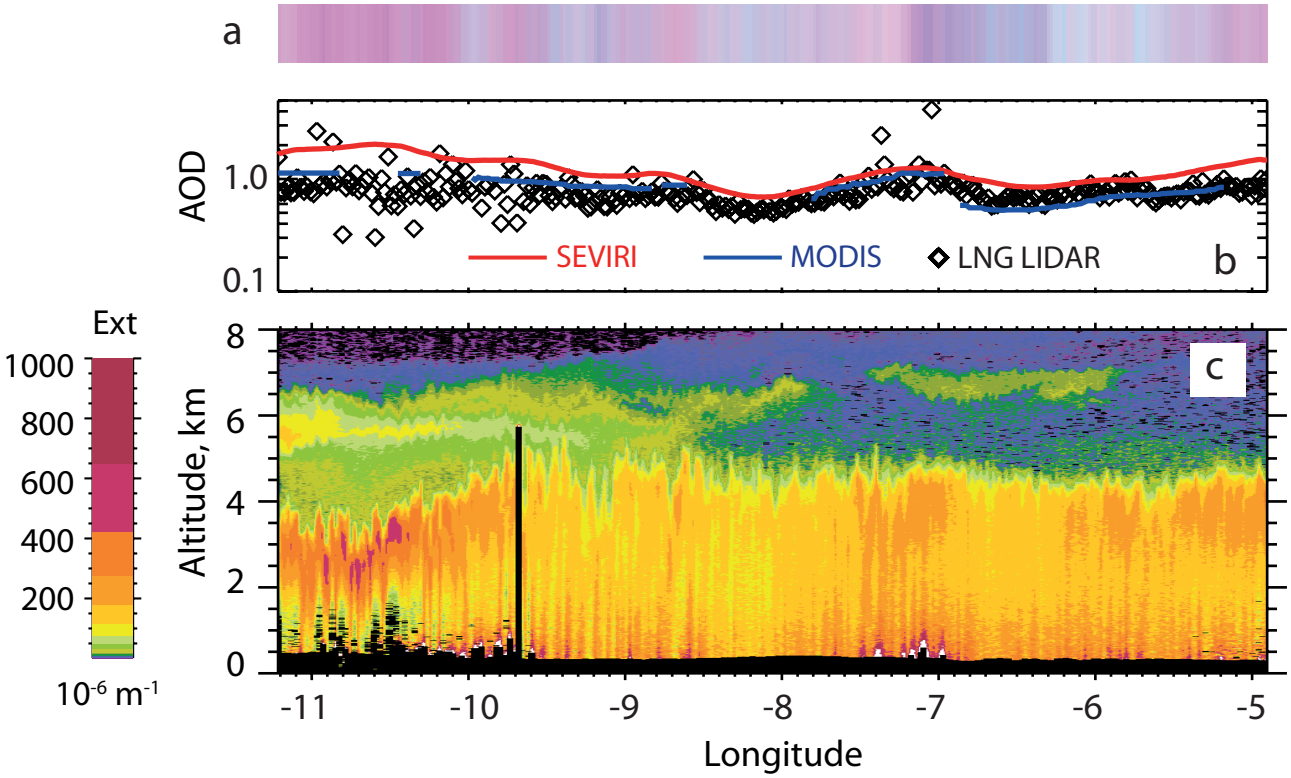

Figure 10: Figure 10

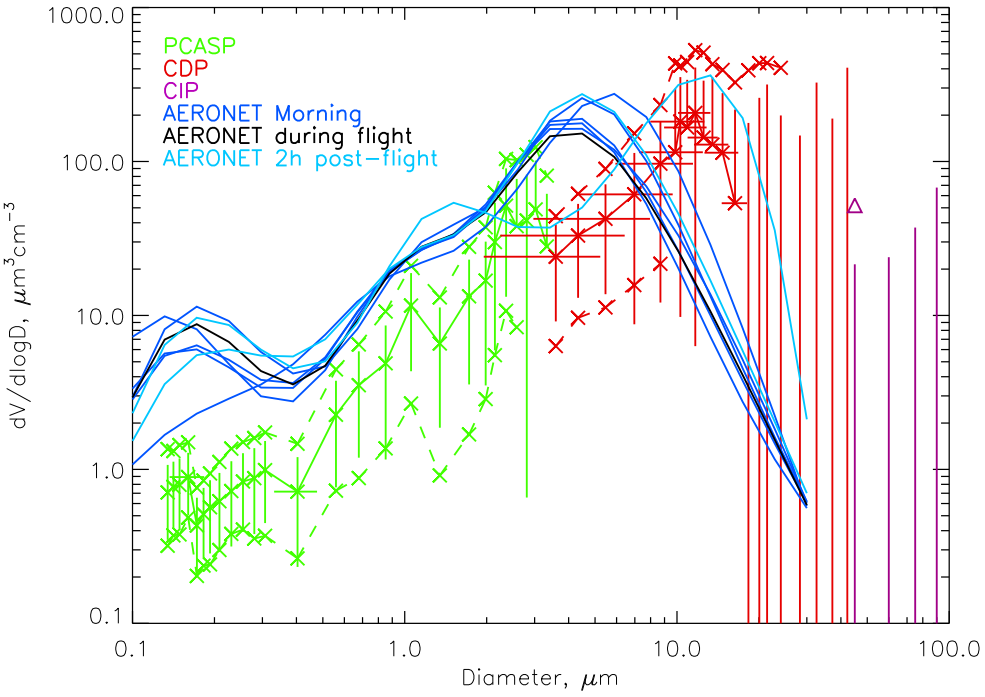

Figure 11: Figure 11

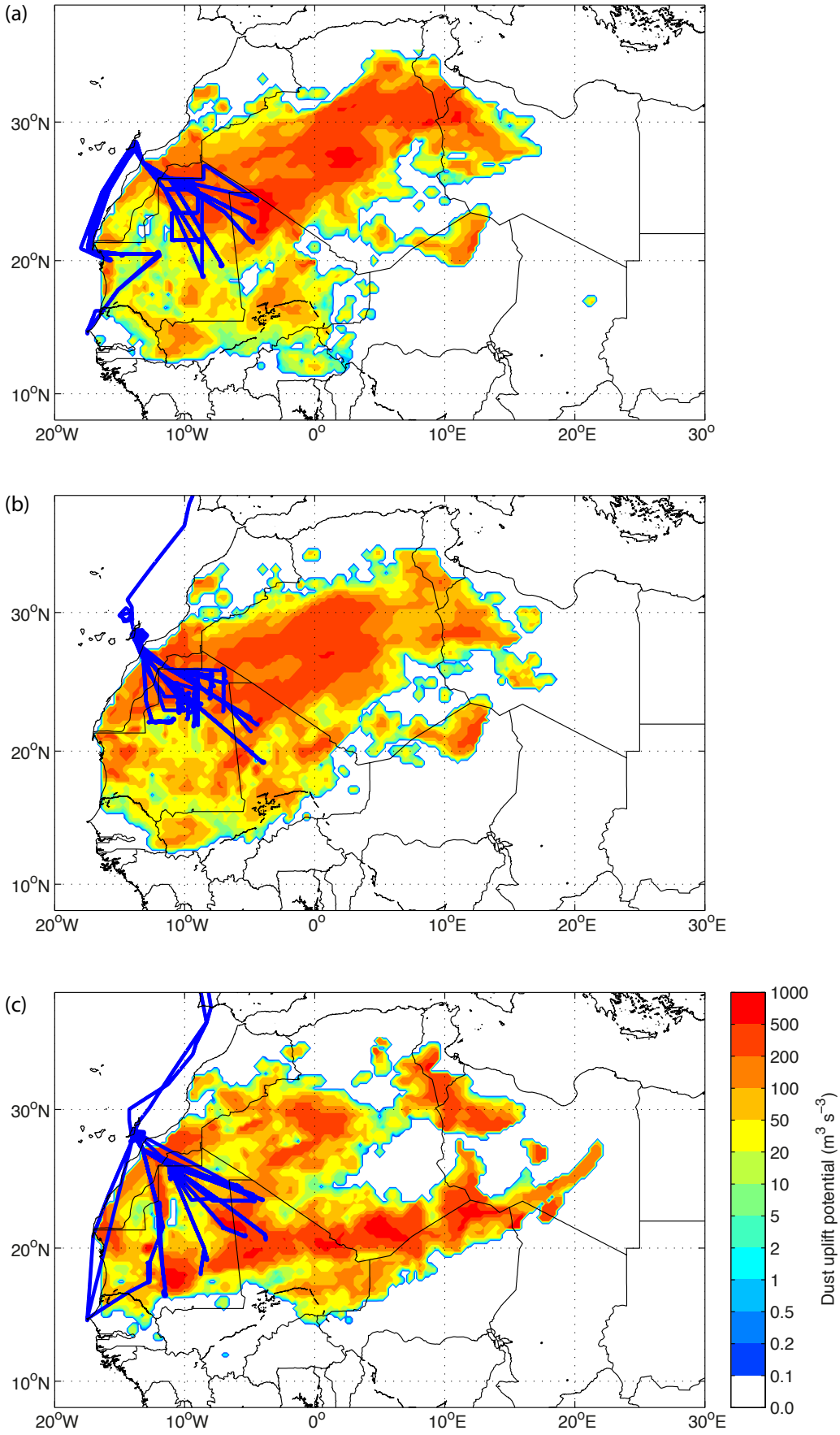

Figure 12: Figure 12

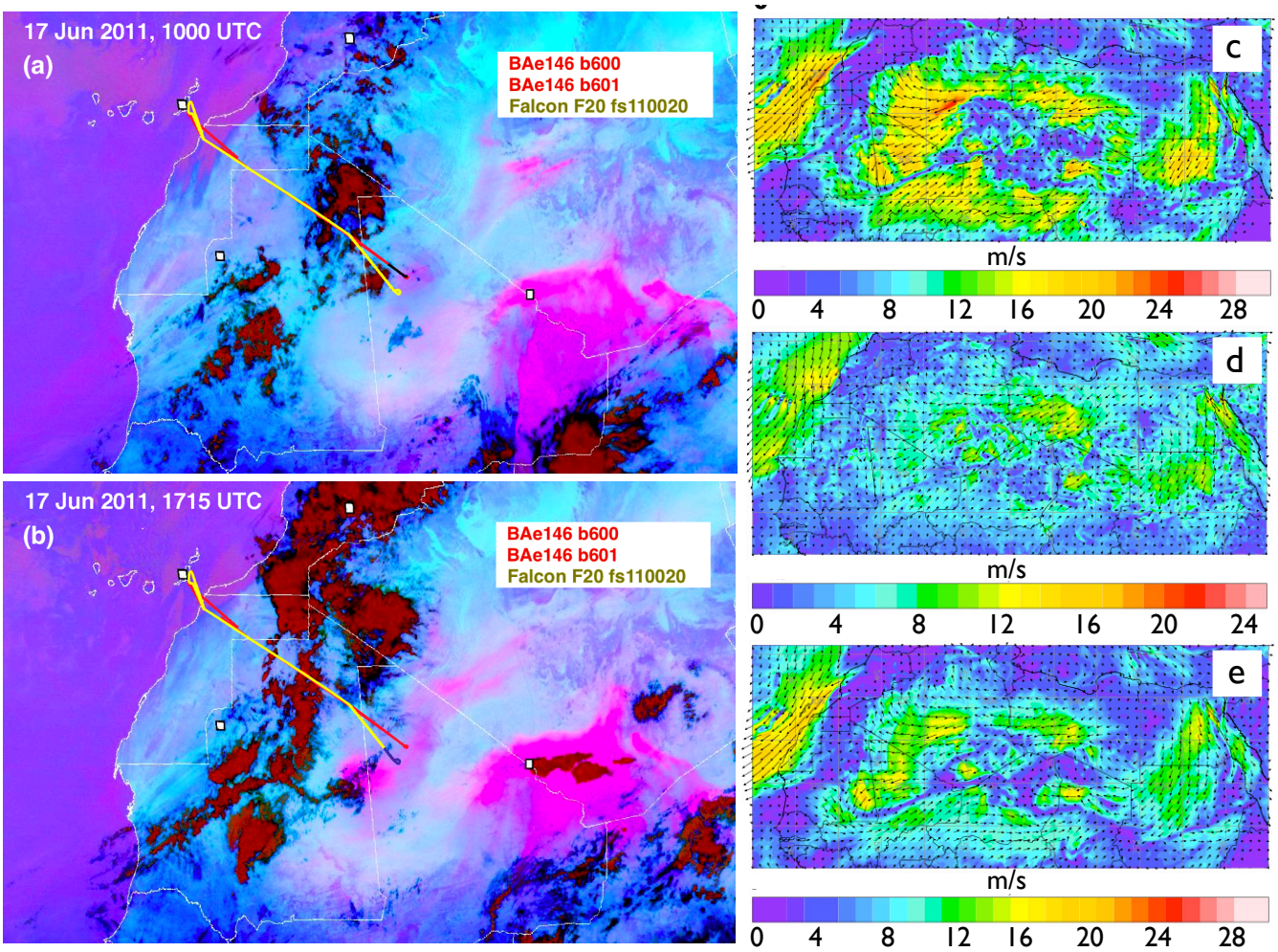

Figure 13: Figure 13

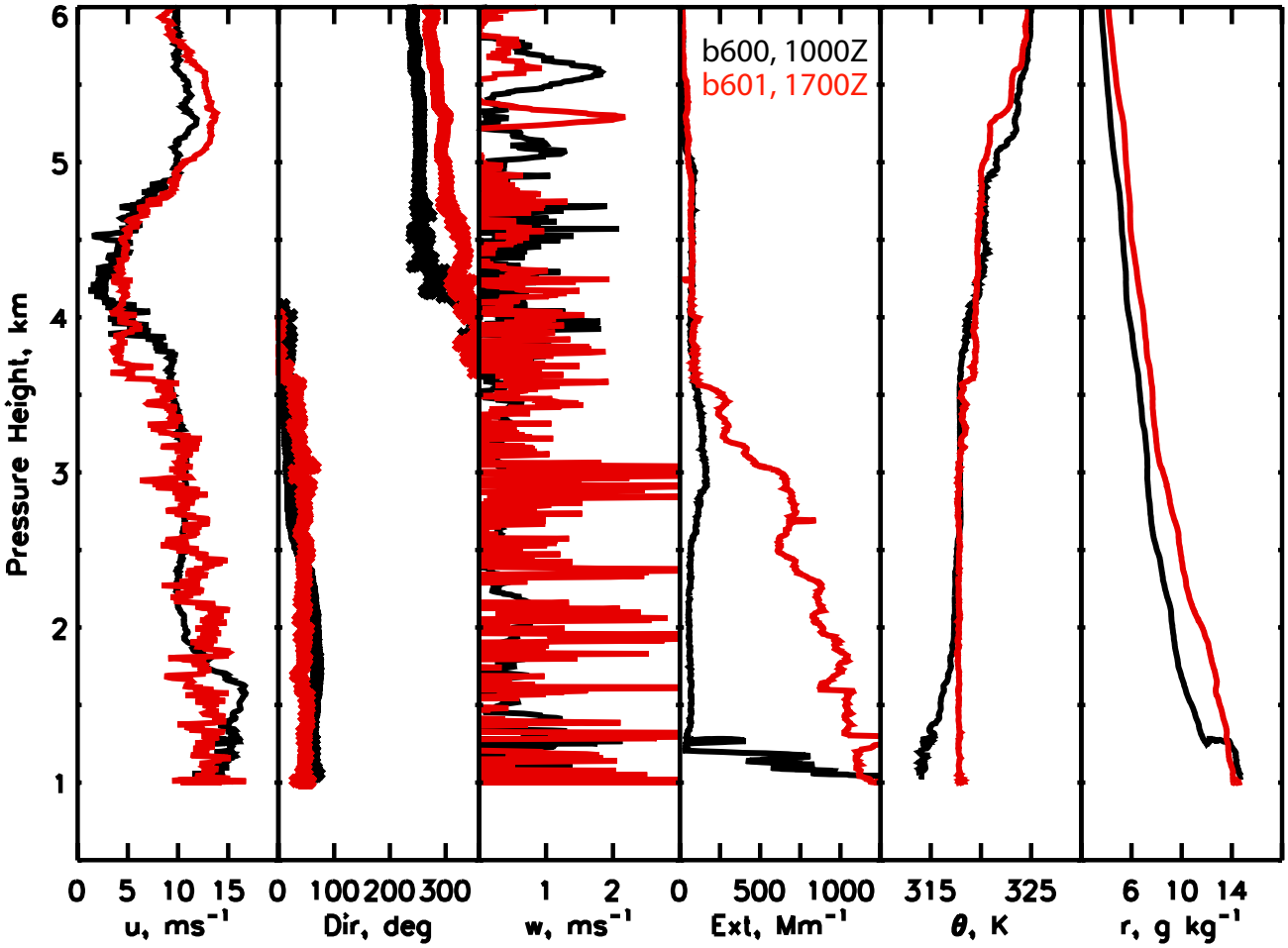

Figure 14: Figure 14

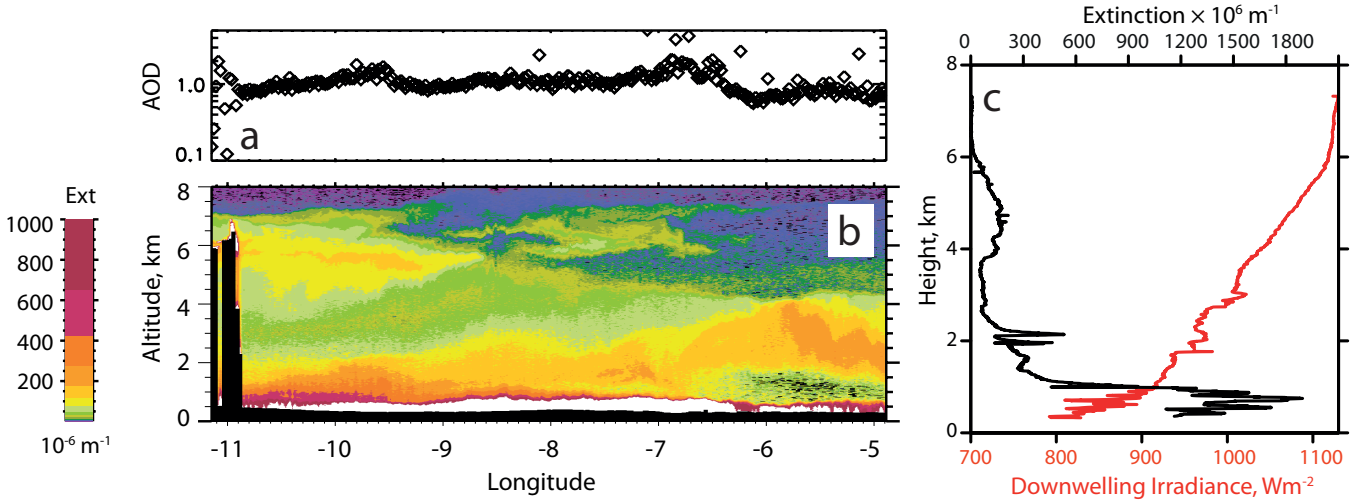

Figure 15: Figure 15

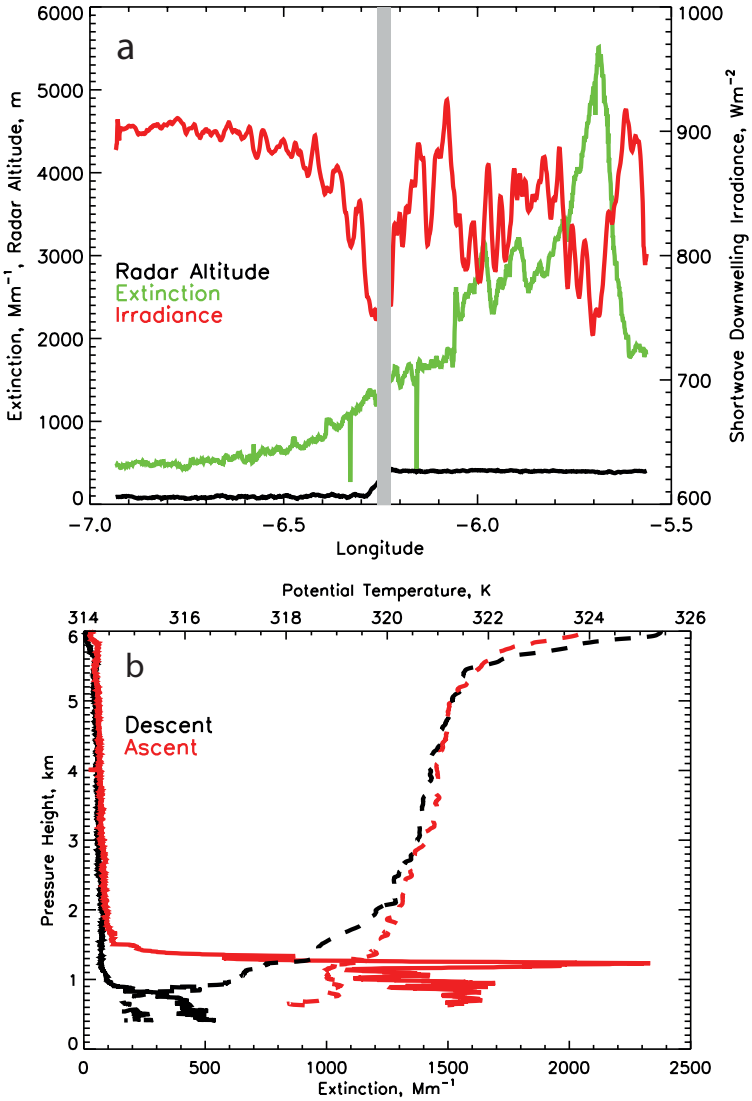

Figure 16: Figure 16

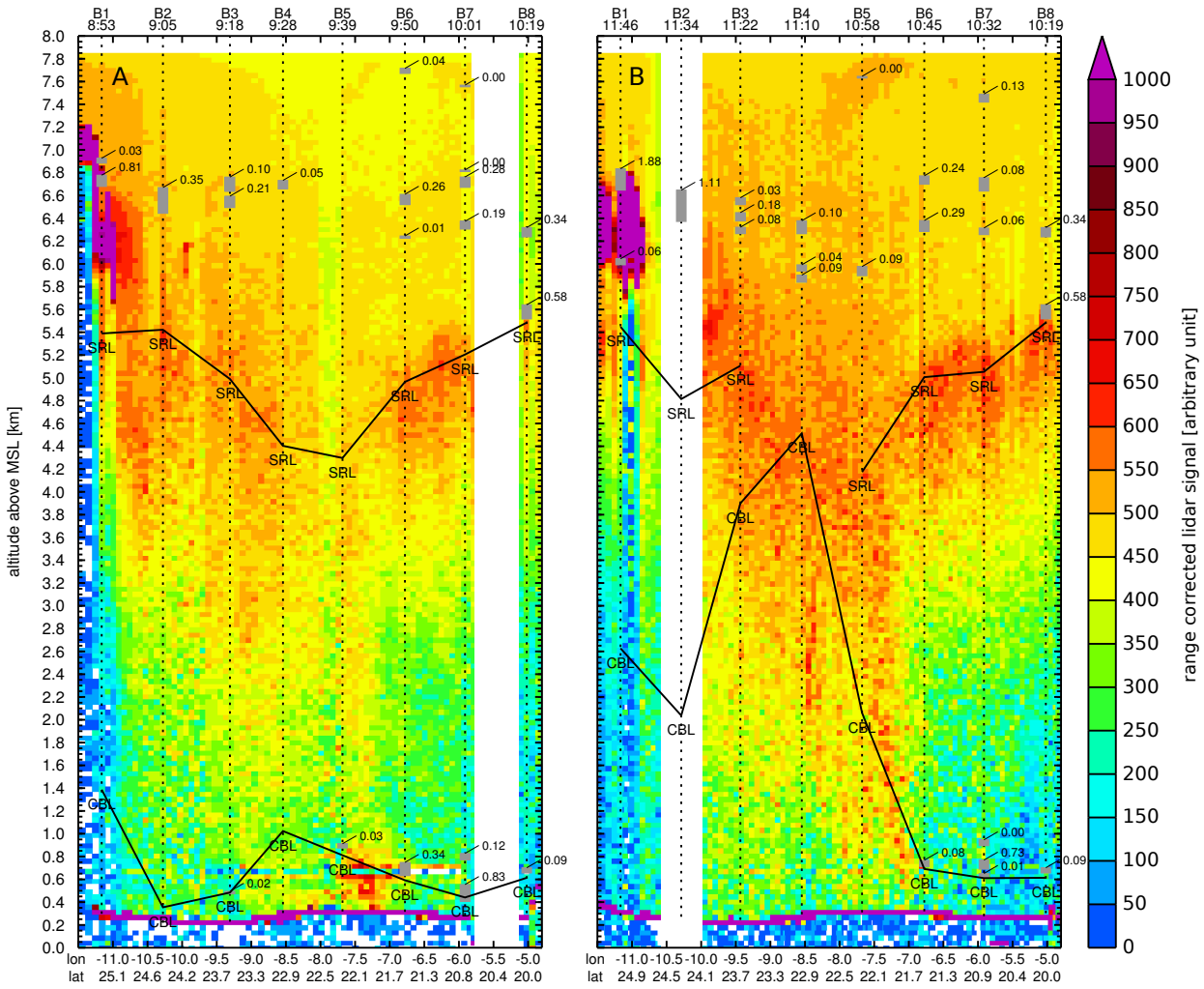

Figure 17: Figure 17

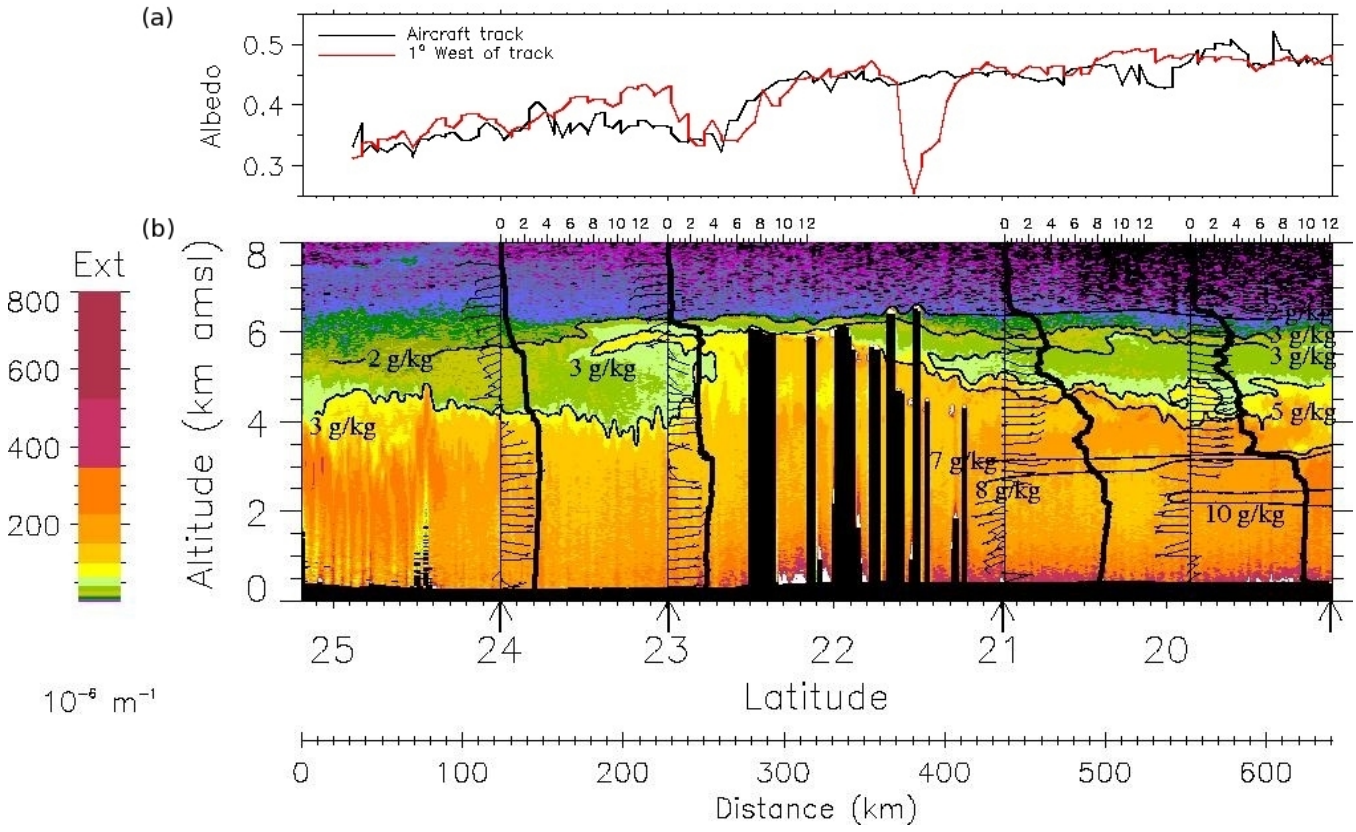

Figure 18: Figure 18